國立臺灣大學理學院化學系

博士論文

Department of Chemistry
College of Science
National Taiwan University
Doctoral Thesis

# 太陽能光敏化染料電池之染料在二氧化鈦表面上的理論計算研究與其相關性質的探討

# Theoretical Study of Dyes Anchoring onto the $TiO_2$ Surface in DSCs and Their Relevant Properties

劉士弘

Shih-Hung Liu

指導教授：周必泰 博士

Advisor: Pi-Tai Chou, Ph.D.

中華民國 102 年 7 月

July, 2013

# 國立臺灣大學博士學位論文
# 口試委員會審定書

**太陽能光敏化染料電池之染料在二氧化鈦表面上的理論計算研究與其相關性質的探討**

**Theoretical Study of Dyes Anchoring onto the $TiO_2$ Surface in DSCs and Their Relevant Properties**

本論文係**劉士弘**君（學號 **D96223131**）在國立臺灣大學化學系完成之博士學位論文，於民國 **102** 年 **7** 月 **30** 日承下列考試委員審查通過及口試及格，特此證明。

口試委員：

_____（簽名）
（指導教授）

_____ 何美舜

陳輝龍 李祐慈

康敦

系主任、所長 _____（簽章）

# 誌謝

能夠完成博士學位，最感謝的人是我的指導教授，周必泰教授。謝謝周老師對我的包容與熱忱指導，讓我在專業領域的研究工作收獲良多。

非常感謝我的口試委員，何美霖教授，康佳正教授，李祐慈教授，陳輝龍教授，在我的學位口試時，提供許多實貴的建議，讓我能夠及時改正我研究成果的缺失。

同時我要感謝實驗室各位伙伴的幫忙與指導，唐國鈞學長，沈俊義學長，莊惟廸學長，陳協志學長，陳東藝，趙偉志，曾維宣，張志雲，林佳貞，黃懷慶，梁聖彬，陳其霖，林子傑，陳怡安，劉啟璋，郭廷逸，林鈺璇，許晏豪，曾昱睿，吳毓心，張珮甄，簡韻宸，陳冠瑜，胡元正，杜庭薰。

另外要特別感謝已經離開實驗室的伙伴，鄭宜明學長，謝承志，賴志維，吳以哲，劉瑋鑫，陳柏壽，賴正軒，陳祺霖，劉建良，符宏信，李宗憓，李志強，吳忠燁，徐佳榕，徐丞志，姜昌明，林竣偉，施純偉，楊孟儒，彭歆傑，王康為，林奕志，余雅倩，陳敬亭，詹子瑩，林昭辰，鍾敏玟，陳昱群，林宗毅，彭詠康，林佳莉，鄭詠之，潘校安，張育佳，潘星儒，蕭怡瑄，陳羿如，蔡佩芬，陳昱安，劉駿。

謝謝這些年來在實驗室遇到的每位伙伴，讓我這段期間的人生經歷更顯得多采多姿，非常感謝大家的幫忙。

# 中文摘要

**關鍵詞：**太陽能光敏化染料電池，染料，二氧化鈦表面，電子傳遞，光電轉換過程，基態，激發態

隨著人類對石油和天然氣的使用殆盡，尋找替代性能源是現今學界首要的研究工作，利用太陽光來發電是研究的領域之一，其中以太陽能光敏化敏料電池（Dye-Sensitized Solar Cells, DSCs）具有低成本、容易操作的優點。目前最高的光致電轉換效率為 12%，如何提升 DSCs 的光致電轉換效率是學界急需突破的瓶頸。

在 DSCs 的元件中，染料吸收太陽的可見光及紅外光，染料的電子從染料的基態躍遷到激發態，接著電子再注入到二氧化鈦表面上，電子在二氧化鈦內傳遞，經由外電路，再得到人類日常生活所需要的電能。

染料在二氧化鈦表面上的介面行為是非常複雜的，如何利用理論計算的方法來得知此介面行為的機制是我們的研究主題。我們利用軟體 Gaussian 09 模擬以重金屬 Ru 和 Os 為中心金屬的三配位基染料，此兩類染料可以吸收紅外光，有 10% 左右的光致電轉換效率，在長時間元件的使用期間裡具有良好的穩定性。我們經由理論計算的吸收光譜跟實驗得到的吸收光譜作比較，發現有良好的可信度，另外我們可以得到各個軌域的電子分布，進而對染料在二氧化鈦表面上的介面行為有更深入的瞭解，進而提升 DSCs 的光致電轉換效率。

在染料的設計方面，我們可以從太陽光的組成來探討，太陽光的組成為紫外線，可見光，紅外光，其中紅外光佔了一半，如何讓染料可以吸收更多的紅外光，是目前學界想要解決的難題之一。我們可以經由理論計算的計算，來預測未知染料的光電性質，進而節省實驗合成的繁瑣程序。

本篇論文分為兩個章節來討論，在第一章裡，我們用 Ru(II)為中心金屬的三配位基染料 N749，N749 分別帶有 0，1，2，3 個羧酸根的質子，模擬它們在二氧化鈦表面上光電轉換現象，共有七種模型，我們的計算結果與實驗相符，因此我們的計算方法是可以被認可的。

接著，在第二章裡，我們計算了以 Os(II)為中心金屬的兩個三配位基染料，分別為 TF-51-Os 和 TF-52-Os，以及以 Ru(II)為中心金屬的兩個三配位基染料，分別為 TF-51-Ru 和 TF-52-Ru，總共四個染料。TF-51-Os 和 TF-51-Ru 具有相同的分子結構，而且 TF-52-Os 和 TF-52-Ru 也具有相同的分子結構。這四個染料在做成 DSCs 元件時，都可以吸收紅外光，而且 Os(II)染料比 Ru(II)染料可以吸收更多的紅外光，而我們的理論計算結果也顯示一樣的趨勢，因此我們可以更深入瞭解以 Os(II)與 Ru(II)為中心金屬的染料不同之處。

在未來的工作裡，我們可以計算更多不同的染料在二氧化鈦的光電性質，進而對染料在二氧化鈦表面上的介面現象有更深層的認識，也是本篇論文的最大目標。

# Abstract

**Keywords**: DSCs, dye, Ru(II)–dye, Os(II)–dye, $TiO_2$, electron injection, optical electron transfer, electronic coupling

**Chapter I: Theoretical Study of N749 Dyes Anchoring on the $(TiO_2)_{28}$ Surface in DSCs and Their Electronic Absorption Properties**

In chapter I, we have performed calculations on the panchromatic N749 dyes adsorbed on the $(TiO_2)_{28}$ surface. N749 is a prototypical form of Ru(II) complexes for dye sensitized solar cells (DSCs), which possesses a terpyridine tridentate ligand bearing four different protonation states (0, 1, 2, or 3 carboxylic protons). Depending on the type of proton bonding interaction (protonated and deprotonated), seven N749/$(TiO_2)_{28}$ surface models (N749-0H/$(TiO_2)_{28}$, N749-1H-P/$(TiO_2)_{28}$, N749-1H-DP/$(TiO_2)_{28}$, N749-2H-P/$(TiO_2)_{28}$, N749-2H-DP/$(TiO_2)_{28}$, N749-3H-P/$(TiO_2)_{28}$, and N749-3H-DP/$(TiO_2)_{28}$) have been applied in this study for the geometry optimization, frontier molecular orbital level diagrams, and calculated absorption spectra. The moderate surface area of $(TiO_2)_{28}$ cluster is suitable for N749 dyes adsorbing behaviors so that all calculations can be performed using the Gaussian 09 program package. We have carefully examined these seven N749/$(TiO_2)_{28}$ assemblies that could influence the DSCs device performance. The calculated absorption spectra of these seven various N749/$(TiO_2)_{28}$ models are in good agreement with the experimental results by Hagfeldt

et al. [*J. Phys. Chem. B*, **2002**, *106*, 12693–12704] with onset ranging from visible to near-IR region. The combination of the adsorption energy onto $TiO_2$ and calculated absorption spectra (c.f. the experimental results) concludes that the deprotonated dyes constitute the most favorable and dominant structure in the DSCs devices. The frontier molecular orbital graphs indicate that the electron charge distribution of all HOMOs are located at the N749 dyes while LUMOs are localized at the $(TiO_2)_{28}$ surface or delocalized at the interfacial regions of N749/$(TiO_2)_{28}$. The corresponding transitions are thus more like a type of optical electron transfer, injecting the electron to the interfacial $TiO_2$.

**Chapter II: Tridentate Terpyridine Os(II)– and Ru(II)–Based Dyes**

**Anchoring on the $(TiO_2)_{38}$ Surface in DSCs – A Theoretical Study**

In Chapter II, in the past decade, Os(II)–based panchromatic dye sensitized solar cells (DSCs) are an alternatively accessible choice to replacing the traditional heavy metal Ru(II)–based dyes. In 2012, we reported two synthesized Os(II)–based dyes with photo-current conversion efficiency reaching 8.85% in our experimental research. In this theoretical study, we performed the simulation regarding two Os(II)– (TF-51-Os and TF-52-Os) and two Ru(II)–based (TF-51-Ru and TF-52-Ru) dyes anchoring onto the anatase (101) $(TiO_2)_{38}$ surface. In total, we simulated four dye/$(TiO_2)_{38}$ surface models. Based on the same structures (TF-51-Os *vs*. TF-51-Ru and TF-52-Os *vs*.

TF-52-Ru), we could make a comparative study relating the Os(II)– and Ru(II)–based dyes in DSCs. By the way, we also quantitatively estimated the electronic coupling between the dye and $(TiO_2)_{38}$ interfacial interaction using the Generalized Mulliken–Hush (GMH) theory with configuration–interaction singles (CIS) method. This article is the first report theoretically studying about the Os(II)–based dye in DSCs, and we believe that it could open a new doorway in the heavy metal based dye/$TiO_2$ research field.

# Contents

## Chapter I: Theoretical Study of N749 Dyes Anchoring on the $(TiO_2)_{28}$ Surface in DSCs and Their Electronic Absorption Properties


1.1 Abstract……..……..2

1.2 Introduction…….……4

1.3 Models and Computational Methods……..8

1.4 Results and Discussion…….…….11

1.4.1 $(TiO_2)_{28}$ Surface and Associated Behaviors of the N749/$(TiO_2)_{28}$ Models…....11

1.4.2 Frontier Molecular Orbitals and Absorption Spectra……...…….12

1.4.2.1 N749-0H/$(TiO_2)_{28}$, N749-1H-DP/$(TiO_2)_{28,}$ N749-2H-DP/$(TiO_2)_{28}$, *vs*. N749-3H-DP/$(TiO_2)_{28}$.....16

1.4.2.2 N749-1H-P/$(TiO_2)_{28,}$ N749-2H-P/$(TiO_2)_{28}$, *vs*. N749-3H-P/$(TiO_2)_{28}$.....17

1.4.2.3 N749-nH-P/$(TiO_2)_{28}$ *vs*. N749-nH-DP/$(TiO_2)_{28}$ (n = 1, 2, 3).....17

1.4.3 Theoretical *vs*. Experimental Approach…….....18

1.5 Conclusion…….22

1.6 References.....60

## Chapter II: Tridentate Terpyridine Os(II)– and Ru(II)–Based Dyes Anchoring on the $(TiO_2)_{38}$ Surface in DSCs – A Theoretical Study

2.1 Abstract.....66

2.2 Introduction.....67

2.3 Models and Computational Methods.....72

2.4 Results and Discussion.....74

2.4.1 $(TiO_2)_{38}$ Surface and Associated behaviors of the four dye/$(TiO_2)_{38}$ Models.....74

2.4.2 Frontier Molecular Orbitals and Absorption Spectra.....75

2.4.3 Electronic Coupling Estimation.....79

2.5 Conclusion.....84

2.6 References.....122

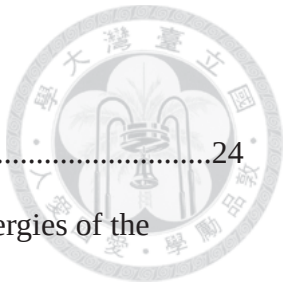

## Figure Captions

**Figure 1.1** Molecular structures of various N749 dyes.....24

**Figure 1.2** Optimized geometries, O–Ti distances, and adsorption energies of the $(TiO_2)_{28}$ cluster and seven N749/$(TiO_2)_{28}$ models.....25

**Figure 1.3** Molecular orbital energy level (eV) diagram from HOMO-10 to LUMO+30 of the seven N749/$(TiO_2)_{28}$ surface models.....26

**Figure 1.4** Frontier molecular orbitals of N749-0H/$(TiO_2)_{28}$.....27

**Figure 1.5** Frontier molecular orbitals of N749-1H-P/$(TiO_2)_{28}$.....30

**Figure 1.6** Frontier molecular orbitals of N749-1H-DP/$(TiO_2)_{28}$.....33

**Figure 1.7** Frontier molecular orbitals of N749-2H-P/$(TiO_2)_{28}$.....36

**Figure 1.8** Frontier molecular orbitals of N749-2H-DP/$(TiO_2)_{28}$.....39

**Figure 1.9** Frontier molecular orbitals of N749-3H-P/$(TiO_2)_{28}$.....42

**Figure 1.10** Frontier molecular orbitals of N749-3H-DP/$(TiO_2)_{28}$.....45

**Figure 1.11** The experimental N749-1H/$TiO_2$ and calculated absorption spectra of the four N749-DP/$(TiO_2)_{28}$ surface models.....48

**Figure 1.12** The experimental N749-1H/$TiO_2$ and calculated absorption spectra of the three N749-P/$(TiO_2)_{28}$ surface models.....49

**Figure 1.13** HOMO and LUMO+6 in N749-1H-DP/$(TiO_2)_{28}$ during optical absorption photoexcitation.....50

**Figure 1.14** HOMO and LUMO+3 in N749-0H/$(TiO_2)_{28}$ during optical absorption photoexcitation.....51

**Figure 1.15** HOMO and LUMO+1 in N749-1H-P/$(TiO_2)_{28}$ during optical absorption photoexcitation.....52

**Figure 1.16** HOMO and LUMO+3 in N749-2H-P/$(TiO_2)_{28}$ during optical absorption photoexcitation.....53

**Figure 1.17** HOMO and LUMO+7 in N749-2H-DP/$(TiO_2)_{28}$ during optical absorption photoexcitation.....54

**Figure 1.18** HOMO and LUMO+5 in N749-3H-P/$(TiO_2)_{28}$ during optical absorption photoexcitation.....55

**Figure 1.19** HOMO and LUMO+13 in N749-3H-DP/$(TiO_2)_{28}$ during optical absorption photoexcitation.....56

**Figure 1.20** The experimental N749-1H/$TiO_2$ and calculated absorption spectra of N749-1H-P/$(TiO_2)_{28}$ and N749-1H-DP/$(TiO_2)_{28}$ surface models.....57

**Figure 1.21** The experimental N749-1H/$TiO_2$ and calculated absorption spectra of N749-2H-P/$(TiO_2)_{28}$ and N749-2H-DP/$(TiO_2)_{28}$ surface models.....58

**Figure 1.22** The experimental N749-1H/$TiO_2$ and calculated absorption spectra of N749-3H-P/$(TiO_2)_{28}$ and N749-3H-DP/$(TiO_2)_{28}$ surface models.....59

**Figure 2.1** Molecular structures of compound TF51-Os, TF51-Ru, TF52-Os, and TF52-Ru.....86

**Figure 2.2** Optimized geometries, O–Ti distances, and adsorption energies of the four dye/$(TiO_2)_{38}$ and $(TiO_2)_{38}$ model.....87

**Figure 2.3** Molecular orbital energy level diagram of the four dye/$(TiO_2)_{38}$ models.....88

**Figure 2.4** HOMO and LUMO of the four dye/$(TiO_2)_{38}$ models.....89

**Figure 2.5** Frontier molecular orbitals of TF-51-Os/$(TiO_2)_{38}$.....91

**Figure 2.6** Frontier molecular orbitals of TF-51-Ru/$(TiO_2)_{38}$.....95

**Figure 2.7** Frontier molecular orbitals of TF-52-Os/$(TiO_2)_{38}$.....99

**Figure 2.8** Frontier molecular orbitals of TF-52-Ru/$(TiO_2)_{38}$.....103

**Figure 2.9** The experimental spectra and calculated oscillator strengths of the four dye/$(TiO_2)_{38}$ models in DMF.....107

**Figure 2.10** HOMO and LUMO of the four dye/$(TiO_2)_{38}$ in isovalue = 0.002.....108

**Figure 2.11** The lowest singlet optical transition of the four dye/$(TiO_2)_{38}$ models.....109

**Figure 2.12** The HOMO-1 of TF-52-Os/$(TiO_2)_{38}$.....116

**Figure 2.13** The HOMO-1 of TF-52-Ru/$(TiO_2)_{38}$.....117

**Figure 2.14** Schematic illustration of the ground state $S_0$, Frank–Condon excited state S*, and the nuclear geometry optimized medium state $S_1$ during the photoexcitation in TF-52-Os/$(TiO_2)_{38}$.....118

# Table Captions

**Table 1.1** The singlet optical transitions for N749-0H/$(TiO_2)_{28}$.....29

**Table 1.2** The singlet optical transitions for N749-1H-P/$(TiO_2)_{28}$.....32

**Table 1.3** The singlet optical transitions for N749-1H-DP/$(TiO_2)_{28}$.....35

**Table 1.4** The singlet optical transitions for N749-2H-P/$(TiO_2)_{28}$.....38

**Table 1.5** The singlet optical transitions for N749-2H-DP/$(TiO_2)_{28}$.....41

**Table 1.6** The singlet optical transitions for N749-3H-P/$(TiO_2)_{28}$.....44

**Table 1.7** The singlet optical transitions for N749-3H-DP/$(TiO_2)_{28}$.....47

**Table 2.1** The singlet optical transitions for TF-51-Os/$(TiO_2)_{38}$.....90

**Table 2.2** The singlet optical transitions for TF-51-Ru/$(TiO_2)_{38}$.....94

**Table 2.3** The singlet optical transitions for TF-52-Os/$(TiO_2)_{38}$.....98

**Table 2.4** The singlet optical transitions for TF-52-Ru/$(TiO_2)_{38}$.....102

**Table 2.5** Electron contributions in molecular fragments and molecular orbitals of the four dye/$(TiO_2)_{38}$ models.....111

**Table 2.6** Electron contributions in molecular fragments and molecular orbitals of TF-51-Os/$(TiO_2)_{38}$.....112

**Table 2.7** Electron contributions in molecular fragments and molecular orbitals of TF-51-Ru/$(TiO_2)_{38}$.....113

**Table 2.8** Electron contributions in molecular fragments and molecular orbitals of TF-52-Os/$(TiO_2)_{38}$.....114

**Table 2.9** Electron contributions in molecular fragments and molecular orbitals of TF-52-Ru/$(TiO_2)_{38}$.....115

**Table 2.10** The electronic coupling of the four dye/$(TiO_2)_{38}$ models.....119

**Table 2.11** The calculated dipole moments of the four dye/$(TiO_2)_{38}$ models.....120

**Table 2.12** The calculated transition dipole moments of the four dye/$(TiO_2)_{38}$ .....121

# Chapter I: Theoretical Study of N749 Dyes Anchoring on the $(TiO_2)_{28}$ Surface in DSCs and Their Electronic Absorption Properties

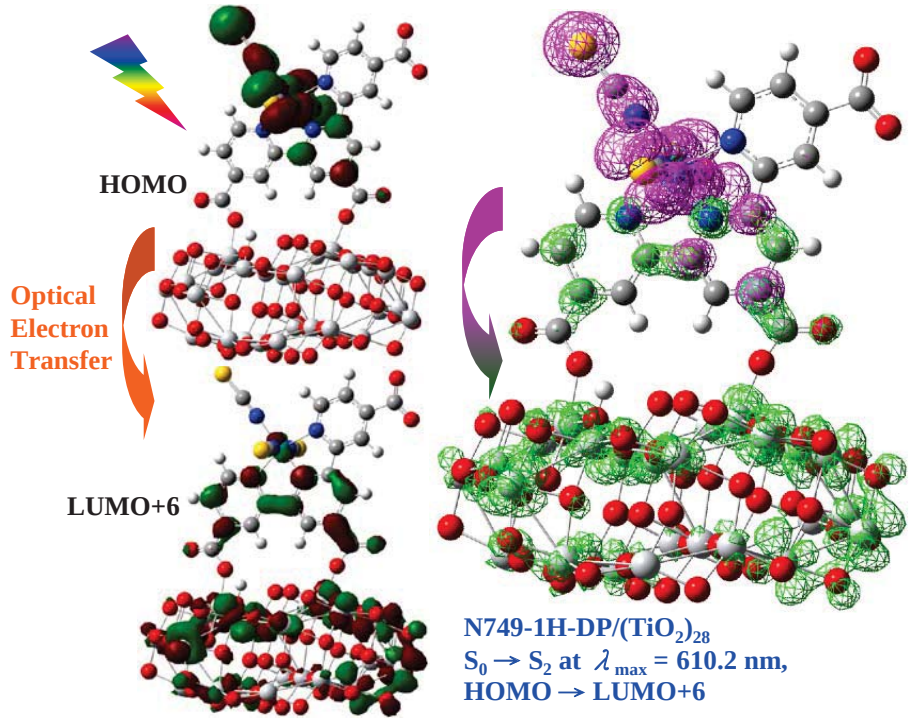


When N749 dye is anchoring onto $TiO_2$ surface in DSCs, the electron of the dye is injected into the $TiO_2$ cluster via ultrafast interfacial charge trasnsfer. Left**:** Frontier molecular orbitals of HOMO and LUMO+6 in N749-1H-DP/$(TiO_2)_{28}$ during optical absorption photoexcitation. Right: Charge density difference between the ground state $S_0$ and the excited state $S_2$. Pink mesh indicates decrease of charge density, while green mesh indicates the increase of charge density upon photoexcitation.

## 1.1 Abstract

We have performed calculations on the panchromatic N749 dyes adsorbed on the $(TiO_2)_{28}$ surface. N749 is a prototypical form of Ru(II) complexes for dye sensitized solar cells (DSCs), which possesses a terpyridine tridentate ligand bearing four different protonation states (0, 1, 2, or 3 carboxylic protons). Depending on the type of proton bonding interaction (protonated and deprotonated), seven N749/$(TiO_2)_{28}$ surface models (N749-0H/$(TiO_2)_{28}$, N749-1H-P/$(TiO_2)_{28}$, N749-1H-DP/$(TiO_2)_{28}$, N749-2H-P/$(TiO_2)_{28}$, N749-2H-DP/$(TiO_2)_{28}$, N749-3H-P/$(TiO_2)_{28}$, and N749-3H-DP/$(TiO_2)_{28}$) have been applied in this study for the geometry optimization, frontier molecular orbital level diagrams, and calculated absorption spectra. The moderate surface area of $(TiO_2)_{28}$ cluster is suitable for N749 dyes adsorbing behaviors so that all calculations can be performed using the Gaussian 09 program package. We have carefully examined these seven N749/$(TiO_2)_{28}$ assemblies that could influence the DSCs device performance. The calculated absorption spectra of these seven various N749/$(TiO_2)_{28}$ models are in good agreement with the experimental results by Hagfeldt et al. [*J. Phys. Chem. B*, **2002**, *106*, 12693–12704] with onset ranging from visible to near-IR region. The combination of the adsorption energy onto $TiO_2$ and calculated absorption spectra (c.f. the experimental results) concludes that the deprotonated dyes constitute the most favorable and dominant structure in the DSCs devices. The frontier molecular orbital graphs

indicate that the electron charge distribution of all HOMOs are located at the N749 dyes while LUMOs are localized at the $(TiO_2)_{28}$ surface or delocalized at the interfacial regions of N749/$(TiO_2)_{28}$. The corresponding transitions are thus more like a type of optical electron transfer, injecting the electron to the interfacial $TiO_2$.

## 1.2 Introduction

Dye-sensitized solar cells (DSCs) have been considered as a practical and accessible alternative to the conventional amorphous silicon solar cells due to their cost-effective and highly efficient conversion of photovoltaic energy.[1-4] The DSCs devices are composed of a nanocrystalline $TiO_2$ anatase (101) film adsorbed by organic or inorganic dyes as the sensitizer, the latter of which are mainly based on Ru(II)–based transition metal complexes. When the dye molecule is excited by the absorption of sunlight, an electron is readily injected into the conduction band of $TiO_2$. The electron is then transported to the external circuit and the dye molecule is regenerated by redox reaction coupled to e.g. the $I^-/I_3^-$ ion pair in electrolyte. The mechanism of the electron injection into $TiO_2$ from the dye incorporates an ultrafast interfacial electron transfer process and is a key step in DSCs. The presence of an ultrafast electron injection suggests that the energy of LUMO of the dye should lie well above the conduction band edge of $TiO_2$ (–4.00 eV *vs*. vacuum).[2] Additionally, the HOMO energy level of the dye should be lower than the redox potential of $I^-/I_3^-$ (–4.90 eV *vs*. vacuum),[4] leading to a fast dye regeneration and avoiding the recombination of the ejected electrons back into the oxidized dye molecules. From the theoretical aspect, the dye/$TiO_2$/electrolyte interaction is complicated in practice. Interested readers can refer three recent review articles regarding theoretical approaches in dye/$TiO_2$ surface systems.[5-7]

Ru(II)–based coordination complexes are effective sensitizers for DSCs due to their lower metal-to-ligand charge transfer (MLCT) energy gap. Some DSCs incorporating Ru(II)–based sensitizers have shown incident photon-to-current conversion efficiency (IPCE) under the red and near-infrared region of the solar spectrum.[8] During the past decade, three prototypical Ru(II) dyes, N3, N719, and N749 (black dye) have been the core of Ru(II)–based dyes developed in DSCs.[3] Simulations on N3/$TiO_2$[9,10] and N719/$TiO_2$[11-14] systems have been studied by several groups. On the other hand, computational approach on the N749/$TiO_2$ model is obscure until 2012, a letter was published regarding the calculation of N749-3H/$(TiO_2)_{96}$.[15] The calculation in this letter is focused on N749-3H (with three carboxylic protons) with various protonated forms and anchoring modes of N749-3H/$(TiO_2)_{96}$.[15]

The N749 dye is an anionic complex named $\{(C_4H_9)_4N\}_3[Ru(Htctpy)(NCS)_3]$ (tctpy = 4,4′,4″-tricarboxy-2,2′:6′,2″-terpyridine), also known as the black dye.[16-21] The carboxylic groups act as anchors, which are adsorbed onto the $TiO_2$ surface. The best conversion efficiency is ~11% for DSCs with N749 as sensitizer.[18] This is mainly attributed to the property of the N749 dye that absorbs the full visible spectrum and some of the near-IR region (up to 920 nm).[17] The best IPCE achieved was reported to be 80%.[17]

From chemistry point of view, these terpyridine ligand anchored Ru(II) dyes latently

possess superior stability suited for practical applications. Despite three carboxylic groups being capable of anchoring on the $TiO_2$ surface, the N749 dye is keen on adsorbing on the $TiO_2$ surface by a bidentate and bridging coordination mode according to the experimental results, where two O atoms, each from a different carboxylate groups, attach monodentately to the Ti atoms on the $TiO_2$ surface.[19,20] In other words, two carboxylate groups are enough to create a stable adsorption site on the $TiO_2$ surface, and the third carboxylic group is dangling above the $TiO_2$ surface.[22,23] The form of "bidentate carboxylate anchoring on the Ti atoms of $TiO_2$ surface" has been examined experimentally and theoretically in Ru(II) dyes carrying bipyridine ligands with dicarboxylate groups,[9-14,22-25] in attempts to understand both the improved conversion efficiency and stability.

Research regarding terpyridine Ru(II)-based dyes in DSCs has boomed fast in recent years. An increased number of relevant dyes were reported to have great DSCs performance.[23,26-31] Recently, a series of panchromatic terpyridine Os(II)–based dyes in DSCs show high conversion efficiency reaching 8.85%.[32] Owing to the prosperity of relevant terpyridine Ru(II) dyes in DSCs, it is timely to perform the computational approach of these dyes on the $TiO_2$ surface. The unit cell of $TiO_2$ anatase (101) is $(TiO_2)_4$ and its space group is no. 141 [I 41/a m d :2]. In the $TiO_2$ anatase (101) surface nanocluster, each O atom is nearly binding with two Ti atoms. The smallest possible

reasonable $TiO_2$ anatase (101) nanocluster is $(TiO_2)_{16}$.[33] The next larger reasonable ones are $(TiO_2)_{28}$, $(TiO_2)_{38}$, and $(TiO_2)_{46}$.[34] In this chapter (Chapter I), we adopt the $(TiO_2)_{28}$ surface cluster as our simulation model. The surface area of the $(TiO_2)_{28}$ is suitable for the bidentate carboxylate groups of N749 dye to anchor onto. In particular, various deprotonated forms of model compound N749 will be carefully examined. Detail of results and discussion is elaborated in the following sections.

### 1.3 Models and Computational Methods

All the calculations are performed with the Gaussian 09 program package.[35] The ground state geometry of pure $(TiO_2)_{28}$ surface cluster and each single N749 dye are optimized first, and then each ground state geometry of N749/$(TiO_2)_{28}$ assembly is fully optimized. The ground state geometry optimizations are all performed with density functional theory (DFT) at PBE1PBE/LANL2DZ (Ru, Ti) and PBE1PBE/6-31G* (H, C, N, O, S) level. The functional PBE1PBE is weighted at 25% exchange and 75% correlation.[36] PBE had been found effective in simulating ground state geometry optimizations and absorption spectra in inorganic sensitizers and metal oxides.[11-14,37] The optimized structures of N749/$(TiO_2)_{28}$ models are then used to calculate the 60 lowest singlet electronic transitions using time dependent density functional theory (TD-DFT) method. The lowest triplet excited state energy of each model is also calculated. We adopt acetonitrile as the solvent, which is commonly used in DSCs. The solvation effect is based on the conductor-like polarizable continuum model (C-PCM), which is implemented in the Gaussian 09 program.

In the N749/$(TiO_2)_{28}$ surface models, we have performed calculation with the N749 dyes carrying 0, 1, 2, or 3 carboxylic protons. The different numbers of carboxylic protons simulated are according to the condition reported in experimental[17] and theoretical[21] (in gas phase) N749 literatures. The N749 dye carrying zero carboxylic

proton is defined as “N749-0H”, which has a charge of “–4”. Likewise, N749 dyes carrying one, two, and three carboxylic protons are dubbed as “N749-1H” (–3), “N749-2H” (–2), and “N749-3H” (–1), respectively (see Figure 1.1 for their structures). Because N749-1H has the best conversion efficiency in DSCs among these four protonation types of N749 dyes[17] and the experimental absorption spectra and FT-IR data of N749-0H/$TiO_2$, N749-1H/$TiO_2$, and N749-3H/$TiO_2$ are similar[20], we only adopt N749-1H in our experimental absorption spectrum of N749/$TiO_2$ (vide infra). The model of N749-1H/$(TiO_2)_{28}$ composite includes two forms: the protonated form “N749-1H-P/$(TiO_2)_{28}$” and the deprotonated form “N749-1H-DP/$(TiO_2)_{28}$”. The protonated form N749-1H-P/$(TiO_2)_{28}$ has retained its carboxylic proton on the third unanchored carboxylic group. The deprotonated form N749-1H-DP/$(TiO_2)_{28}$ has transferred its carboxylic proton of the N749-1H dye onto the $(TiO_2)_{28}$ surface. The N749-2H/$(TiO_2)_{28}$ composite also includes two protonation models: the protonated form “N749-2H-P/$(TiO_2)_{28}$” and the deprotonated form “N749-2H-DP/$(TiO_2)_{28}$”. The protonated N749-2H-P/$(TiO_2)_{28}$ has retained one carboxylic proton on the third unanchored carboxylic group and transferred the other one onto the $(TiO_2)_{28}$ surface. The deprotonated N749-2H-DP/$(TiO_2)_{28}$ has transferred two carboxylic protons of the N749-2H dye onto the $(TiO_2)_{28}$ surface. The N749-3H/$(TiO_2)_{28}$ composite also includes two protonation models: the protonated form “N749-3H-P/$(TiO_2)_{28}$” and the

deprotonated form "N749-3H-DP/$(TiO_2)_{28}$". The protonated N749-3H-P/$(TiO_2)_{28}$ has retained one carboxylic proton on the third unanchored carboxylic group of the dye N749-3H and transferred the other two onto the $(TiO_2)_{28}$ surface. The deprotonated N749-3H-DP/$(TiO_2)_{28}$ has transferred all the three carboxylic protons of the N749-3H dye onto the $(TiO_2)_{28}$ surface. In short, as shown in Figure 1.2, there are totally seven surface models of N749/$(TiO_2)_{28}$ to be simulated: "N749-0H/$(TiO_2)_{28}$", "N749-1H-P/$(TiO_2)_{28}$", "N749-1H-DP/$(TiO_2)_{28}$", "N749-2H-P/$(TiO_2)_{28}$", "N749-2H-DP/$(TiO_2)_{28}$", "N749-3H-P/$(TiO_2)_{28}$", and "N749-3H-DP/$(TiO_2)_{28}$". Note that in this approach we do not consider those N749/$(TiO_2)_{28}$ models in basic solution, in which the proton is dissociated without anchoring onto $TiO_2$. It has been reported that the DSCs performance is inferior in basic solution.[3]

## 1.4 Results and Discussion

### 1.4.1 $(TiO_2)_{28}$ Surface and Associated Behaviors of the N749/$(TiO_2)_{28}$ Models

We use the $(TiO_2)_{28}$ cluster as our simulation model, for which the full geometry optimized structure is depicted in Figure 1.2. The $(TiO_2)_{28}$ cluster possesses a nearly planar structure and its surface area is suitable for N749 with the bidentate bicarboxylate (of the tridentate tricarboxylate) to anchor onto. The HOMO and LUMO energy levels of the $(TiO_2)_{28}$ surface in acetonitrile are calculated to be –7.35 and –3.45 eV, respectively, deducing a HOMO-LUMO band gap of 3.90 eV. The $S_0 \rightarrow S_1$ optical gap is calculated to be 3.25 eV, which is only slightly larger than the experimental band gap of ~3.20 eV for the nano-sized (15~20 nm) $TiO_2$,[2] supporting the validity of current theoretical approach based on the $(TiO_2)_{28}$ cluster. We then focus on the adsorption energies for the N749 dyes onto $(TiO_2)_{28}$. The optimized geometries, calculated adsorption energies, and O–Ti (between carboxylate O atom and Ti atom) distances of these seven N749/$(TiO_2)_{28}$ models are shown in Figure 1.2. The adsorption energy, $E_{ads}$, is defined as $E_{ads} = E_{dye/(TiO2)28} - [E_{dye} + E_{(TiO2)28}]$ where $E_{dye/(TiO2)28}$, $E_{dye}$ and $E_{(TiO2)28}$ denote the optimized energy of the dye/$(TiO_2)_{28}$ assembly, isolated dye, and $(TiO_2)_{28}$, respectively. The adsorption is expected to be exothermic, which is a prerequisite for the formation of dye/$(TiO_2)_{28}$ due to the negative entropic change of the adsorption process. Evidently, as shown in Figure 1.2, the calculated adsorption energies of all seven

N749/$(TiO_2)_{28}$ surface models are negative; thus each N749/$(TiO_2)_{28}$ assembly is thermodynamically stable. In particular, the deprotonated form N749-1H-DP/$(TiO_2)_{28}$ (–2.98 eV) is more stable than the protonated form N749-1H-P/$(TiO_2)_{28}$ (–2.88 eV). Similar results are obtained for the two- and three-proton systems, in which N749-2H-DP/$(TiO_2)_{28}$ (–2.50 eV) and N749-3H-DP/$(TiO_2)_{28}$ (–1.95 eV) are more stable than N749-2H-P/$(TiO_2)_{28}$ (–2.35 eV) and N749-3H-P/$(TiO_2)_{28}$ (–1.86 eV), respectively. The deprotonated form is a dissociative adsorption, thus it has a larger adsorption energy than the protonated form. In addition, the O–Ti distances between the carboxylate O atoms and Ti atoms of these seven N749/$(TiO_2)_{28}$ cluster models are calculated to be within 1.89 to 1.97 Å (see Figure 1.2), which are in good agreement with the reported experimental value ranging from 1.92 to 1.97 Å.[19] We then calculate the electronic properties for each model elaborated as follows, in which N749/$(TiO_2)_{28}$ with various protonated and deprotonated forms will be discussed in detail.

### 1.4.2 Frontier Molecular Orbitals and Absorption Spectra

The electron density distributions in HOMOs and LUMOs of these seven N749/$(TiO_2)_{28}$ models show no obvious differences. The HOMOs are only located at the N749 dyes, while the LUMOs are localized at the $(TiO_2)_{28}$ surface or delocalized at the N749/$(TiO_2)_{28}$ interfaces, and the LUMOs form a nearly continuous state (see Figures 1.3 to 1.10). Furthermore, the electron distributions in HOMO and HOMO-1

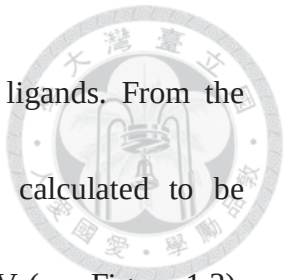

are both localized at the section between Ru(II) center and NCS ligands. From the energetics point of view, all HOMOs (oxidation potential) are calculated to be within –5.18 to –5.33 eV, and LUMOs are within –2.58 to –3.29 eV (see Figure 1.3). The $S_0 \rightarrow S_1$ optical gaps of these seven N749/$(TiO_2)_{28}$ models are also calculated, the values of which are within 1.98 eV (627.3 nm) and 1.69 eV (731.7 nm). Thus, alternatively, the LUMO energy can be estimated by adding $S_0 \rightarrow S_1$ gaps to their corresponding HOMO. The resulting LUMO energy levels are within –3.20 to –3.64 eV, which are then closer to the experimental energy level of $TiO_2$ conduction band (–4.0 eV). Nevertheless, despite which method being applied for estimating LUMO, for these seven N749/$(TiO_2)_{28}$ models all LUMOs are higher in energy than the experimental energy level of $TiO_2$ conduction band. Meanwhile, all HOMOs are lower than the experimental redox potential of $I^-/I_3^-$ (–4.9 eV). Accordingly, these seven N749/$(TiO_2)_{28}$ models are predicted to operate well in the N749 based DSCs, in good agreement with the experimental report.[17] The optical transitions of these seven N749/$(TiO_2)_{28}$ models are mainly transferring from HOMO or HOMO-1 to LUMOs, and are ascribed as an interfacial charge transfer process (see Tables 1.1, 1.2, 1.3, 1.4, 1.5, 1.6, and 1.7). The peak of the experimental N749-1H/$TiO_2$ absorption spectrum is at 599 nm (2.07 eV). The maxima of the calculated absorption spectra over 560 nm of these seven models (N749-0H/$(TiO_2)_{28}$, N749-1H-P/$(TiO_2)_{28}$, N749-1H-DP/$(TiO_2)_{28}$,

N749-2H-P/$(TiO_2)_{28}$, N749-2H-DP/$(TiO_2)_{28}$, N749-3H-P/$(TiO_2)_{28}$, and N749-3H-DP/$(TiO_2)_{28}$) are at 582.8 nm (2.13 eV), 617 nm (2.010 eV), 610.2 nm (2.03 eV), 618.3 nm (2.005 eV), 615.7 nm (2.014 eV), 638.7 nm (1.94 eV), and 598 nm (2.07 eV), respectively (see Figures 1.11, 1.12, Tables 1.1, 1.2, 1.3, 1.4, 1.5, 1.6, and 1.7). The oscillator strengths of these peaks are all larger than 0.04. This, together with the HOMO (and HOMO-1) and LUMOs being assigned to N749 and $(TiO_2)_{28}$, respectively, indicates a type of optical electron transfer process. In other words, through the complex formation between N749 and $TiO_2$ in the N749/$(TiO_2)_{28}$ systems, the coupling constant of the matrix elements must be large (>> kT) so that the interfacial transition, in part, becomes optically allowed.

The discrepancies in absorption peak frequency between the experimental and these seven calculated spectra are within 0.13 eV. In particular, the calculated maxima of the four N749-DP/$(TiO_2)_{28}$ models (for N749-0H/$(TiO_2)_{28}$, N749-1H-DP/$(TiO_2)_{28}$, N749-2H-DP/$(TiO_2)_{28}$, and N749-3H-DP/$(TiO_2)_{28}$) are in better agreement with the experimental result, as evidenced by the fact that differences between the experimental and the calculated peaks of the four N749-DP/$(TiO_2)_{28}$ are only within 0.06 eV (see Figures 1.11, 1.12, Tables 1.1, 1.2, 1.3, 1.4, 1.5, 1.6, and 1.7).

The calculated absorption maximum of N749-1H-DP/$(TiO_2)_{28}$ is at 617 nm ($S_0 \rightarrow S_2$ transition) with an oscillator strength of 0.06, which comprises three components;

namely: 1) HOMO → LUMO, 2) HOMO → LUMO+1, and 3) HOMO → LUMO+6 (see Table S1.3). Figure 1.13 depicts the combination of HOMO and LUMO+6 to illustrate the transition properties. LUMO+6 is picked due to its largest delocalization of electron density in both N749-1H-DP and $(TiO_2)_{28}$. Along this line, photoexcitation from HOMO (N749-1H-DP) to LUMO+6, in which electron densities are distributed around the interface of N749-1H-DP/$(TiO_2)_{28}$ (see Figure 1.13), exhibits an electron-hole charge transfer transition with a substantially strong oscillator strength. The net result can be equivalently described as processing an instantaneously interfacial electron injection fitted to a well established "direct injection" mechanism.[9,14] Similar transition patterns at the absorption maxima are obtained for the rest six N749/$(TiO_2)_{28}$ models and the corresponding molecular orbital illustrations are depicted in Figures 1.14, 1.15, 1.16, 1.17, 1.18, and 1.19.

Further careful examination on Figure 1.3 indicates that the HOMO-LUMO band gaps and the first singlet excited state energies ($S_0 \rightarrow S_1$) do not have the same trend of correlation among the seven N749/$(TiO_2)_{28}$ models studied. For clarity, a fair comparison is made by classifying the titled nanocomposites into three subgroups. First, in section 1.4.2.1 we discuss the N749-DP/$(TiO_2)_{28}$ model for cases of 0-, 1-, 2- and 3-H (vide supra). We then present the N749-P/$(TiO_2)_{28}$ models for 1-, 2- and 3-H in section 1.4.2.2. Lastly, under the restriction that one proton has to reside at the

carboxylic site, comparative study has been carried out between the rest protons on the carboxylic groups and on the $(TiO_2)_{28}$ sites. In other words, focus on section 1.4.2.3 will be for 1H-P *vs*. 1H-DP, 2H-P *vs*. 2H-DP and 3H-P *vs*. 3H-DP (for detailed definition, see section 1.3).

#### 1.4.2.1 N749-0H/$(TiO_2)_{28}$, N749-1H-DP/$(TiO_2)_{28}$, N749-2H-DP/$(TiO_2)_{28}$, *vs.* N749-3H-DP/$(TiO_2)_{28}$

The orbital energy levels of HOMOs and LUMOs of these four N749-DP/$(TiO_2)_{28}$ models (see Figure 1.3) show a notable correlation with the number of protons. They are related in that the increase of proton number associates with a decrease of both HOMOs and LUMOs, and the energy gap between HOMO and LUMO is decreased as well. This results can be rationalized by the fact that adding more protons on the $(TiO_2)_{28}$ surface leads to the progressively build-up of the positive charge. The greater potential gradient is then formed between the negatively charged N749 dyes and the positively charged $(TiO_2)_{28}$ surface, resulting in the decrease of both HOMOs and LUMOs energy levels.[38] It should also be noted that the decrease of HOMO energy is not as significant as the decrease of LUMO energy. As a result, the individual HOMO–LUMO energy gap $E_{H-L}$ exhibits a sequential red-shift with increasing number of protons, the result of which is in agreement with the theoretical study of N749 in gas phase.[21] All these four N749-DP/$(TiO_2)_{28}$ models carry none of carboxylic proton in the N749 dyes. Evidently,

LUMOs reside on $(TiO_2)_{28}$ and thus are much more affected by the transferred protons. On the other hand, the HOMOs residing only at the main framework of the N749 dye are less affected by the protons on the $(TiO_2)_{28}$ cluster. Similarly, upon increasing number of protons, the corresponding $S_0 \rightarrow S_1$ energy gaps are red shifted in the order of 627.3 nm (0), 651.3 nm (1), 659.6 nm (2), and 731.7 nm (3) (see Figure 1.3, Tables 1.1, 1.3, 1.5, and 1.7).

#### 1.4.2.2 N749-1H-P/$(TiO_2)_{28}$, N749-2H-P/$(TiO_2)_{28}$, *vs*. N749-3H-P/$(TiO_2)_{28}$

With the increase of the proton number, these three protonated N749-P/$(TiO_2)_{28}$ models have the same trends as the four N749-DP/$(TiO_2)_{28}$ models (see Figure 1.3), that is the decrease of the energy levels of HOMOs and LUMOs results in decrease of both HOMO–LUMO band gap and $S_0$–$S_1$ energy gap. Note that all these three N749-P/$(TiO_2)_{28}$ models carry one carboxylic proton on the N749 dye, while the rest protons reside on $(TiO_2)_{28}$. Since both HOMOs and LUMOs energy levels are greatly affected by the potential gradient built between N749 (negatively charged) and $(TiO_2)_{28}$ (positively charged),[38] similar trend in energetic relationship for N749-1H-P/$(TiO_2)_{28}$ (no proton on $TiO_2$), N749-2H-P/$(TiO_2)_{28}$ (one proton) and N749-3H-P/$(TiO_2)_{28}$ (two protons) is expected and can be rationalized by the same reasons given for the four N749-DP/$(TiO_2)_{28}$ models discussed above (see section 1.4.2.1).

#### 1.4.2.3 N749-nH-P/$(TiO_2)_{28}$ *vs*. N749-nH-DP/$(TiO_2)_{28}$ (n = 1, 2, 3)

The energy level of LUMO of N749-1H-DP/$(TiO_2)_{28}$ (–2.84 eV) is lower than N749-1H-P/$(TiO_2)_{28}$ (–2.70 eV), while the energy level of HOMO of N749-1H-DP/$(TiO_2)_{28}$ (–5.23 eV) is higher than N749-1H-P/$(TiO_2)_{28}$ (–5.33 eV) (see Figure 1.3). In comparison to the protonated form N749-1H-P/$(TiO_2)_{28}$, the deprotonated form N749-1H-DP/$(TiO_2)_{28}$ leads to a downshift of LUMO and up-shift of HOMO. The downshift of LUMO is mainly due to the fact that the $(TiO_2)_{28}$ cluster in N749-1H-DP/$(TiO_2)_{28}$ carries more positive charge than that of $(TiO_2)_{28}$ in N749-1H-P/$(TiO_2)_{28}$. Conversely, N749-1H-DP in N749-1H-DP/$(TiO_2)_{28}$ carries more negative charge than that of N749-1H-P in N749-1H-P/$(TiO_2)_{28}$, resulting in an up-shift of HOMO. As a result, N749-1H-DP/$(TiO_2)_{28}$ has a smaller HOMO-LUMO band gap than that of N749-1H-P/$(TiO_2)_{28}$. Similarly, N749-1H-DP/$(TiO_2)_{28}$ has a smaller $S_0$–$S_1$ energy gap than N749-1H-P/$(TiO_2)_{28}$ (see Figure 1.3, Tables 1.2, and 1.3). The trends of both HOMO–LUMO and $S_0$–$S_1$ gaps are in good agreement with the theoretical approach using N719/$(TiO_2)_{38}$ as a model.[12] For the two- and three-proton systems, as shown in Figure 1.3, both N749-2H-P/$(TiO_2)_{28}$ *vs.* N749-2H-DP/$(TiO_2)_{28}$ and N749-3H-P/$(TiO_2)_{28}$ *vs.* N749-3H-DP/$(TiO_2)_{28}$ follow the same trend regarding HOMO–LUMO band gap and $S_0$–$S_1$ energy gap, which can be well explained by the same reasons given for N749-1H-P/$(TiO_2)_{28}$ *vs.* N749-1H-DP/$(TiO_2)_{28}$.

### 1.4.3 Theoretical *vs.* Experimental Approach

We then make a fair comparison between theoretical and experimental approaches. As for one-proton models, Figure 1.20 displays the absorption spectrum of N749-1H/$TiO_2$ together with the calculated spectra of N749-1H-P/$(TiO_2)_{28}$ and N749-1H-DP/$(TiO_2)_{28}$. The calculated lowest singlet excitation peak wavelength $\lambda_{S0\text{-}S1}$ of N749-1H-DP/$(TiO_2)_{28}$ (651.3 nm; also see Table 1.3) is red shifted relative to that (647.5 nm) of N749-1H-P/$(TiO_2)_{28}$ (see Table 1.2). In particular, N749-1H-P/$(TiO_2)_{28}$ has another prominent absorption peak at 534.1 nm ($S_0 \rightarrow S_5$) with strong oscillator strength of 0.05. As a result, the calculated spectrum of the deprotonated form N749-1H-DP/$(TiO_2)_{28}$ matches the experimental spectrum (with oscillator strengths distributed) better than that of the protonated form N749-1H-P/$(TiO_2)_{28}$ in the range of 450 nm to 950 nm (see Figure 1.20).

Similar results are also found for two- and three-proton models, in which the calculated absorption spectral maxima of the four deprotonated N749-DP/$(TiO_2)_{28}$ models are better in overlapping with the experimental absorption spectrum than those three protonated N749-P/$(TiO_2)_{28}$ models (see Figures 1.4 and 1.5). Also, the calculated absorption spectra of N749-2H-P/$(TiO_2)_{28}$ and N749-3H-P/$(TiO_2)_{28}$ reveal additional lower lying peak at 549.4 and 537.3 nm with oscillator strength of 0.046 and 0.02, respectively, resulting in an inferior overlap (with oscillator strengths distributed) with respect to the experimental spectrum. For clarity, Figures 1.21 and 1.22 show a fair

comparison among relevant spectra for the two- and three-proton models, respectively.

The above results seems contradictory to the most recent calculation using N749-3H/$(TiO_2)_{96}$ as a model.[15] Applying CPMD (geometry optimization) and Gaussian 09 (TD-DFT for excitation) for the N749-3H/$(TiO_2)_{96}$ model, Sodeyama et al.[15] calculated the protonated form of N749-3H/$(TiO_2)_{96}$ to be more stable than the deprotonated form, with its corresponding spectrum being closer to the experimental absorption spectra. In the current study, applying Gaussian 09 for full geometry optimization and excitation simulation, several remarks extracted from our results lead us to cast the alternative viewpoint that the N749 deprotonated forms should be the dominant species upon anchoring onto $TiO_2$ nanocluster. Our viewpoint stems from the combination of aforementioned adsorption energies, resemblance of absorption onset and maxima as well as spectral feature in terms of oscillator strengths with respect to the experimental observation.[20] Moreover, all of the frontier molecular orbital graphs of HOMOs and LUMOs of the seven N749/$(TiO_2)_{28}$ models have been displayed, in which the electron charge distributions of all HOMOs are located at the N749 dyes, and LUMOs are localized at the $(TiO_2)_{28}$ surface or delocalized at the interfacial regions of N749/$(TiO_2)_{28}$. This is consistent with the calculated results of N719/$(TiO_2)_{82}$.[13,14] We thus conclude that the N749 deprotonated forms should be the dominant species upon anchoring onto the $(TiO_2)_{28}$ cluster, and simultaneously the protons are co-adsorbed on

the $TiO_2$ surface adjacent to the carboxylate group. This comprises a composite framework in mimicking the DSCs configuration. The result is also in agreement with the conclusion drawn according to the experimental progress. Experimentally, both UV-Vis and FT-IR absorption spectra of N749-0H/$TiO_2$, N749-1H/$TiO_2$ and N749-3H/$TiO_2$ resemble each other, indicating that the N749 deprotonated form should be the prevailing species, and the dissociated carboxylic protons are coadsorbed onto the $TiO_2$ surface.[20]

Last but not least, the above delineation is mainly in the singlet manifold. As for the Ru(II)–based dyes in DSCs, due to the heavy atom enhanced spin–orbit coupling and hence the facilitation of rate of intersystem crossing, the lowest triplet state ($T_1$) may be populated, which may also play a role for the electron injection processes.[39] We have thus calculated the $S_0$–$T_1$ energies of the seven N749/$(TiO_2)_{28}$ models and the results are shown in Figure 1.3. Evidently, the onsets of the calculated transition for the seven models are all in the near IR, ranging from 794.2 nm to 951 nm, accounting for the tail of spectral onset for N749 adsorbed onto $TiO_2$.

## 1.5 Conclusion

In summary, we provide a compact but efficient model incorporating $(TiO_2)_{28}$ assembly for accessing the adsorption of the N749 dyes with terpyridine anchoring group. Seven distinctive N749/$(TiO_2)_{28}$ surface models are investigated with the Gaussian 09 software package. Various properties of the N749/$(TiO_2)_{28}$ models, such as optimized structures, O–Ti distances, adsorption energies, frontier molecular orbitals, and TD-DFT UV-VIS excitation spectra have been calculated and a fair comparison with the experimental results have been made. Among these seven N749/$(TiO_2)_{28}$ models, the combination of the adsorption energy onto $TiO_2$ and experimental and calculated absorption spectra concludes that the deprotonated dyes constitute the most favorable and dominant structure in the DSCs devices. The frontier molecular orbital graphs indicate that the electron charge distribution of all HOMOs are located at the N749 dyes and LUMOs are localized at the $(TiO_2)_{28}$ surface or delocalized at the interfacial regions of N749/$(TiO_2)_{28}$. The corresponding transitions are thus more like a type of optical electron transfer, injecting the electron to the interfacial $TiO_2$. The interfacial charge transfer processes of the seven N749/$(TiO_2)_{28}$ models are also shown. We also have comprehensively discussed the energy level positions of HOMOs and LUMOs of these seven N749/$(TiO_2)_{28}$ models, accounting for their relationships with

the number of protons. Accordingly, we have demonstrated that the selection of suitable $(TiO_2)_{28}$ assembly can be used to simulate real-life experimental data with good reliability. Due to the readily accessible in computation capability for most of laboratories, new and more efficient Ru(II) sensitizers may be strategically designed via simulation prior to the execution of synthetic work, saving the redundant synthetic efforts and suited for the demand of vast evaluation of the DSCs sensitizers.

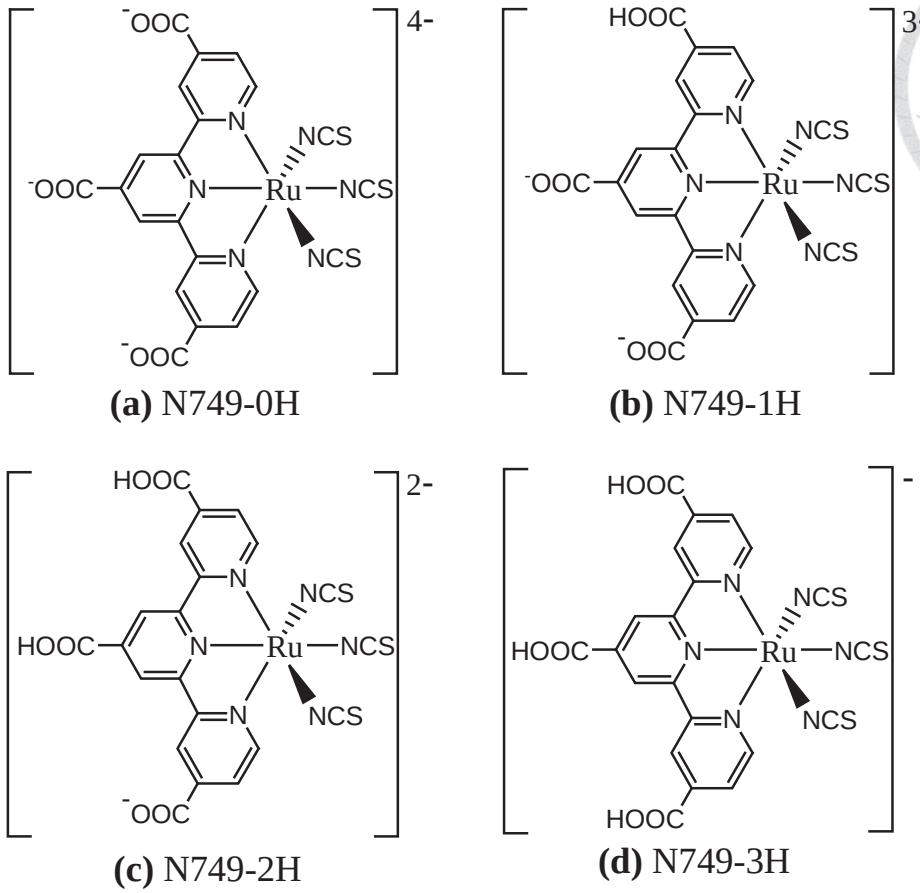


**Figure 1.1** Molecular structures of various N749 dyes: (a) N749-0H, (b) N749-1H, (c) N749-2H, and (d) N749-3H.

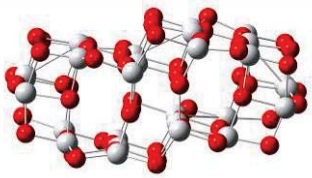

$(TiO_2)_{28}$

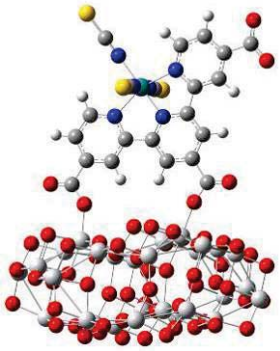

N749-0H/$(TiO_2)_{28}$
O–Ti = 1.95 and 1.94 Å
$E_{ads}$ = –3.15 eV

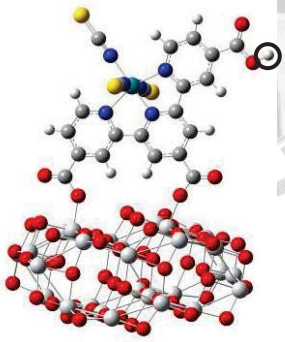

N749-1H-P/$(TiO_2)_{28}$
O–Ti = 1.97 and 1.95 Å
$E_{ads}$ = –2.88 eV

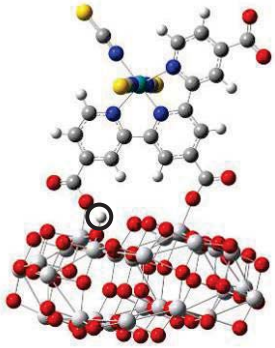

N749-1H-DP/$(TiO_2)_{28}$
O–Ti = 1.94 and 1.92 Å
$E_{ads}$ = –2.98 eV

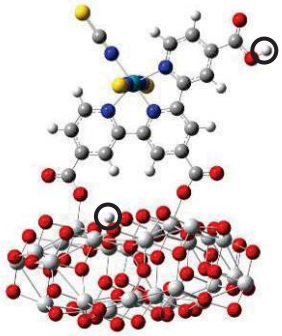

N749-2H-P/$(TiO_2)_{28}$
O–Ti = 1.94 and 1.93 Å
$E_{ads}$ = –2.35 eV

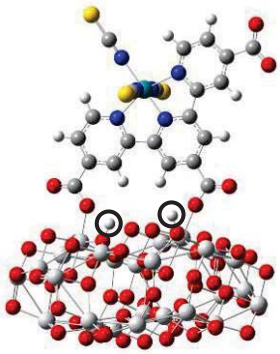

N749-2H-DP/$(TiO_2)_{28}$
O–Ti = 1.97 and 1.91 Å
$E_{ads}$ = –2.50 eV

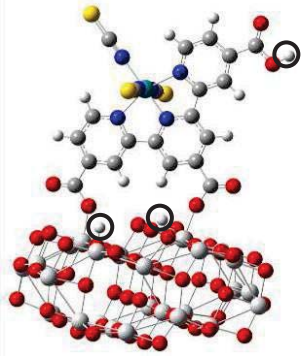

N749-3H-P/$(TiO_2)_{28}$
O–Ti = 1.92 and 1.93 Å
$E_{ads}$ = –1.86 eV

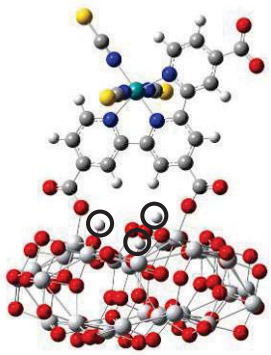

N749-3H-DP/$(TiO_2)_{28}$
O–Ti = 1.96 and 1.89 Å
$E_{ads}$ = –1.95 eV

**Figure 1.2** Optimized geometries, O–Ti distances (left and right side), and adsorption energies of the $(TiO_2)_{28}$ cluster and seven N749/$(TiO_2)_{28}$ models. Note: The carboxylic protons and protons on the $(TiO_2)_{28}$ surface are indicated by circle symbol.

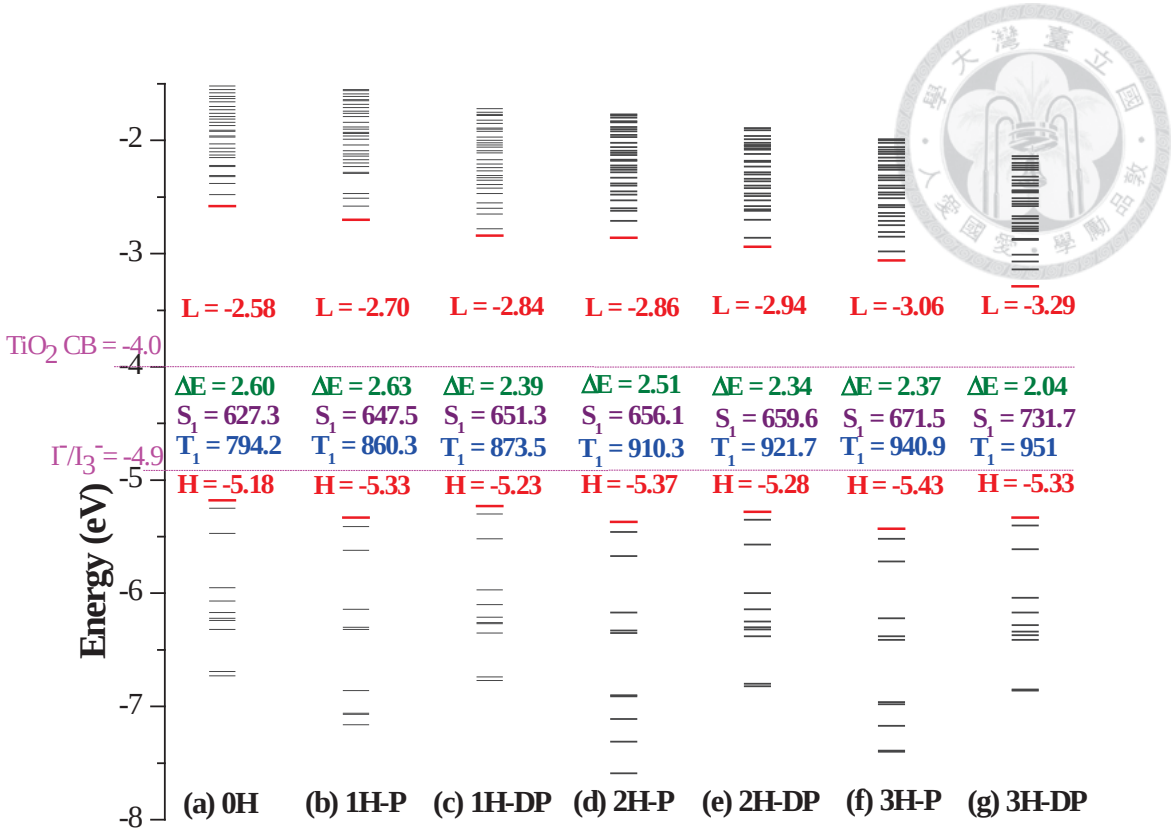


**Figure 1.3** Molecular orbital energy level (eV) diagram from HOMO-10 to LUMO+30 of the seven N749/$(TiO_2)_{28}$ surface models. (a) N749-0H/$(TiO_2)_{28}$, (b) N749-1H-P/$(TiO_2)_{28}$, (c) N749-1H-DP/$(TiO_2)_{28}$, (d) N749-2H-P/$(TiO_2)_{28}$, (e) N749-2H-DP/$(TiO_2)_{28}$, (f) N749-3H-P/$(TiO_2)_{28}$, and (g) N749-3H-DP/$(TiO_2)_{28}$. CB = conduction band, H = HOMO, L = LUMO, and ΔE is HOMO–LUMO band gap. $S_1$ and $T_1$ stand for the calculated first singlet and the lowest triplet excited state energies in nm, respectively.

| | | |
|---|---|---|
| 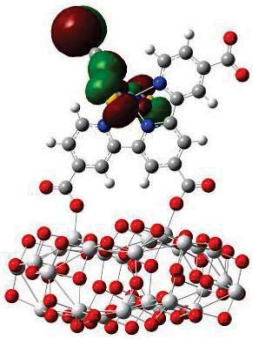 HOMO-4 (-6.07 eV) | 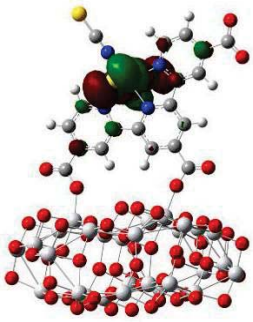 HOMO-1 (-5.25 eV) | 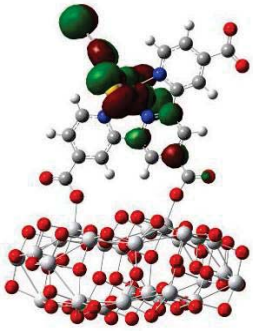 HOMO (-5.18 eV) |
| 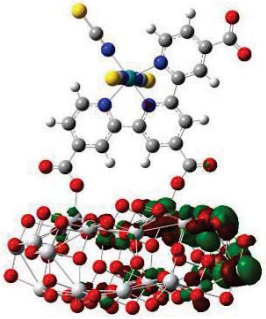 LUMO (-2.58 eV) | 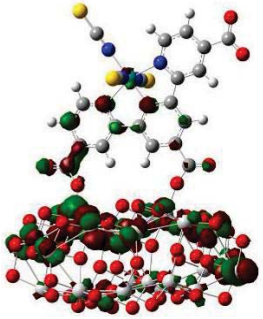 LUMO+1 (-2.48 eV) | 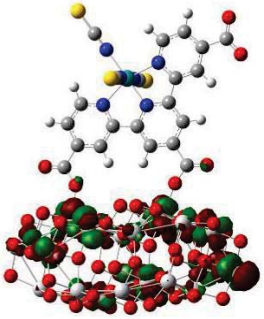 LUMO+2 (-2.38 eV) |
| 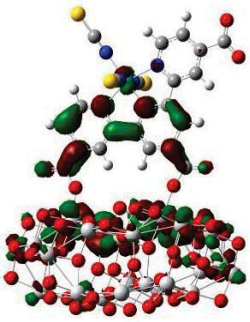 LUMO+3 (-2.32 eV) | 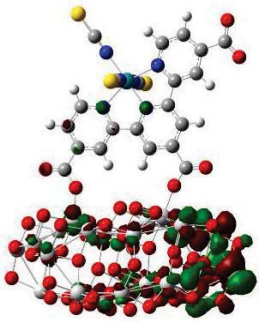 LUMO+4 (-2.31 eV) | 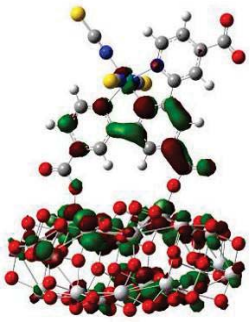 LUMO+5 (-2.23 eV) |
|  LUMO+6 (-2.22 eV) | 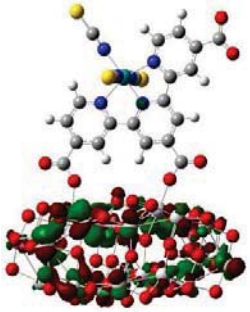 LUMO+7 (-2.15 eV) | 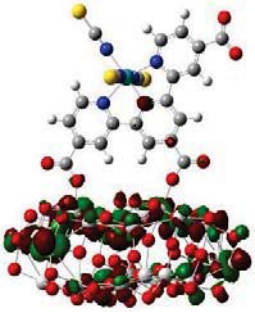 LUMO+8 (-2.13 eV) |

**Figure 1.4.1** Frontier molecular orbitals pertinent to the singlet optical transitions in selected states for N749-0H/$(TiO_2)_{28}$. The isovalue for the contours is 0.02.

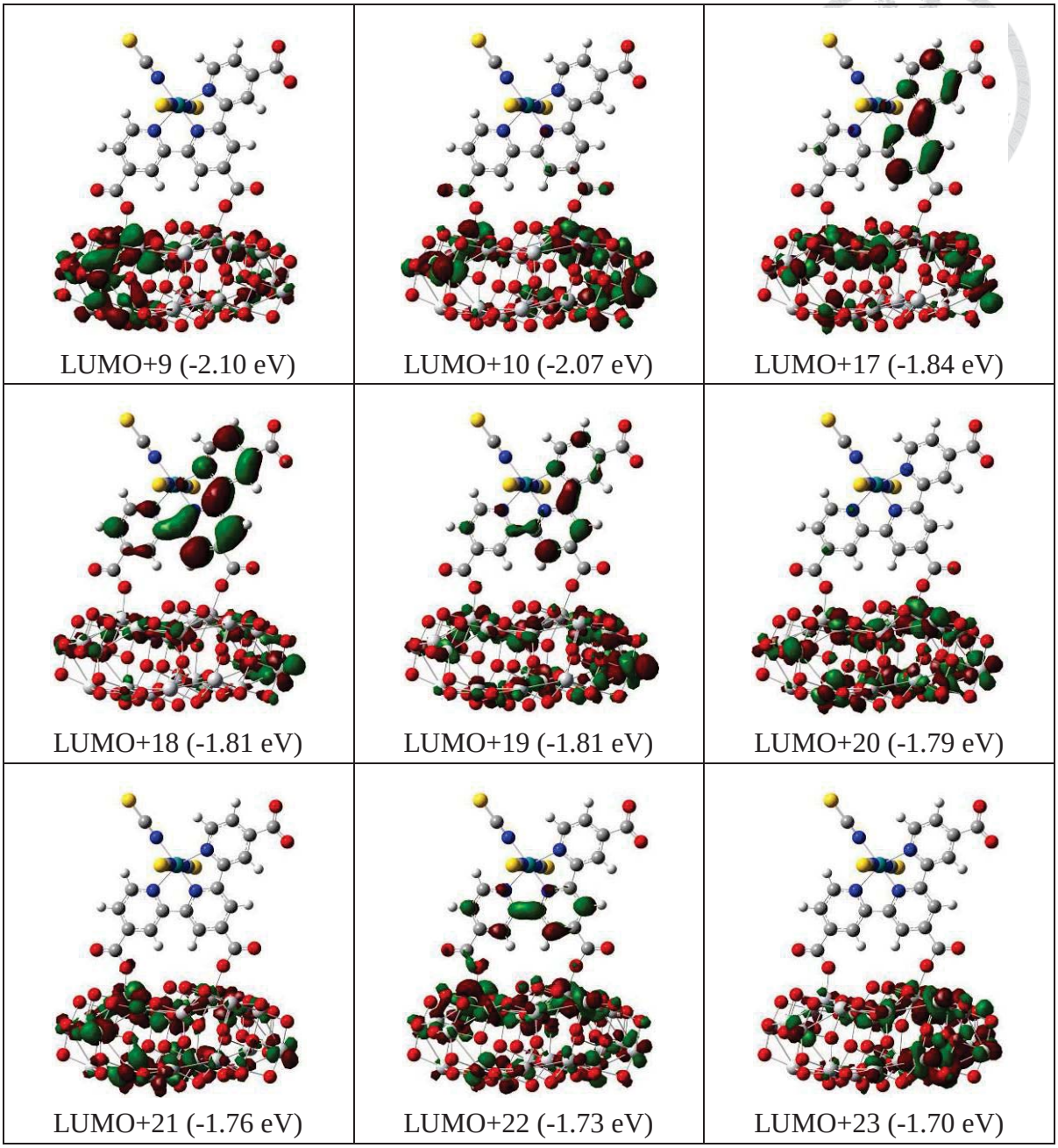


**Figure 1.4.2** Frontier molecular orbitals pertinent to the singlet optical transitions in selected states for N749-0H/$(TiO_2)_{28}$. The isovalue for the contours is 0.02.

**Table 1.1** The wavelengths, transition probabilities and charge transfer characters of the singlet optical transitions in selected states with oscillator strength > 0.003 for N749-0H/$(TiO_2)_{28}$. *f* is oscillator strength.

| State | $\lambda_{cal}$ (nm) | *f* | Assignments |
|---|---|---|---|
| 1 | 627.3 | 0.0142 | HOMO-1→LUMO+3(24%) HOMO-1→LUMO+1(18%) HOMO-1→LUMO+5(16%) HOMO-1→LUMO+6(14%) HOMO-1→LUMO(6%) |
| 2 | 582.8 | 0.0935 | HOMO→LUMO+1(25%) HOMO→LUMO+3(20%) HOMO→LUMO(13%) HOMO→LUMO+5(10%) HOMO→LUMO+6(10%) |
| 7 | 509.1 | 0.0051 | HOMO-1→LUMO+1(42%) HOMO→LUMO+2(18%) HOMO→LUMO+3(6%) HOMO→LUMO+1(6%) |
| 8 | 506.3 | 0.0083 | HOMO→LUMO+2(43%) HOMO-1→LUMO+1(31%) HOMO-1→LUMO+3(6%) |
| 9 | 494.9 | 0.0177 | HOMO→LUMO+2(31%) HOMO→LUMO+18(21%) HOMO→LUMO+17(10%) HOMO→LUMO+19(7%) HOMO→LUMO+3(5%) |
| 10 | 490.4 | 0.0061 | HOMO-1→LUMO+2(76%) |
| 15 | 472.3 | 0.0114 | HOMO-1→LUMO+4(62%) HOMO-1→LUMO+18(8%) HOMO-1→LUMO+2(5%) |
| 17 | 468 | 0.021 | HOMO-1→LUMO+18(24%) HOMO-1→LUMO+4(19%) HOMO-1→LUMO+17(10%) HOMO-1→LUMO+6(9%) HOMO-1→LUMO+5(8%) HOMO-1→LUMO+19(8%) |
| 21 | 458.4 | 0.0055 | HOMO→LUMO+8(59%) HOMO→LUMO+7(26%) |
| 26 | 446.4 | 0.0056 | HOMO→LUMO+10(82%) HOMO→LUMO+8(8%) |
| 30 | 435.6 | 0.0048 | HOMO-1→LUMO+10(82%) HOMO-1→LUMO+8(10%) |
| 48 | 407.7 | 0.005 | HOMO→LUMO+20(63%) HOMO→LUMO+21(6%) HOMO→LUMO+22(5%) |
| 57 | 398.6 | 0.0044 | HOMO-1→LUMO+20(61%) HOMO-1→LUMO+22(9%) HOMO-1→LUMO+21(7%) |
| 58 | 396.8 | 0.004 | HOMO-1→LUMO+19(41%) HOMO-1→LUMO+22(39%) |
| 59 | 395.5 | 0.0059 | HOMO-4→LUMO+1(20%) HOMO-4→LUMO(17%) HOMO-4→LUMO+3(10%) HOMO→LUMO+23(7%) HOMO-4→LUMO+5(5%) |
| 60 | 395 | 0.0039 | HOMO-1→LUMO+19(27%) HOMO-1→LUMO+18(24%) |

| | | |
|---|---|---|
| 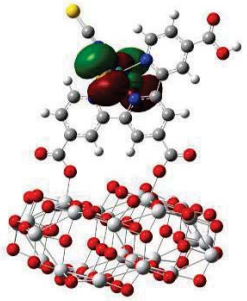 HOMO-5 (-6.32 eV) | 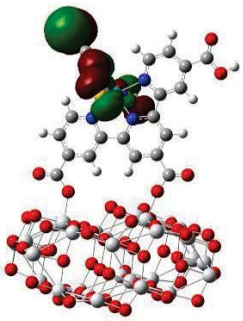 HOMO-3 (-6.14 eV) | 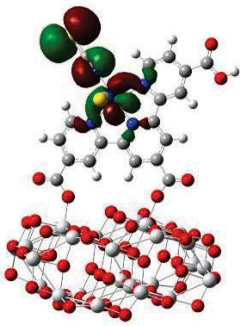 HOMO-2 (-5.62 eV) |
| 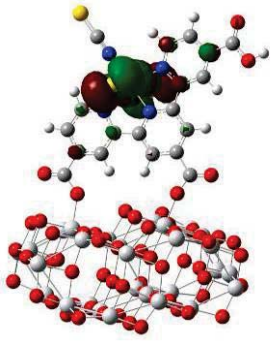 HOMO-1 (-5.41 eV) | 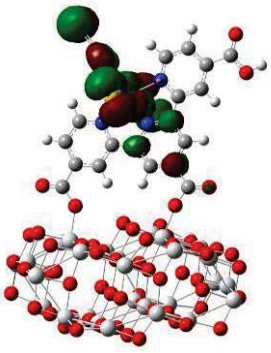 HOMO (-5.33 eV) | 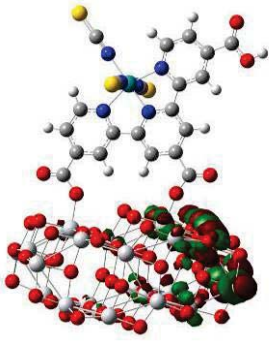 LUMO (-2.70 eV) |
| 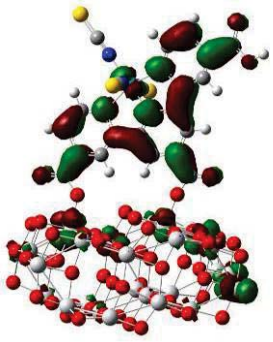 LUMO+1 (-2.58 eV) | 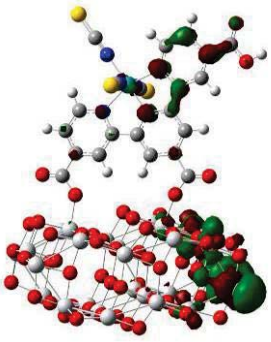 LUMO+2 (-2.51 eV) | 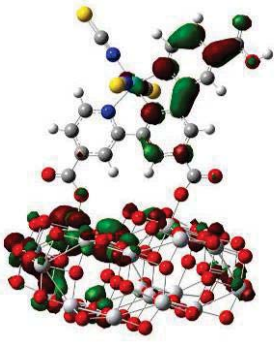 LUMO+3 (-2.47 eV) |
| 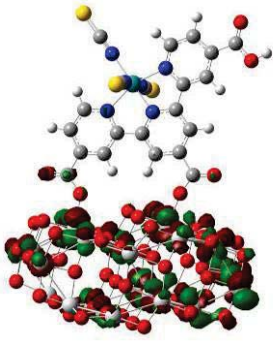 LUMO+4 (-2.29 eV) | 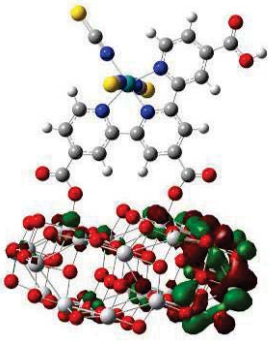 LUMO+5 (-2.28 eV) |  LUMO+6 (-2.23 eV) |

**Figure 1.5.1** Frontier molecular orbitals pertinent to the singlet optical transitions in selected states for N749-1H-P/$(TiO_2)_{28}$. The isovalue for the contours is 0.02.

| | | |
|---|---|---|
| 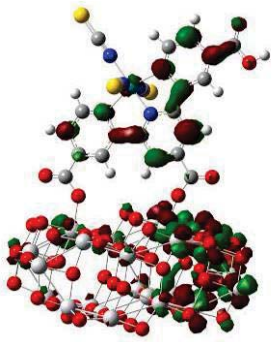 LUMO+7 (-2.20 eV) | 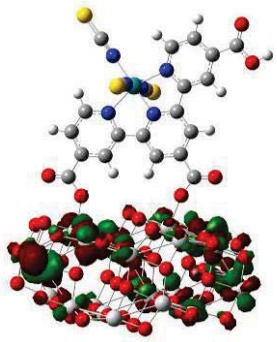 LUMO+8 (-2.17 eV) | 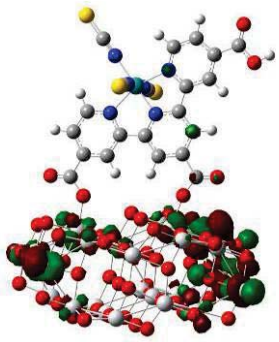 LUMO+9 (-2.14 eV) |
| 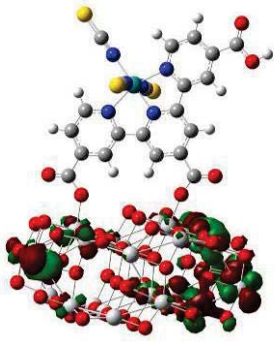 LUMO+10 (-2.12 eV) |  LUMO+11 (-2.09 eV) | 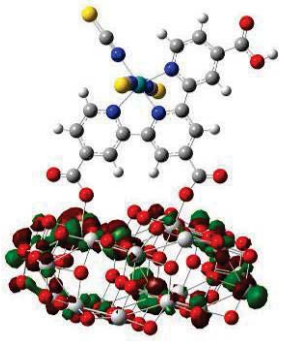 LUMO+12 (-2.04 eV) |
| 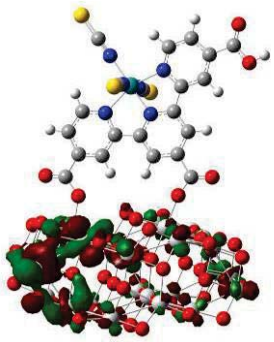 LUMO+14 (-1.96 eV) | 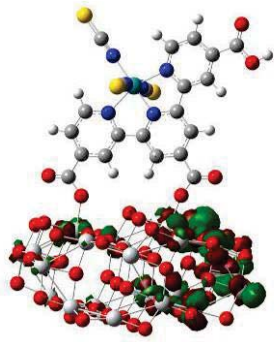 LUMO+15 (-1.94 eV) | 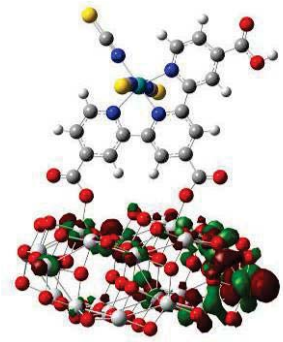 LUMO+16 (-1.93 eV) |
| 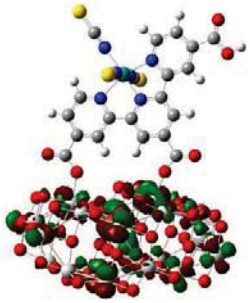 LUMO+18 (-1.88 eV) | 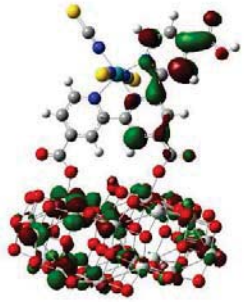 LUMO+22 (-1.74 eV) |  LUMO+24 (-1.68 eV) |

**Figure 1.5.2** Frontier molecular orbitals pertinent to the singlet optical transitions in selected states for N749-1H-P/$(TiO_2)_{28}$. The isovalue for the contours is 0.02

**Table 1.2** The wavelengths, transition probabilities and charge transfer characters of the singlet optical transitions in selected states with oscillator strength > 0.005 for N749-1H-P/$(TiO_2)_{28}$.

| State | $\lambda_{cal}$ (nm) | $f$ | Assignments |
|---|---|---|---|
| 1 | 647.5 | 0.0367 | HOMO-1→LUMO+1(49%) HOMO→LUMO+1(14%) HOMO-1→LUMO+3(13%) HOMO-1→LUMO+2(9%) |
| 2 | 617 | 0.042 | HOMO→LUMO+1(46%) HOMO-1→LUMO+1(16%) HOMO→LUMO+3(11%) HOMO→LUMO+2(8%) |
| 4 | 547.7 | 0.0109 | HOMO→LUMO(87%) |
| 5 | 534.1 | 0.0513 | HOMO→LUMO+6(24%) HOMO→LUMO+11(22%) HOMO→LUMO+7(16%) HOMO→LUMO+3(9%) HOMO→LUMO(9%) HOMO→LUMO+1(9%) |
| 7 | 501.2 | 0.0136 | HOMO→LUMO+1(19%) HOMO-1→LUMO+6(15%) HOMO→LUMO+3(15%) HOMO-1→LUMO+3(14%) HOMO-1→LUMO+11(13%) HOMO-1→LUMO+7(10%) |
| 9 | 491.4 | 0.0102 | HOMO→LUMO+3(50%) HOMO→LUMO+2(31%) |
| 14 | 463.3 | 0.0133 | HOMO→LUMO+4(65%) HOMO→LUMO+5(23%) |
| 16 | 449.5 | 0.0145 | HOMO-1→LUMO+4(65%) HOMO-1→LUMO+5(23%) |
| 19 | 439.8 | 0.0108 | HOMO→LUMO+7(36%) HOMO→LUMO+11(33%) HOMO→LUMO+22(6%) HOMO→LUMO+24(6%) |
| 25 | 429.4 | 0.0131 | HOMO→LUMO+10(43%) HOMO→LUMO+24(12%) HOMO→LUMO+9(11%) HOMO→LUMO+22(7%) |
| 26 | 427.6 | 0.0102 | HOMO→LUMO+10(46%) HOMO→LUMO+11(12%) HOMO→LUMO+24(8%) HOMO→LUMO+22(6%) |
| 27 | 425.7 | 0.0104 | HOMO-1→LUMO+11(29%) HOMO-1→LUMO+7(27%) |
| 31 | 416.9 | 0.0204 | HOMO-1→LUMO+10(28%) HOMO-1→LUMO+9(17%) HOMO-3→LUMO+1(16%) HOMO-1→LUMO+24(9%) HOMO-1→LUMO+22(6%) |
| 32 | 415.8 | 0.0206 | HOMO-3→LUMO+1(39%) HOMO-1→LUMO+10(37%) HOMO-3→LUMO+3(7%) HOMO-3→LUMO+2(6%) |
| 35 | 414 | 0.0176 | HOMO-1→LUMO+10(19%) HOMO-2→LUMO+4(13%) HOMO-3→LUMO+1(10%) HOMO-1→LUMO+11(9%) HOMO-1→LUMO+24(9%) HOMO-1→LUMO+22(7%) |
| 43 | 402.1 | 0.0059 | HOMO→LUMO+18(31%) HOMO-5→LUMO+1(16%) HOMO→LUMO+16(12%) HOMO→LUMO+15(11%) |

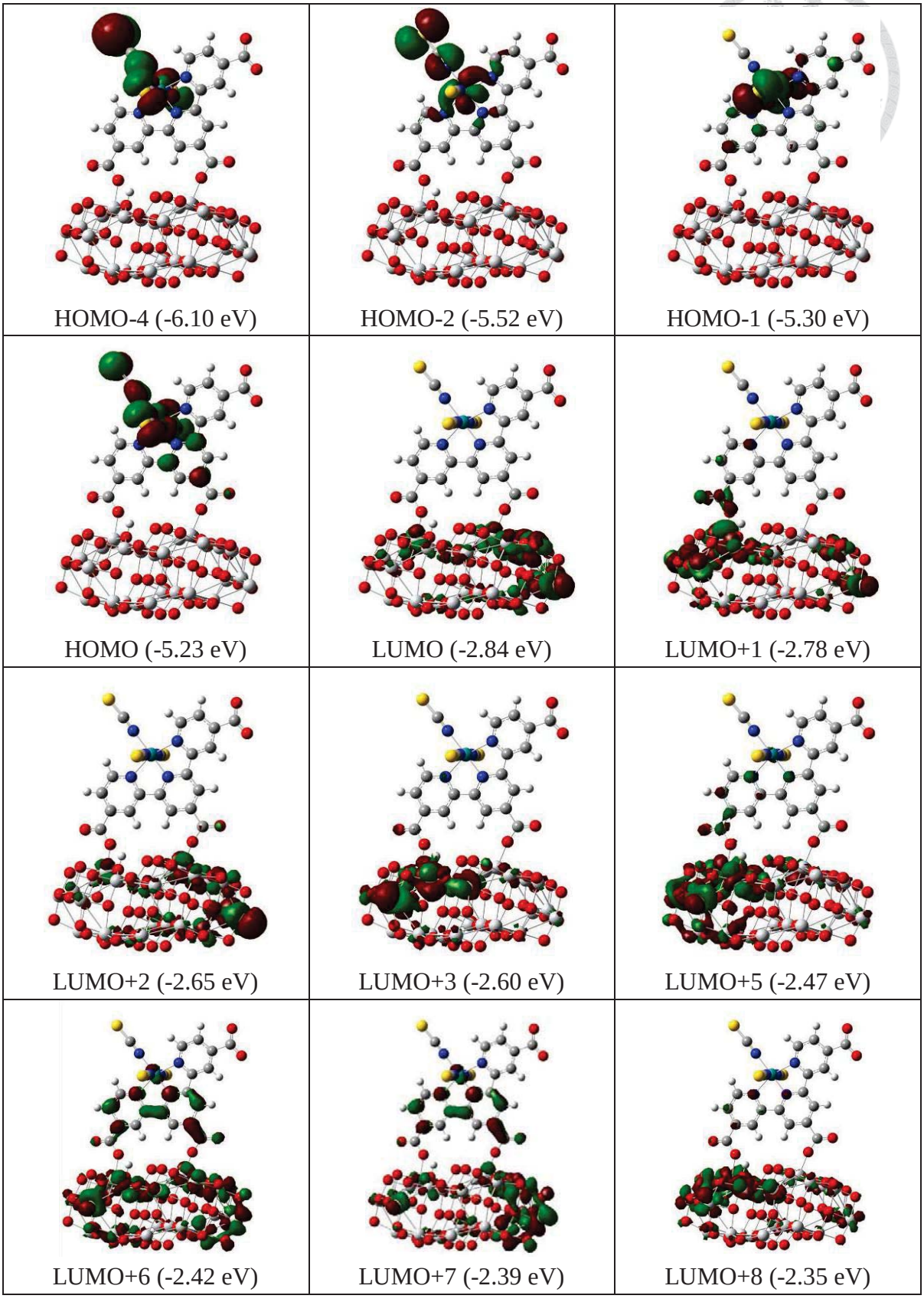


**Figure 1.6.1** Frontier molecular orbitals pertinent to the singlet optical transitions in selected states for N749-1H-DP/$(TiO_2)_{28}$. The isovalue for the contours is 0.02.

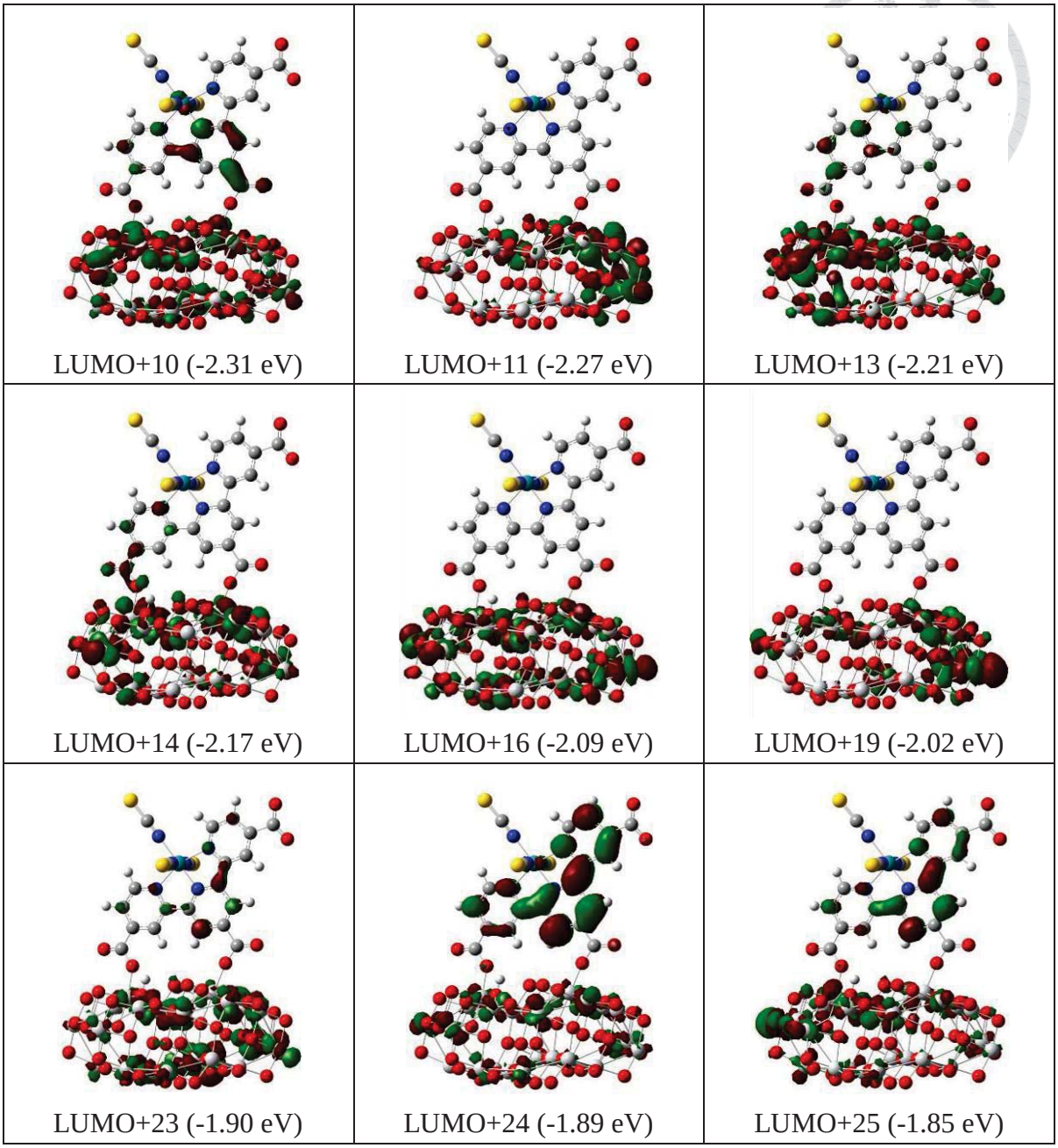


**Figure 1.6.2** Frontier molecular orbitals pertinent to the singlet optical transitions in selected states for N749-1H-DP/$(TiO_2)_{28}$. The isovalue for the contours is 0.02.

**Table 1.3** The wavelengths, transition probabilities and charge transfer characters of the singlet optical transitions in selected states with oscillator strength > 0.001 for N749-1H-DP/$(TiO_2)_{28}$.

| State | $\lambda_{cal}$ (nm) | *f* | Assignments |
|---|---|---|---|
| 1 | 651.3 | 0.0115 | HOMO-1→LUMO+6(15%) HOMO-1→LUMO+1(15%) HOMO-1→LUMO+7(13%) HOMO-1→LUMO(11%) HOMO-1→LUMO+10(8%) HOMO-1→LUMO+5(5%) |
| 2 | 610.2 | 0.0611 | HOMO→LUMO(37%) HOMO→LUMO+1(31%) HOMO→LUMO+6(25%) |
| 3 | 593.4 | 0.0013 | HOMO→LUMO(55%) HOMO→LUMO+1(38%) |
| 6 | 568.2 | 0.0156 | HOMO-1→LUMO+1(25%) HOMO-1→LUMO(8%) HOMO→LUMO+1(8%) HOMO→LUMO+6(7%) HOMO→LUMO+7(6%) |
| 7 | 563.2 | 0.0299 | HOMO-1→LUMO+1(43%) HOMO→LUMO+1(10%) HOMO→LUMO+6(8%) HOMO→LUMO+7(7%) |
| 10 | 529.3 | 0.0062 | HOMO-1→LUMO+2(67%) HOMO-1→LUMO+3(22%) |
| 14 | 510.9 | 0.0033 | HOMO→LUMO+5(69%) HOMO→LUMO+6(6%) |
| 17 | 499.1 | 0.0183 | HOMO→LUMO+24(30%) HOMO-1→LUMO+5(18%) HOMO→LUMO+25(10%) HOMO→LUMO+5(6%) HOMO→LUMO+23(5%) |
| 18 | 496.8 | 0.0045 | HOMO-1→LUMO+5(64%) HOMO→LUMO+24(9%) |
| 25 | 477 | 0.0099 | HOMO-1→LUMO+8(47%) HOMO-1→LUMO+10(16%) HOMO-1→LUMO+6(11%) |
| 27 | 473.3 | 0.0184 | HOMO-1→LUMO+7(21%) HOMO→LUMO+11(18%) HOMO-1→LUMO+24(13%) HOMO→LUMO+10(10%) HOMO-1→LUMO+8(7%) HOMO-2→LUMO+3(5%) |
| 28 | 473.2 | 0.0025 | HOMO→LUMO+11(48%) HOMO→LUMO+13(10%) HOMO-1→LUMO+7(9%) |
| 29 | 470.5 | 0.0134 | HOMO-1→LUMO+10(33%) HOMO-1→LUMO+24(17%) HOMO-1→LUMO+7(16%) HOMO-1→LUMO+25(6%) |
| 34 | 460.9 | 0.0039 | HOMO-1→LUMO+11(63%) HOMO-1→LUMO+13(16%) HOMO-1→LUMO+10(9%) |
| 37 | 455.3 | 0.0031 | HOMO-1→LUMO+13(45%) HOMO-1→LUMO+11(29%) |
| 50 | 430.4 | 0.0021 | HOMO-1→LUMO+16(85%) HOMO-1→LUMO+19(6%) |
| 59 | 420.2 | 0.0082 | HOMO-4→LUMO(54%) HOMO-4→LUMO+1(36%) |

| | | |
|---|---|---|
| 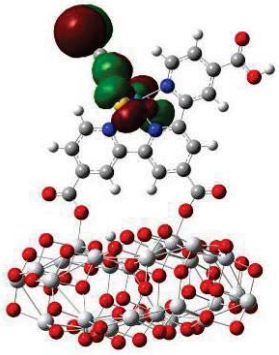 HOMO-3 (-6.17 eV) | 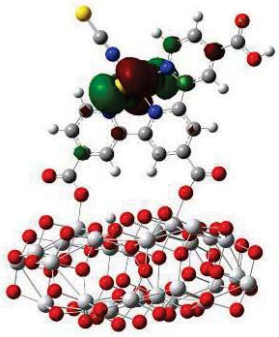 HOMO-1 (-5.46 eV) | 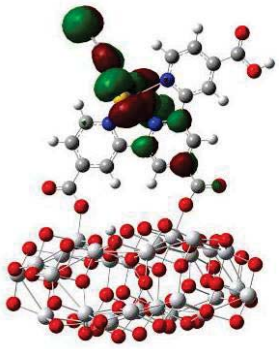 HOMO (-5.37 eV) |
| 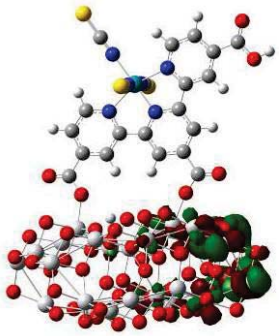 LUMO (-2.86 eV) | 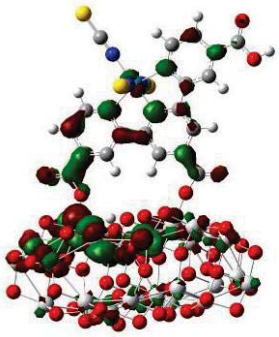 LUMO+1 (-2.60 eV) | 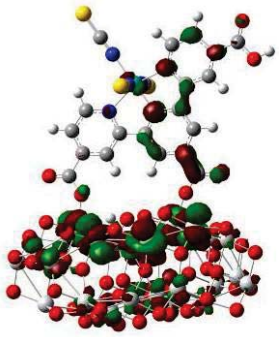 LUMO+2 (-2.53 eV) |
| 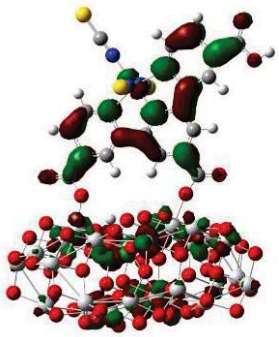 LUMO+3 (-2.48 eV) | 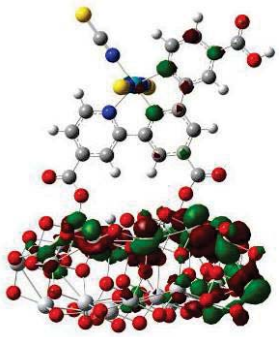 LUMO+4 (-2.45 eV) | 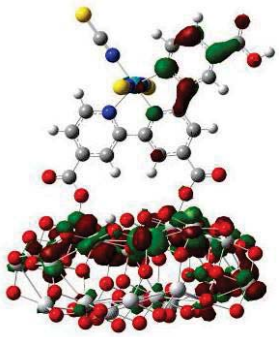 LUMO+6 (-2.38 eV) |
| 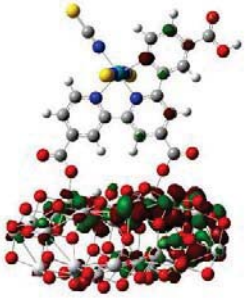 LUMO+9 (-2.26 eV) | 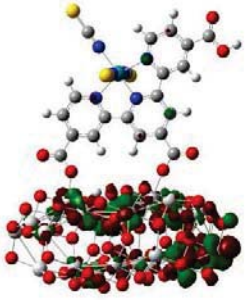 LUMO+10 (-2.24 eV) |  LUMO+11 (-2.22 eV) |

**Figure 1.7.1** Frontier molecular orbitals pertinent to the singlet optical transitions in selected states for N749-2H-P/$(TiO_2)_{28}$. The isovalue for the contours is 0.02.

| | | |
|---|---|---|
| 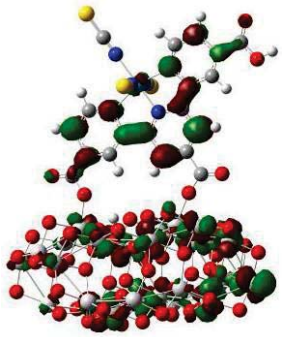 LUMO+12 (-2.18 eV) | 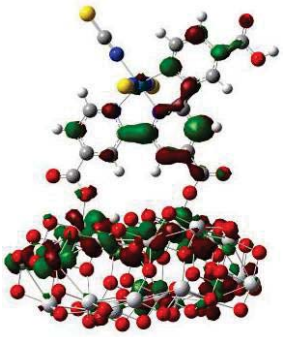 LUMO+13 (-2.17 eV) | 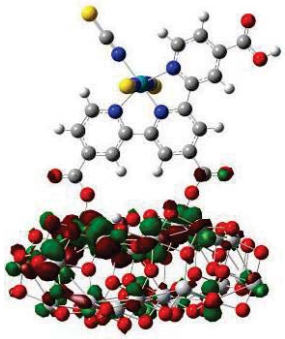 LUMO+14 (-2.13 eV) |
| 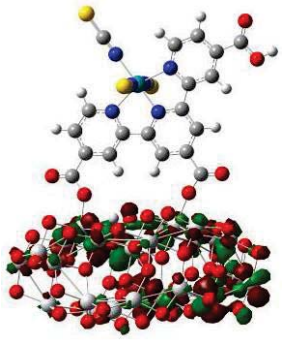 LUMO+15 (-2.11 eV) |  LUMO+16 (-2.09 eV) | 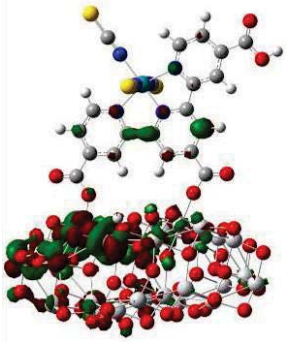 LUMO+17 (-2.06 eV) |
| 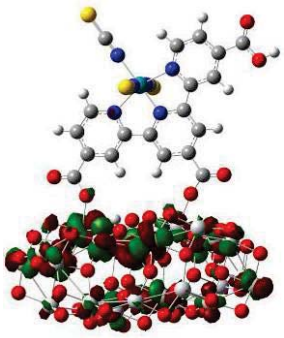 LUMO+18 (-2.02 eV) |  LUMO+30 (-1.77 eV) | 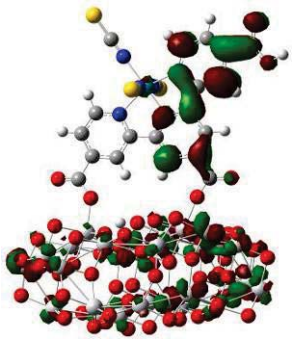 LUMO+32 (-1.75 eV) |

**Figure 1.7.2** Frontier molecular orbitals pertinent to the singlet optical transitions in selected states for N749-2H-P/$(TiO_2)_{28}$. The isovalue for the contours is 0.02.

**Table 1.4** The wavelengths, transition probabilities and charge transfer characters of the singlet optical transitions in selected states with oscillator strength > 0.003 for N749-2H-P/$(TiO_2)_{28}$.

| State | $\lambda_{cal}$ (nm) | *f* | Assignments |
|---|---|---|---|
| 1 | 656.1 | 0.0373 | HOMO-1→LUMO+3(32%) HOMO-1→LUMO+1(23%) HOMO-1→LUMO+2(13%) HOMO→LUMO+3(7%) |
| 2 | 618.3 | 0.0451 | HOMO→LUMO+3(29%) HOMO→LUMO+1(24%) HOMO→LUMO+2(11%) HOMO-1→LUMO+1(8%) HOMO-1→LUMO+3(6%) |
| 4 | 549.4 | 0.0458 | HOMO→LUMO+1(31%) HOMO→LUMO+12(16%) HOMO→LUMO+13(9%) HOMO→LUMO+6(7%) HOMO→LUMO+11(7%) |
| 6 | 525.5 | 0.0111 | HOMO→LUMO+1(28%) HOMO→LUMO+2(21%) HOMO→LUMO+12(8%) HOMO→LUMO+13(5%) |
| 9 | 515.5 | 0.0129 | HOMO→LUMO+2(45%) HOMO-1→LUMO+1(23%) HOMO→LUMO+3(8%) HOMO-1→LUMO+2(8%) HOMO-1→LUMO+3(5%) |
| 12 | 495 | 0.0152 | HOMO→LUMO+4(51%) HOMO-1→LUMO+3(10%) HOMO-1→LUMO+12(5%) |
| 29 | 444.2 | 0.0154 | HOMO→LUMO+12(25%) HOMO→LUMO+14(22%) HOMO→LUMO+11(20%) HOMO→LUMO+13(7%) HOMO-1→LUMO+9(5%) |
| 34 | 434.4 | 0.0144 | HOMO→LUMO+32(14%) HOMO→LUMO+14(14%) HOMO→LUMO+17(9%) HOMO→LUMO+12(7%) HOMO→LUMO+16(6%) HOMO→LUMO+30(6%) HOMO→LUMO+18(6%) |
| 35 | 432.1 | 0.0165 | HOMO-1→LUMO+10(24%) HOMO-1→LUMO+14(23%) HOMO-1→LUMO+13(16%) HOMO→LUMO+15(5%) |
| 44 | 421.2 | 0.036 | HOMO-3→LUMO+1(29%) HOMO-3→LUMO+3(27%) HOMO-3→LUMO+2(10%) |
| 45 | 419.6 | 0.0145 | HOMO-1→LUMO+15(16%) HOMO-1→LUMO+16(12%) HOMO-1→LUMO+17(9%) HOMO-1→LUMO+12(9%) HOMO-1→LUMO+14(8%) HOMO-3→LUMO+1(7%) |
| 46 | 419.1 | 0.0037 | HOMO-1→LUMO+15(63%) HOMO-1→LUMO+18(5%) |
| 49 | 415.7 | 0.0072 | HOMO-1→LUMO+17(65%) HOMO-1→LUMO+14(8%) |

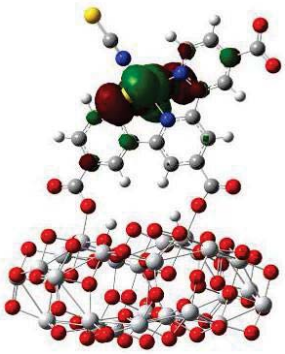
HOMO-1 (-5.35 eV)

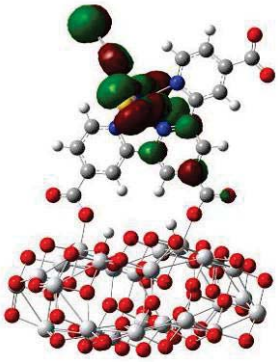
HOMO (-5.28 eV)

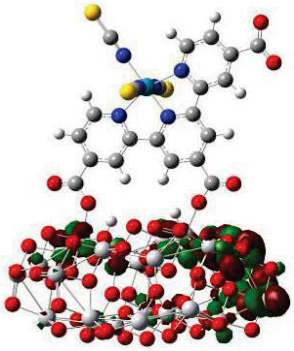
LUMO (-2.94 eV)

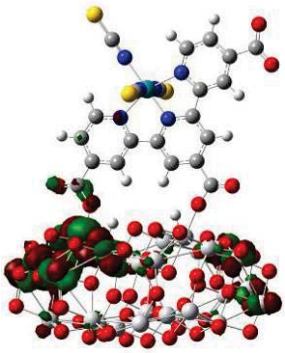
LUMO+1 (-2.86 eV)

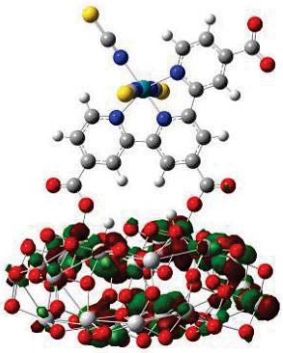
LUMO+2 (-2.70 eV)

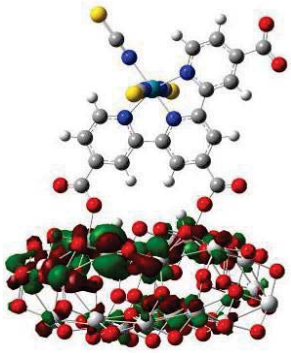
LUMO+3 (-2.62 eV)

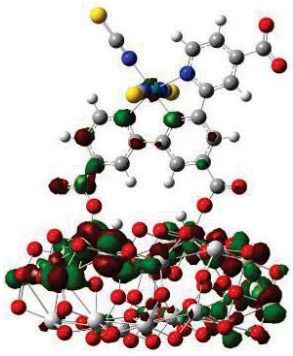
LUMO+4 (-2.61 eV)

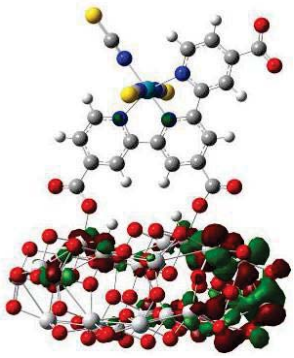
LUMO+5 (-2.58 eV)

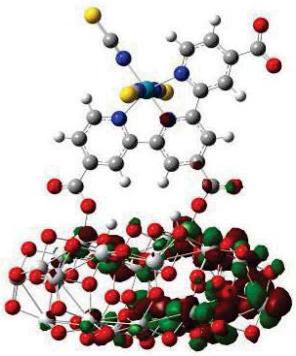
LUMO+6 (-2.53 eV)

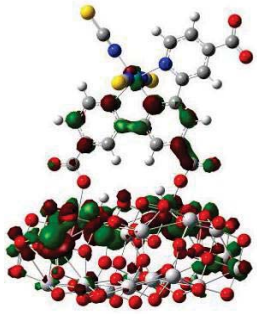
LUMO+7 (-2.49 eV)

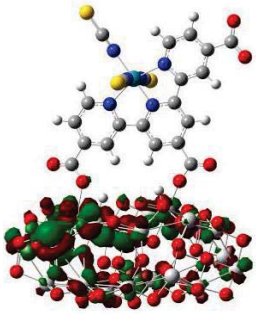
LUMO+8 (-2.47 eV)

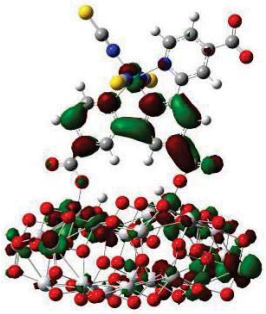
LUMO+9 (-2.42 eV)

**Figure 1.8.1** Frontier molecular orbitals pertinent to the singlet optical transitions in selected states for N749-2H-DP/$(TiO_2)_{28}$. The isovalue for the contours is 0.02.

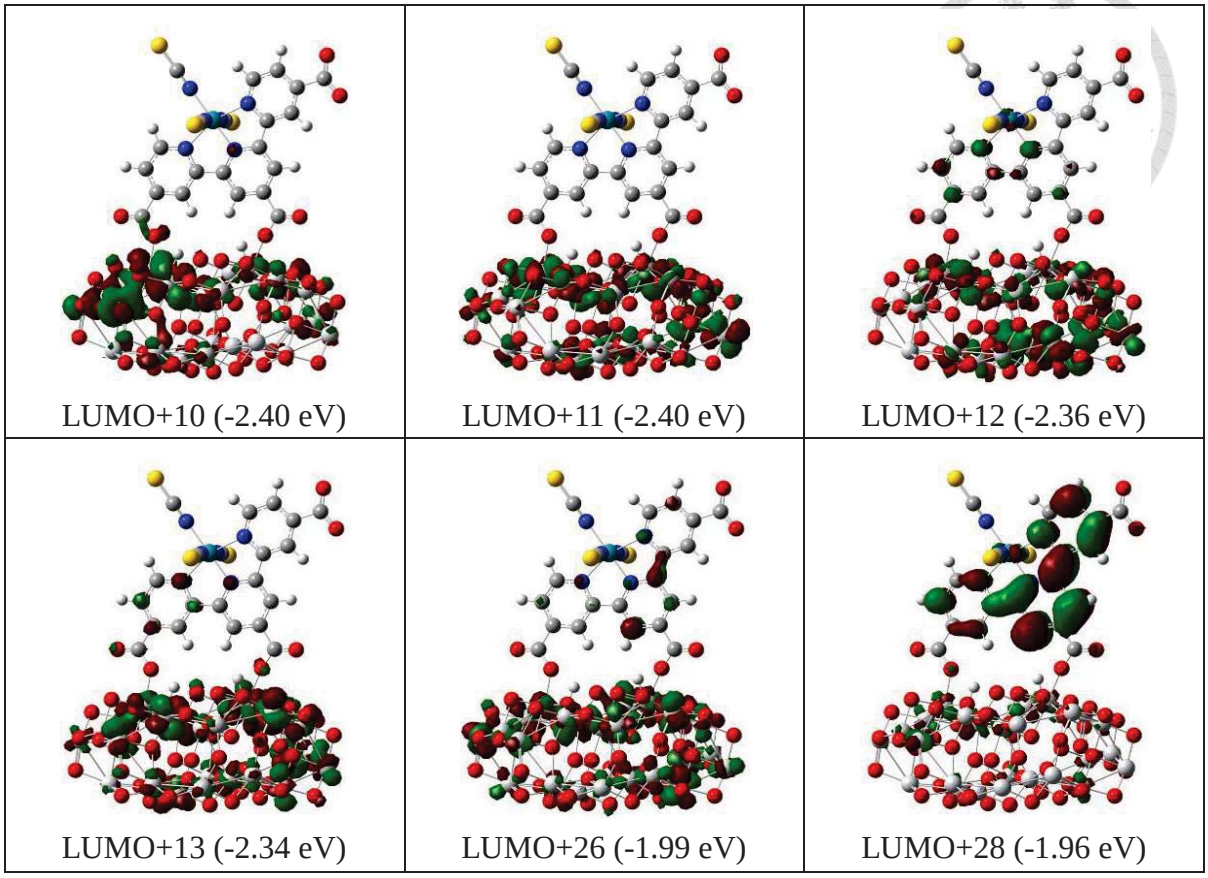


**Figure 1.8.2** Frontier molecular orbitals pertinent to the singlet optical transitions in selected states for N749-2H-DP/$(TiO_2)_{28}$. The isovalue for the contours is 0.02.

**Table 1.5** The wavelengths, transition probabilities and charge transfer characters of the singlet optical transitions in selected states with oscillator strength > 0.001 for N749-2H-DP/$(TiO_2)_{28}$.

| State | $\lambda_{cal}$ (nm) | *f* | Assignments |
|---|---|---|---|
| 1 | 659.6 | 0.0117 | HOMO-1→LUMO+9(22%) HOMO-1→LUMO+7(13%) HOMO-1→LUMO+4(11%) HOMO-1→LUMO+1(11%) HOMO-1→LUMO(5%) HOMO-1→LUMO+12(5%) |
| 2 | 615.7 | 0.0487 | HOMO→LUMO+1(41%) HOMO→LUMO(32%) HOMO→LUMO+7(20%) |
| 3 | 600.5 | 0.0016 | HOMO→LUMO(63%) HOMO→LUMO+1(34%) |
| 5 | 581.6 | 0.0016 | HOMO-1→LUMO(89%) |
| 6 | 579.8 | 0.0285 | HOMO-1→LUMO+1(25%) HOMO→LUMO+1(12%) HOMO→LUMO+9(10%) HOMO→LUMO+4(10%) HOMO→LUMO+7(6%) |
| 7 | 574.9 | 0.0269 | HOMO-1→LUMO+1(60%) HOMO→LUMO+1(8%) HOMO→LUMO+4(7%) HOMO→LUMO+9(6%) |
| 10 | 534.9 | 0.0041 | HOMO-1→LUMO+2(88%) |
| 16 | 511.7 | 0.0032 | HOMO→LUMO+6(31%) HOMO-1→LUMO+4(28%) HOMO-1→LUMO+3(8%) HOMO→LUMO+7(7%) HOMO→LUMO+28(6%) |
| 17 | 510.5 | 0.003 | HOMO→LUMO+6(41%) HOMO-1→LUMO+4(32%) HOMO-1→LUMO+3(6%) HOMO-1→LUMO+7(6%) |
| 19 | 503.3 | 0.0101 | HOMO→LUMO+8(33%) HOMO→LUMO+28(25%) HOMO→LUMO+6(11%) HOMO→LUMO+10(5%) |
| 20 | 500.4 | 0.0063 | HOMO→LUMO+8(28%) HOMO→LUMO+7(27%) HOMO→LUMO+28(21%) HOMO→LUMO+9(8%) |
| 21 | 499.2 | 0.0032 | HOMO→LUMO+8(28%) HOMO→LUMO+7(22%) HOMO→LUMO+9(21%) HOMO→LUMO+28(6%) |
| 28 | 480.4 | 0.0084 | HOMO→LUMO+13(35%) HOMO→LUMO+9(31%) HOMO→LUMO+12(15%) HOMO-1→LUMO+28(5%) |
| 29 | 478.3 | 0.0073 | HOMO-1→LUMO+10(71%) HOMO-1→LUMO+28(6%) HOMO-1→LUMO+8(6%) |
| 30 | 476 | 0.0287 | HOMO-1→LUMO+28(44%) HOMO-1→LUMO+10(18%) HOMO→LUMO+28(6%) HOMO-1→LUMO+26(5%) |
| 34 | 467.4 | 0.003 | HOMO-1→LUMO+13(38%) HOMO-1→LUMO+9(27%) |

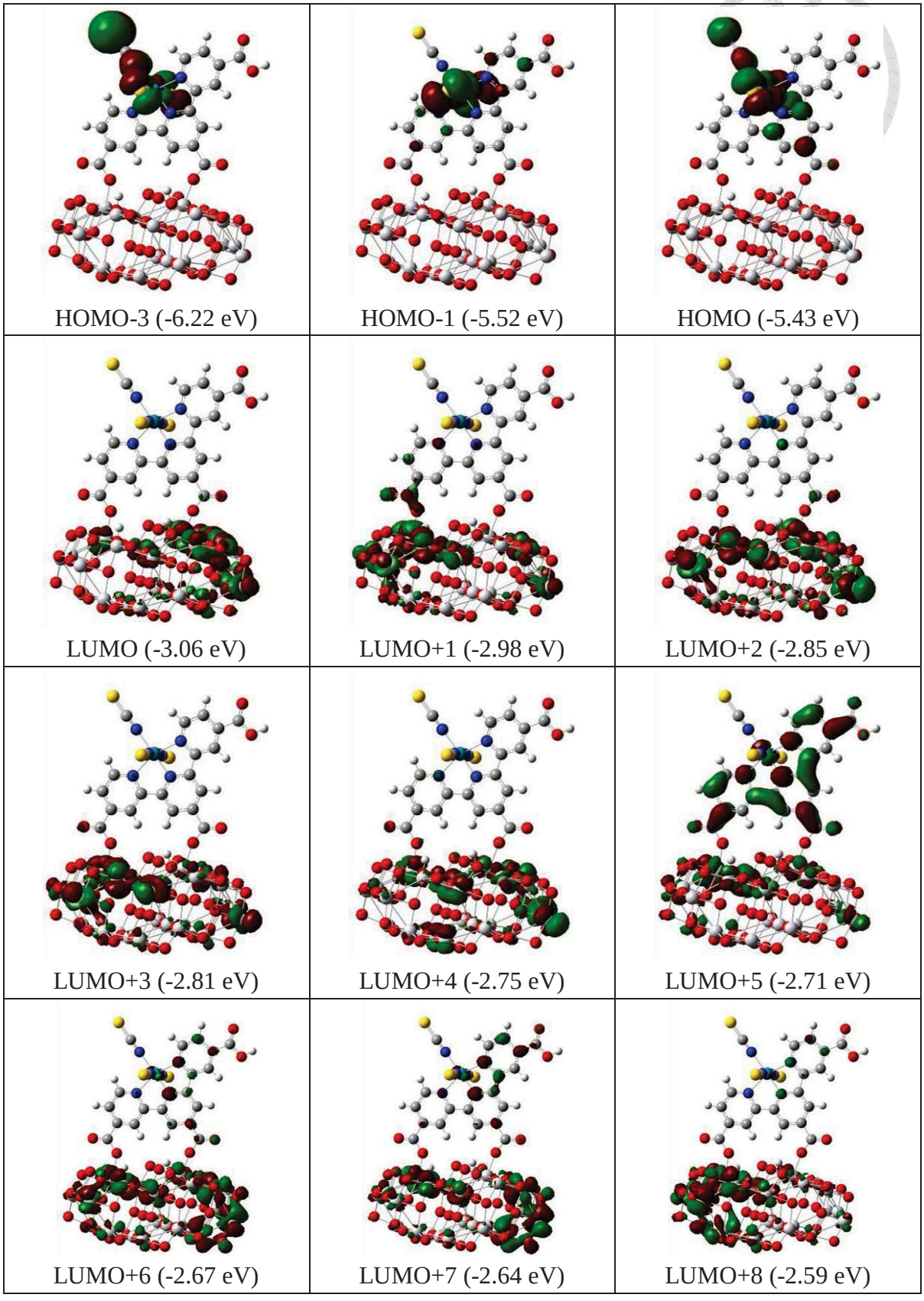


**Figure 1.9.1** Frontier molecular orbitals pertinent to the singlet optical transitions in selected states for N749-3H-P/$(TiO_2)_{28}$. The isovalue for the contours is 0.02.

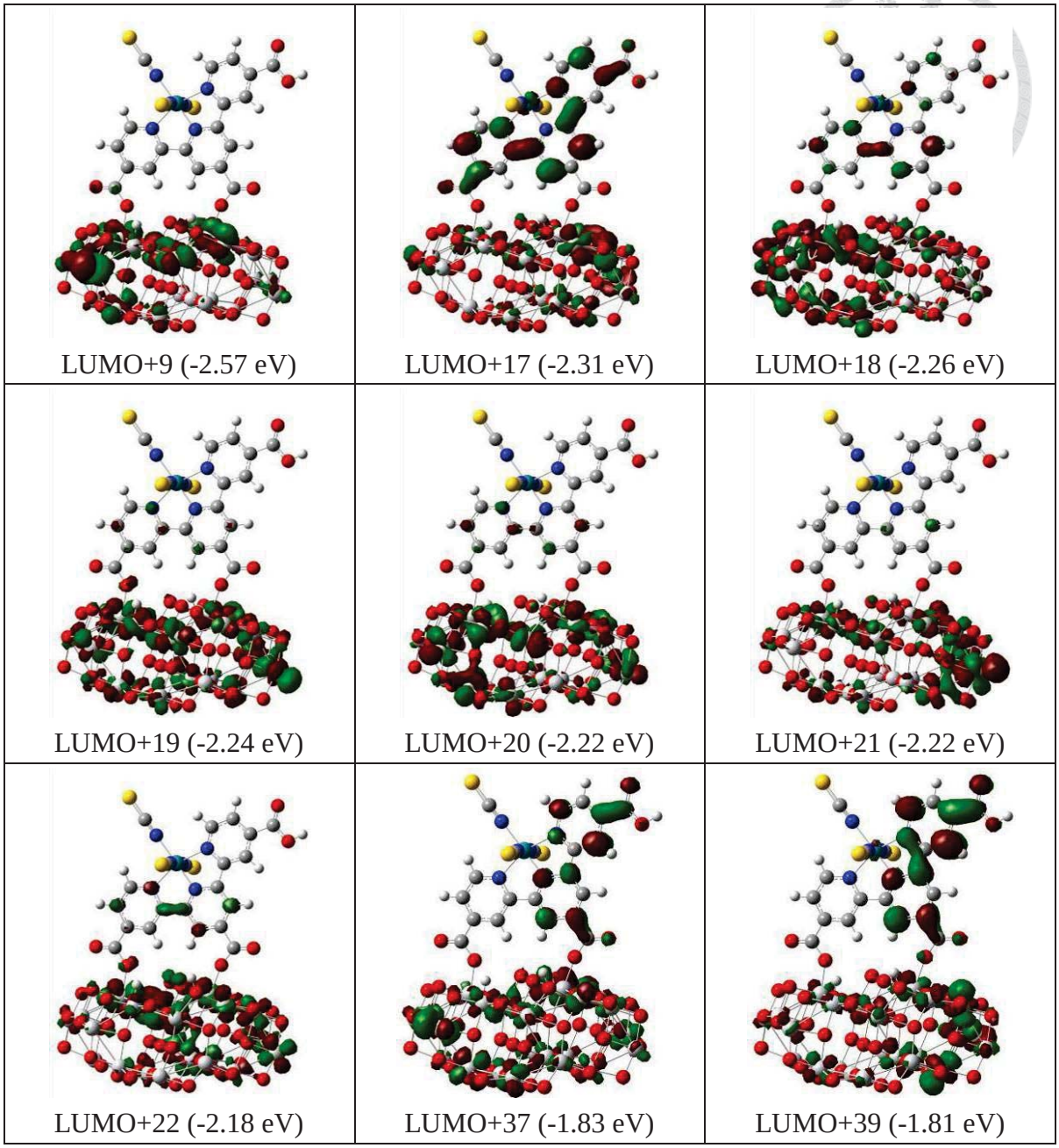


**Figure 1.9.2** Frontier molecular orbitals pertinent to the singlet optical transitions in selected states for N749-3H-P/$(TiO_2)_{28}$. The isovalue for the contours is 0.02.

**Table 1.6** The wavelengths, transition probabilities and charge transfer characters of the singlet optical transitions in selected states with oscillator strength > 0.004 for N749-3H-P/$(TiO_2)_{28}$.

| State | $\lambda_{cal}$ (nm) | *f* | Assignments |
|---|---|---|---|
| 1 | 671.5 | 0.0371 | HOMO-1→LUMO+5(38%) HOMO-1→LUMO(9%) HOMO-1→LUMO+1(9%) HOMO-1→LUMO+7(8%) HOMO-1→LUMO+6(7%) |
| 2 | 638.7 | 0.0463 | HOMO→LUMO(27%) HOMO→LUMO+5(24%) HOMO→LUMO+1(16%) |
| 5 | 589.3 | 0.0065 | HOMO→LUMO+1(65%) HOMO-1→LUMO(7%) HOMO→LUMO+5(7%) |
| 6 | 580.6 | 0.0047 | HOMO-1→LUMO(78%) HOMO-1→LUMO+1(7%) |
| 8 | 553.6 | 0.0095 | HOMO→LUMO+2(82%) |
| 9 | 547.4 | 0.0142 | HOMO→LUMO+3(50%) HOMO→LUMO+4(12%) HOMO→LUMO+17(10%) |
| 10 | 537.3 | 0.0207 | HOMO→LUMO+3(42%) HOMO→LUMO+17(12%) HOMO→LUMO+5(11%) |
| 14 | 522.6 | 0.0069 | HOMO-1→LUMO+3(77%) HOMO→LUMO+4(9%) |
| 17 | 508.1 | 0.0094 | HOMO-1→LUMO+4(58%) HOMO→LUMO+6(7%) HOMO-1→LUMO+6(7%) |
| 18 | 503.2 | 0.0093 | HOMO-1→LUMO+4(21%) HOMO→LUMO+6(21%) HOMO-1→LUMO+5(10%) HOMO-1→LUMO+17(9%) HOMO→LUMO+7(6%) |
| 21 | 495 | 0.0089 | HOMO→LUMO+8(25%) HOMO→LUMO+9(23%) HOMO-1→LUMO+6(19%) HOMO-1→LUMO+5(6%) HOMO-1→LUMO+17(6%) |
| 49 | 435.5 | 0.0148 | HOMO→LUMO+19(40%) HOMO→LUMO+20(20%) HOMO→LUMO+18(16%) |
| 52 | 429.9 | 0.0077 | HOMO→LUMO+20(64%) HOMO→LUMO+19(11%) |
| 53 | 428.4 | 0.0155 | HOMO→LUMO+19(19%) HOMO→LUMO+39(14%) HOMO→LUMO+22(14%) HOMO→LUMO+37(7%) HOMO→LUMO+18(6%) HOMO→LUMO+21(6%) |
| 56 | 425.9 | 0.0106 | HOMO-3→LUMO+1(45%) HOMO-3→LUMO(34%) |
| 59 | 422.9 | 0.0142 | HOMO-1→LUMO+19(43%) HOMO-1→LUMO+20(15%) HOMO-1→LUMO+18(7%) HOMO-1→LUMO+39(5%) |

| | | |
|---|---|---|
| 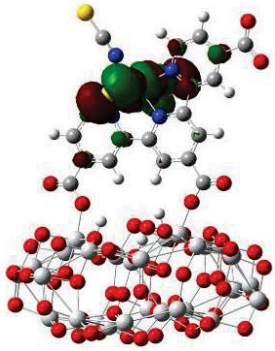 HOMO-1 (-5.40 eV) | 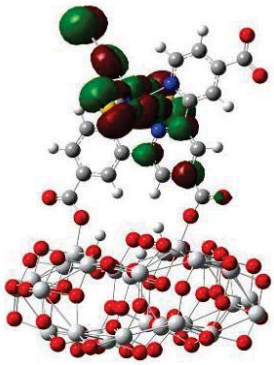 HOMO (-5.33 eV) | 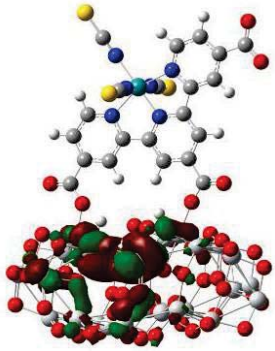 LUMO (-3.29 eV) |
| 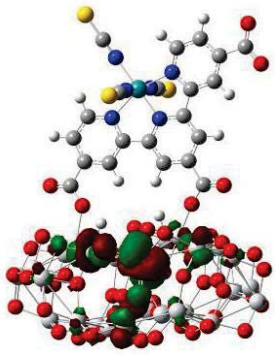 LUMO+1 (-3.14 eV) | 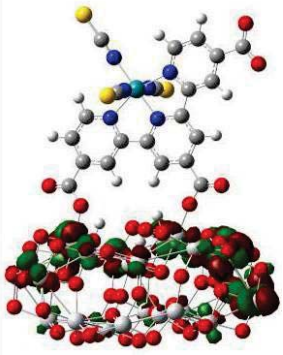 LUMO+2 (-3.07 eV) | 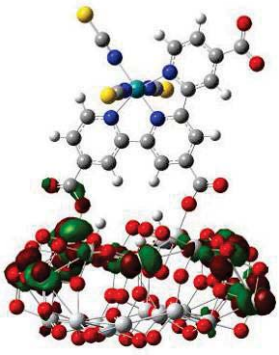 LUMO+3 (-3.01 eV) |
| 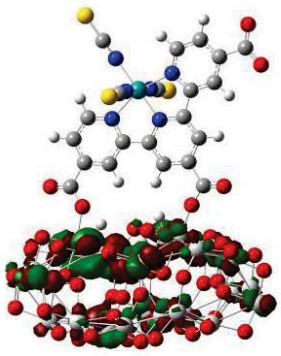 LUMO+4 (-2.88 eV) | 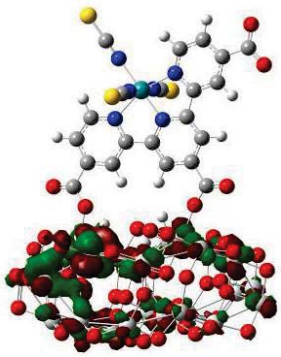 LUMO+5 (-2.87 eV) | 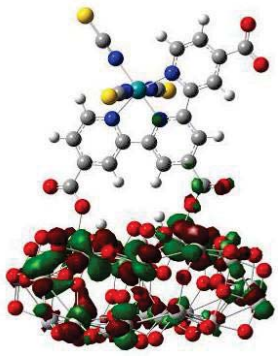 LUMO+6 (-2.80 eV) |
| 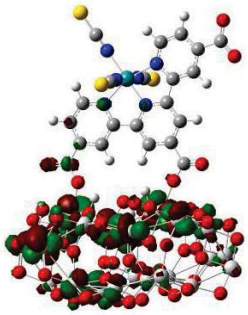 LUMO+7 (-2.78 eV) | 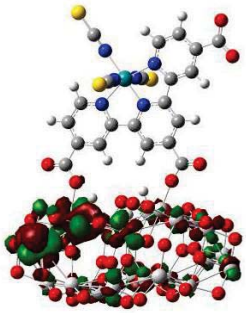 LUMO+9 (-2.73 eV) | 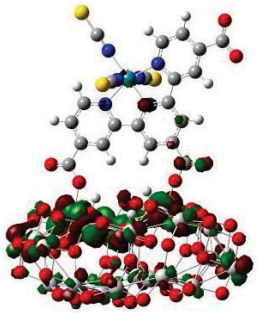 LUMO+11 (-2.67 eV) |

**Figure 1.10.1** Frontier molecular orbitals pertinent to the singlet optical transitions in selected states for N749-3H-DP/$(TiO_2)_{28}$. The isovalue for the contours is 0.02.

| | | |
|---|---|---|
| 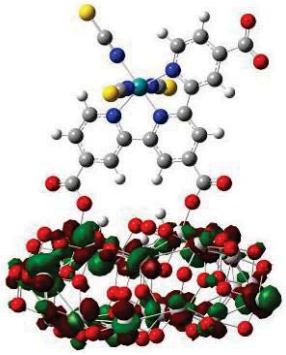 LUMO+12 (-2.58 eV) | 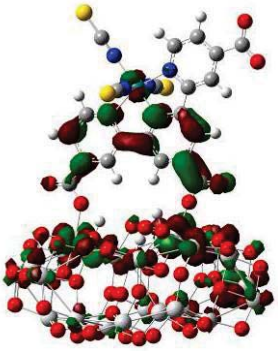 LUMO+13 (-2.58 eV) | 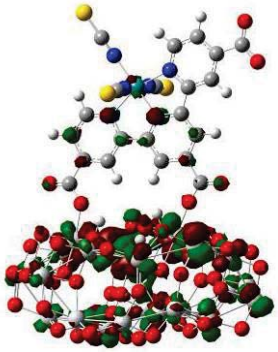 LUMO+14 (-2.56 eV) |
| 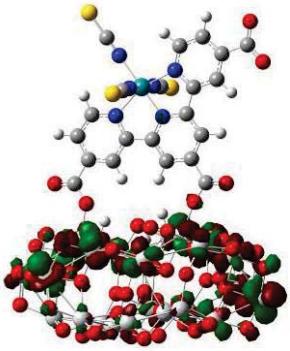 LUMO+15 (-2.54 eV) | 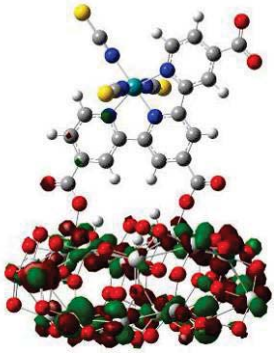 LUMO+17 (-2.46 eV) | 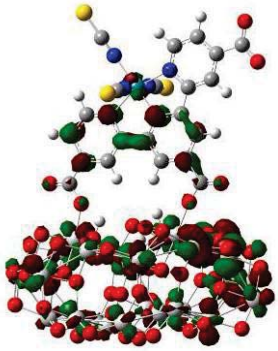 LUMO+18 (-2.45 eV) |
| 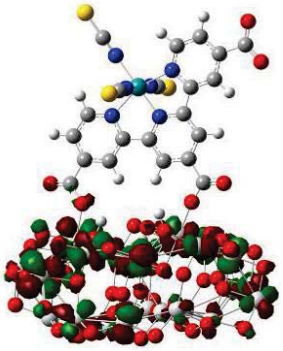 LUMO+19 (-2.44 eV) | 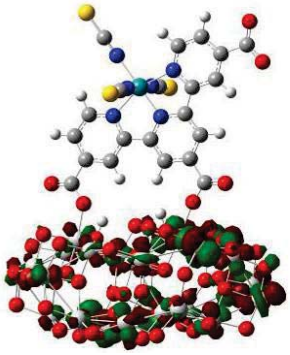 LUMO+20 (-2.40 eV) | 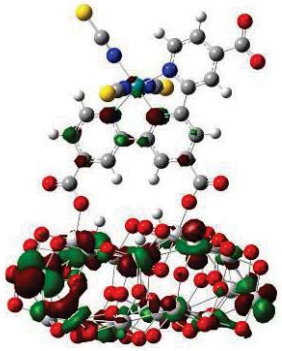 LUMO+21 (-2.38 eV) |
| 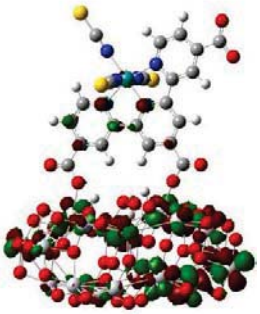 LUMO+24 (-2.32 eV) | 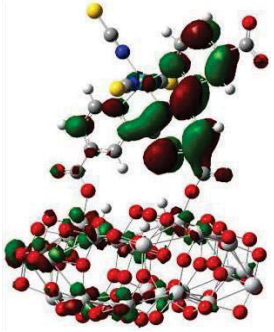 LUMO+35 (-2.04 eV) | 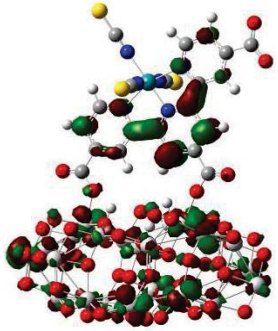 LUMO+37 (-2.01 eV) |

**Figure 1.10.2** Frontier molecular orbitals pertinent to the singlet optical transitions in selected states for N749-3H-DP/$(TiO_2)_{28}$. The isovalue for the contours is 0.02.

**Table 1.7** The wavelengths, transition probabilities and charge transfer characters of the singlet optical transitions in selected states with oscillator strength > 0.002 for N749-3H-DP/$(TiO_2)_{28}$.

| State | $\lambda_{cal}$ (nm) | *f* | Assignments |
|---|---|---|---|
| 1 | 731.7 | 0.0001 | HOMO→LUMO(100%) |
| 2 | 703.5 | 0.0002 | HOMO-1→LUMO(99%) |
| 3 | 672.6 | 0.0022 | HOMO→LUMO+1(84%) |
| 4 | 669.9 | 0.0079 | HOMO→LUMO+1(15%) HOMO-1→LUMO+13(14%) HOMO-1→LUMO+2(12%) HOMO-1→LUMO+3(7%) HOMO-1→LUMO+18(6%) |
| 5 | 649.1 | 0.0192 | HOMO→LUMO+2(54%) HOMO-1→LUMO+1(28%) HOMO→LUMO+3(10%) |
| 6 | 646.6 | 0.0082 | HOMO-1→LUMO+1(68%) HOMO→LUMO+2(19%) |
| 7 | 629.7 | 0.0047 | HOMO→LUMO+3(76%) HOMO→LUMO+2(19%) |
| 11 | 603.8 | 0.0023 | HOMO-1→LUMO+3(75%) |
| 12 | 598 | 0.0613 | HOMO→LUMO+4(20%) HOMO→LUMO+13(13%) HOMO→LUMO+6(12%) HOMO→LUMO+7(11%) HOMO-1→LUMO+3(8%) HOMO→LUMO+3(6%) |
| 13 | 589.1 | 0.0074 | HOMO→LUMO+5(75%) HOMO→LUMO+4(14%) |
| 17 | 567.3 | 0.0037 | HOMO-1→LUMO+4(50%) HOMO-1→LUMO+5(39%) |
| 19 | 555.2 | 0.006 | HOMO→LUMO+7(45%) HOMO→LUMO+11(15%) HOMO→LUMO+13(10%) HOMO→LUMO+6(6%) |
| 23 | 547 | 0.0033 | HOMO→LUMO+9(57%) HOMO-1→LUMO+6(28%) |
| 36 | 507.7 | 0.0091 | HOMO→LUMO+15(33%) HOMO→LUMO+35(19%) HOMO→LUMO+13(9%) HOMO→LUMO+14(7%) HOMO→LUMO+12(6%) |
| 37 | 503.1 | 0.0098 | HOMO→LUMO+15(47%) HOMO→LUMO+35(24%) HOMO→LUMO+37(7%) |
| 52 | 480.7 | 0.0296 | HOMO-1→LUMO+35(32%) HOMO→LUMO+18(16%) HOMO-1→LUMO+37(9%) |
| 54 | 476.7 | 0.007 | HOMO→LUMO+21(25%) HOMO→LUMO+20(24%) HOMO→LUMO+18(10%) HOMO-1→LUMO+35(8%) |
| 56 | 473.5 | 0.0039 | HOMO-1→LUMO+19(42%) HOMO-1→LUMO+17(14%) HOMO→LUMO+20(13%) HOMO→LUMO+21(7%) |

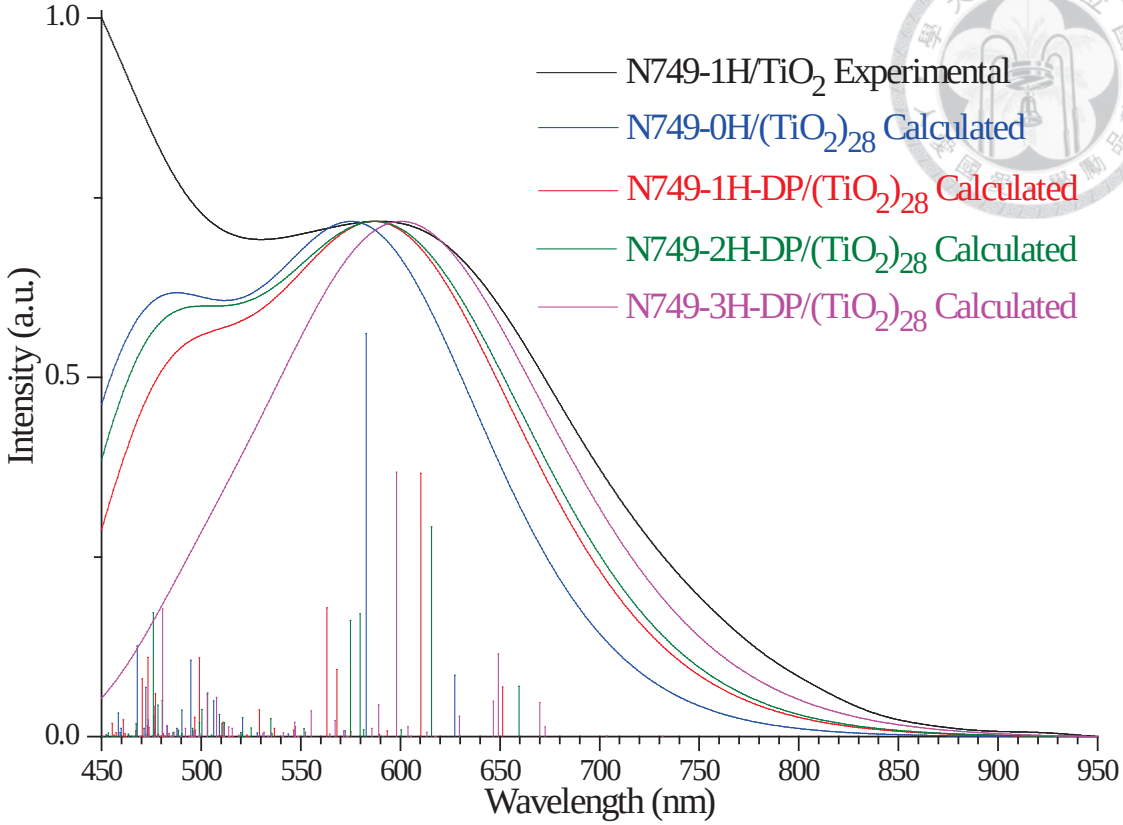


**Figure 1.11** The experimental N749-1H/$TiO_2$ and calculated absorption spectra of the four N749-DP/$(TiO_2)_{28}$ surface models in acetonitrile. The calculated spectra are obtained by a Gaussian convolution with $\sigma$ = 0.19 eV. Their intensities have been rescaled to match their absorption maxima over 560 nm. The blue, red, green, and pink vertical lines at the bottom of the graph represent the relative oscillator strengths.

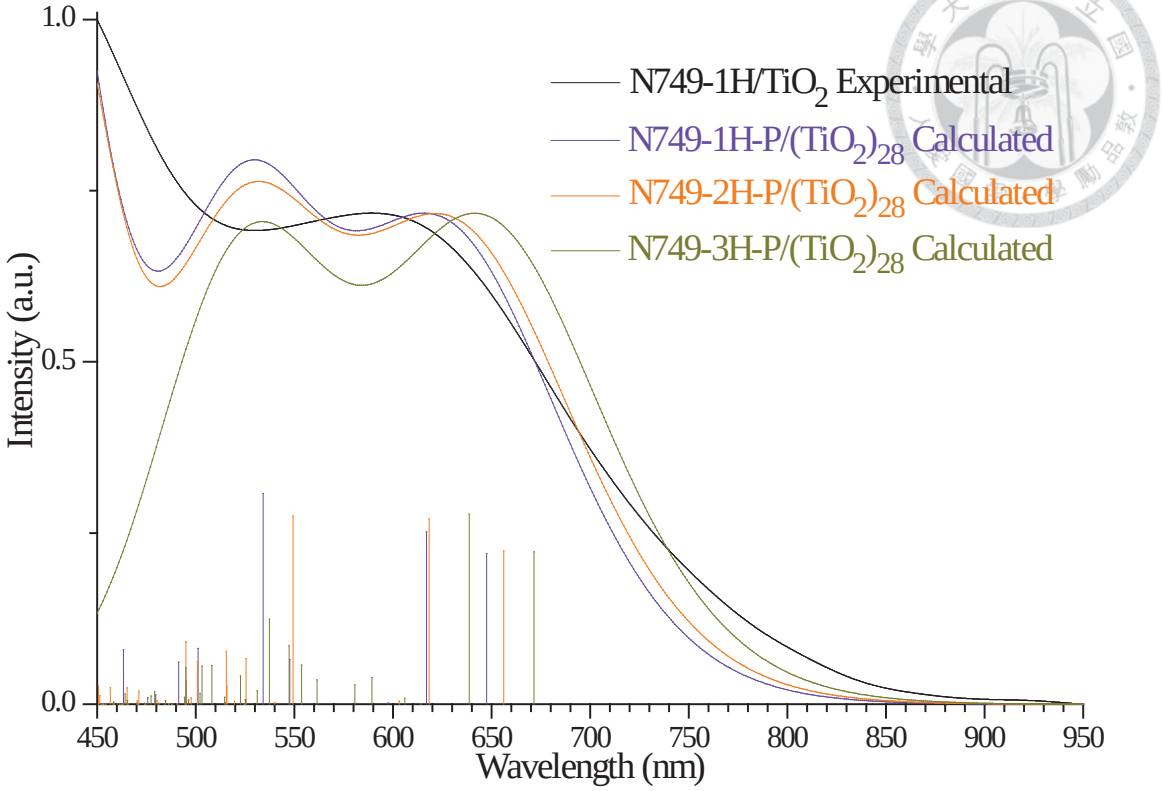


**Figure 1.12** The experimental N749-1H/$TiO_2$ and calculated absorption spectra of the three N749-P/$(TiO_2)_{28}$ surface models in acetonitrile. The calculated spectra are obtained by a Gaussian convolution with $\sigma$ = 0.19 eV. Their intensities have been rescaled to match their absorption maxima over 560 nm. The violet, orange, and dark yellow vertical lines at the bottom of the graph represent the relative oscillator strengths.

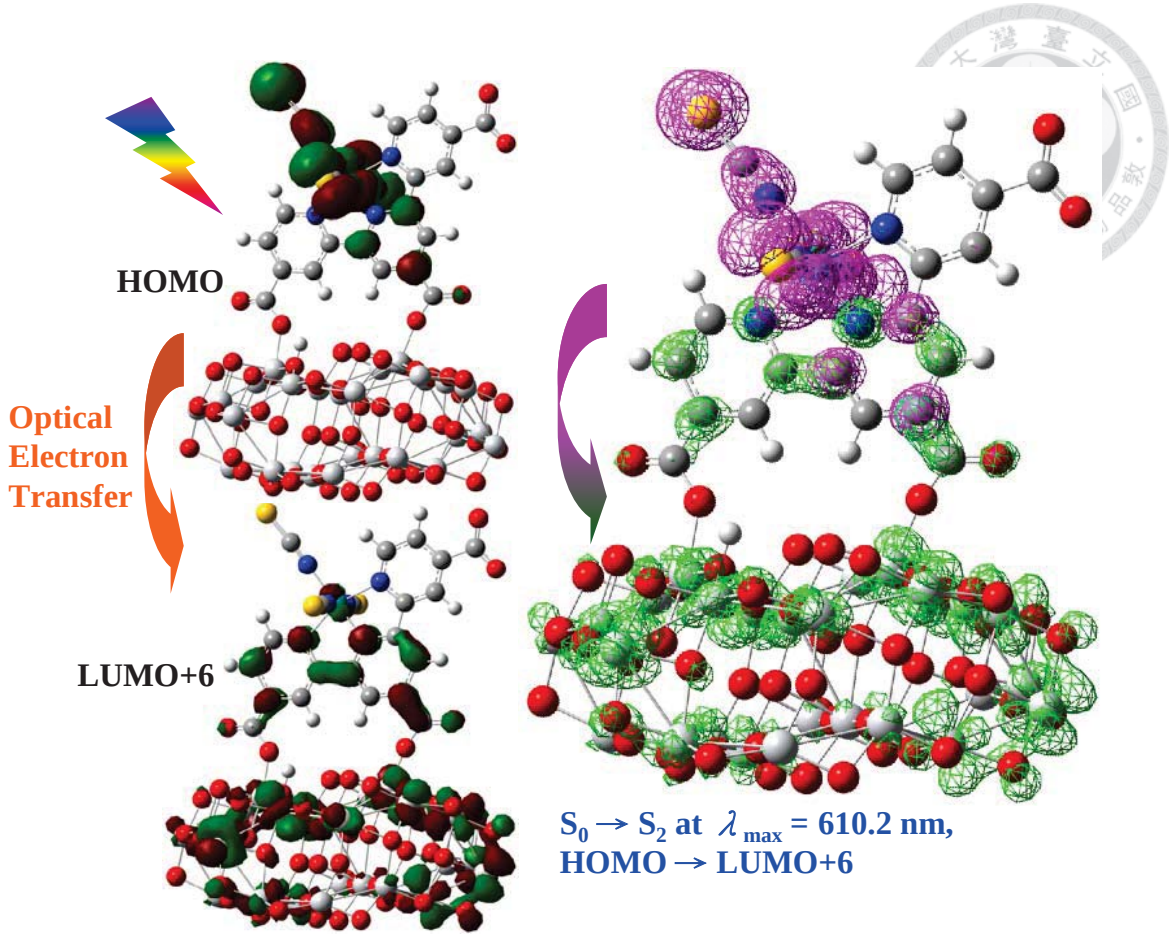


**Figure 1.13** Left: Frontier molecular orbitals of HOMO and LUMO+6 in N749-1H-DP/$(TiO_2)_{28}$ during optical absorption photoexcitation. Right: Charge density difference between the ground state $S_0$ and the excited state $S_2$. Pink mesh indicates decrease of charge density, while green mesh indicates the increase of charge density upon photoexcitation. The isovalue for the contours is 0.02.

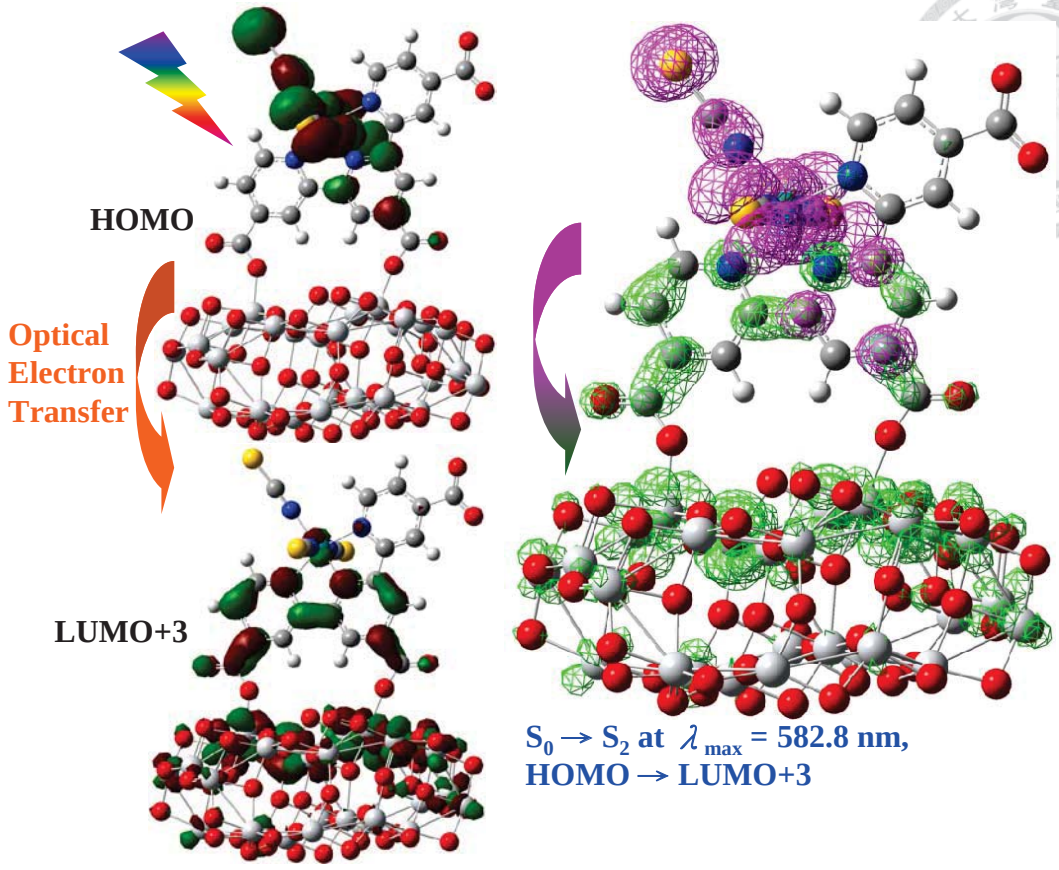


**Figure 1.14** Left**:** Frontier molecular orbitals of HOMO and LUMO+3 in N749-0H/$(TiO_2)_{28}$ during optical absorption photoexcitation. LUMO+3 is picked due to its largest delocalization of electron density in both N749-0H and $(TiO_2)_{28}$. Right: Charge density difference between the ground state $S_0$ and the excited state $S_2$. Pink mesh indicates decrease of charge density, while green mesh indicates the increase of charge density upon photoexcitation. The isovalue for the contours is 0.02.

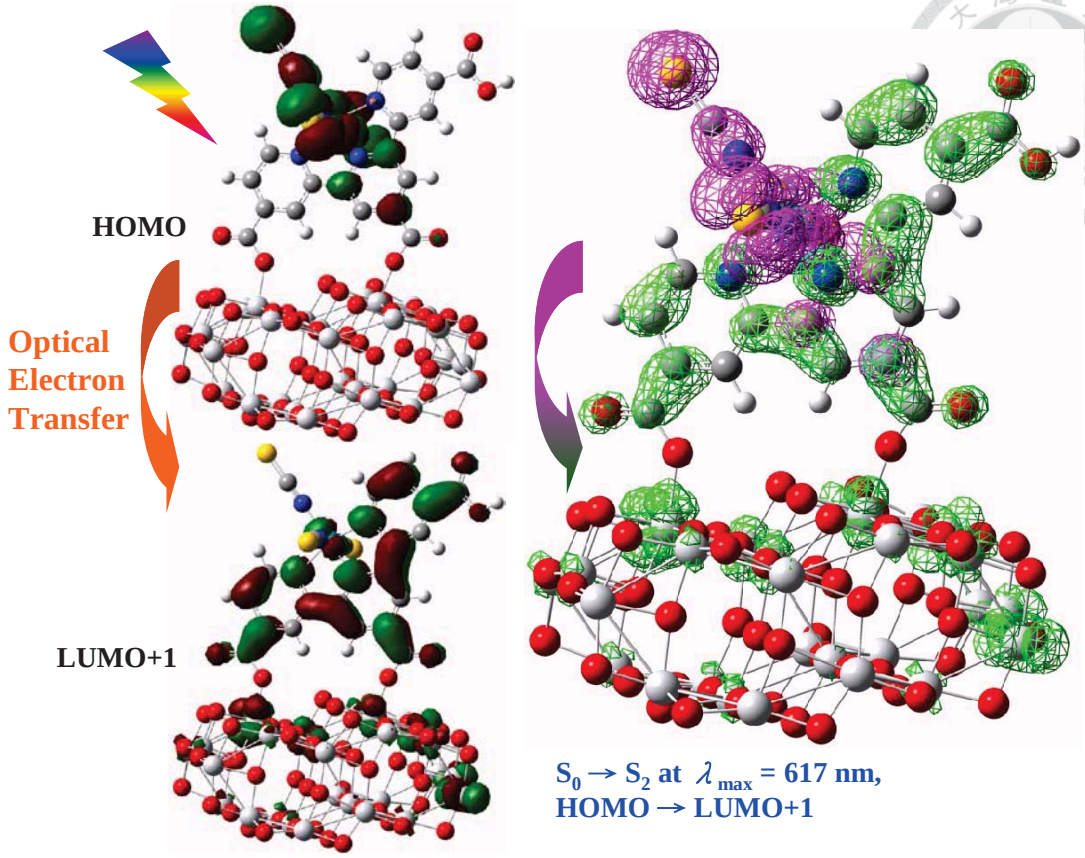


**Figure 1.15** Left**:** Frontier molecular orbitals of HOMO and LUMO+1 in N749-1H-P/$(TiO_2)_{28}$ during optical absorption photoexcitation. LUMO+1 is picked due to its largest delocalization of electron density in both N749-1H-P and $(TiO_2)_{28}$. Right: Charge density difference between the ground state $S_0$ and the excited state $S_2$. Pink mesh indicates decrease of charge density, while green mesh indicates the increase of charge density upon photoexcitation. The isovalue for the contours is 0.02.

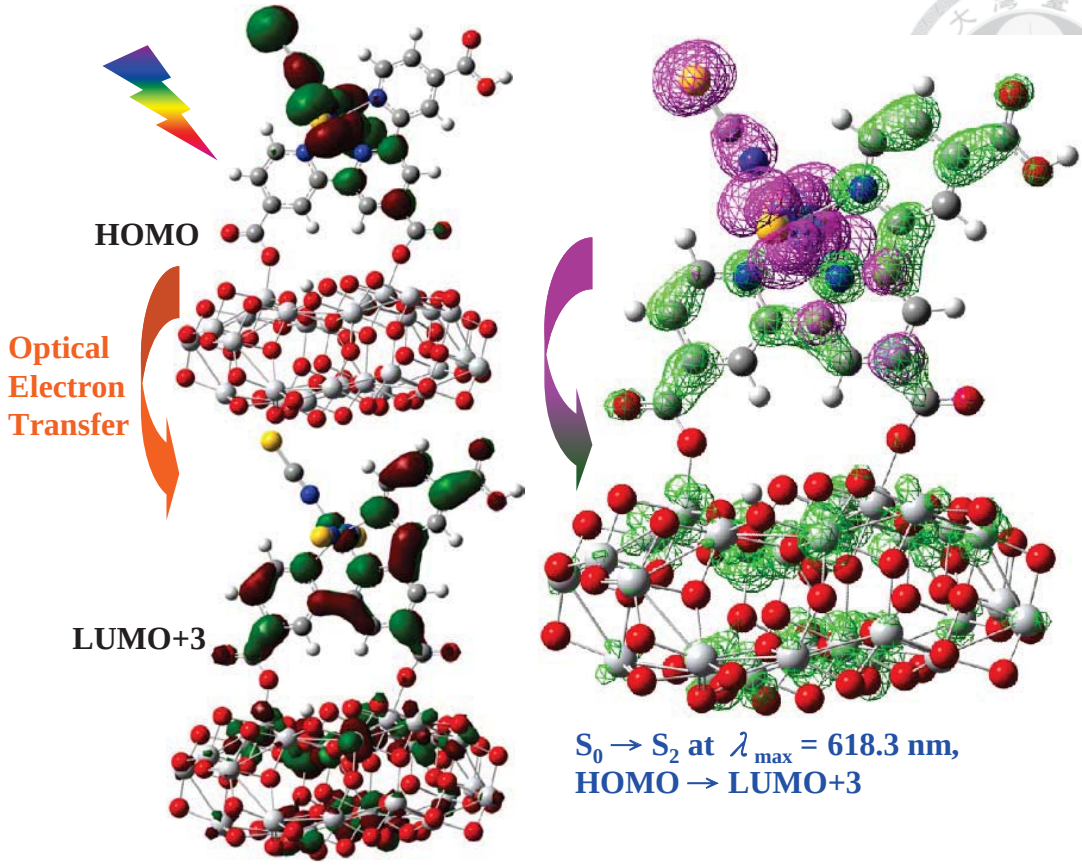


**Figure 1.16** Left**:** Frontier molecular orbitals of HOMO and LUMO+3 in N749-2H-P/$(TiO_2)_{28}$ during optical absorption photoexcitation. LUMO+3 is picked due to its largest delocalization of electron density in both N749-2H-P and $(TiO_2)_{28}$. Right: Charge density difference between the ground state $S_0$ and the excited state $S_2$. Pink mesh indicates decrease of charge density, while green mesh indicates the increase of charge density upon photoexcitation. The isovalue for the contours is 0.02.

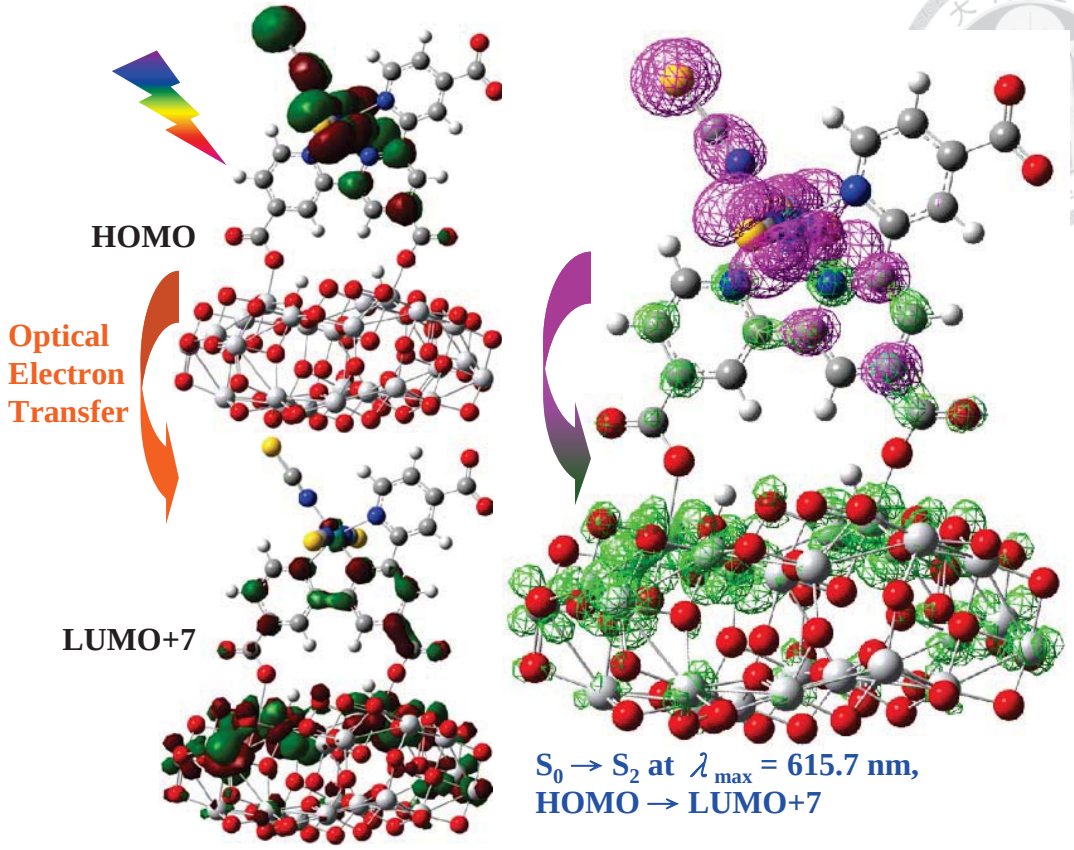


**Figure 1.17** Left**:** Frontier molecular orbitals of HOMO and LUMO+7 in N749-2H-DP/$(TiO_2)_{28}$ during optical absorption photoexcitation. LUMO+7 is picked due to its largest delocalization of electron density in both N749-2H-DP and $(TiO_2)_{28}$. Right: Charge density difference between the ground state $S_0$ and the excited state $S_2$. Pink mesh indicates decrease of charge density, while green mesh indicates the increase of charge density upon photoexcitation. The isovalue for the contours is 0.02.

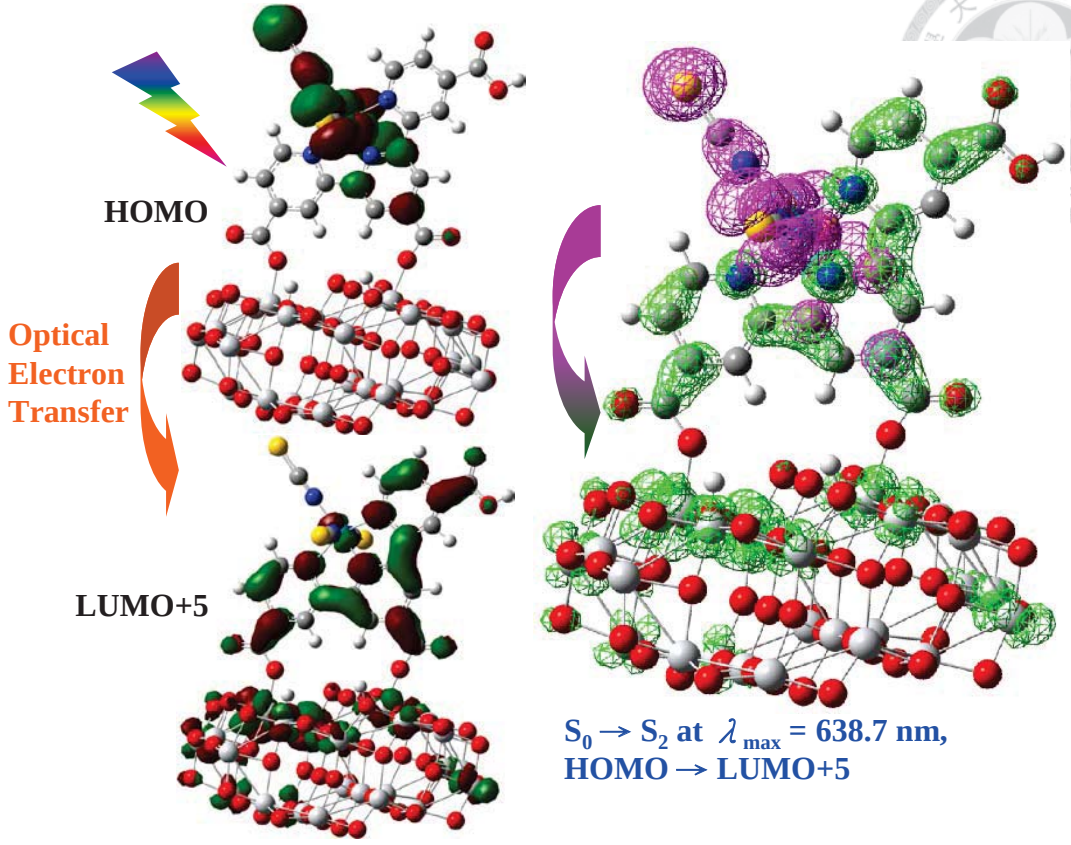


**Figure 1.18** Left**:** Frontier molecular orbitals of HOMO and LUMO+5 in N749-3H-P/$(TiO_2)_{28}$ during optical absorption photoexcitation. LUMO+5 is picked due to its largest delocalization of electron density in both N749-3H-P and $(TiO_2)_{28}$. Right: Charge density difference between the ground state $S_0$ and the excited state $S_2$. Pink mesh indicates decrease of charge density, while green mesh indicates the increase of charge density upon photoexcitation. The isovalue for the contours is 0.02.

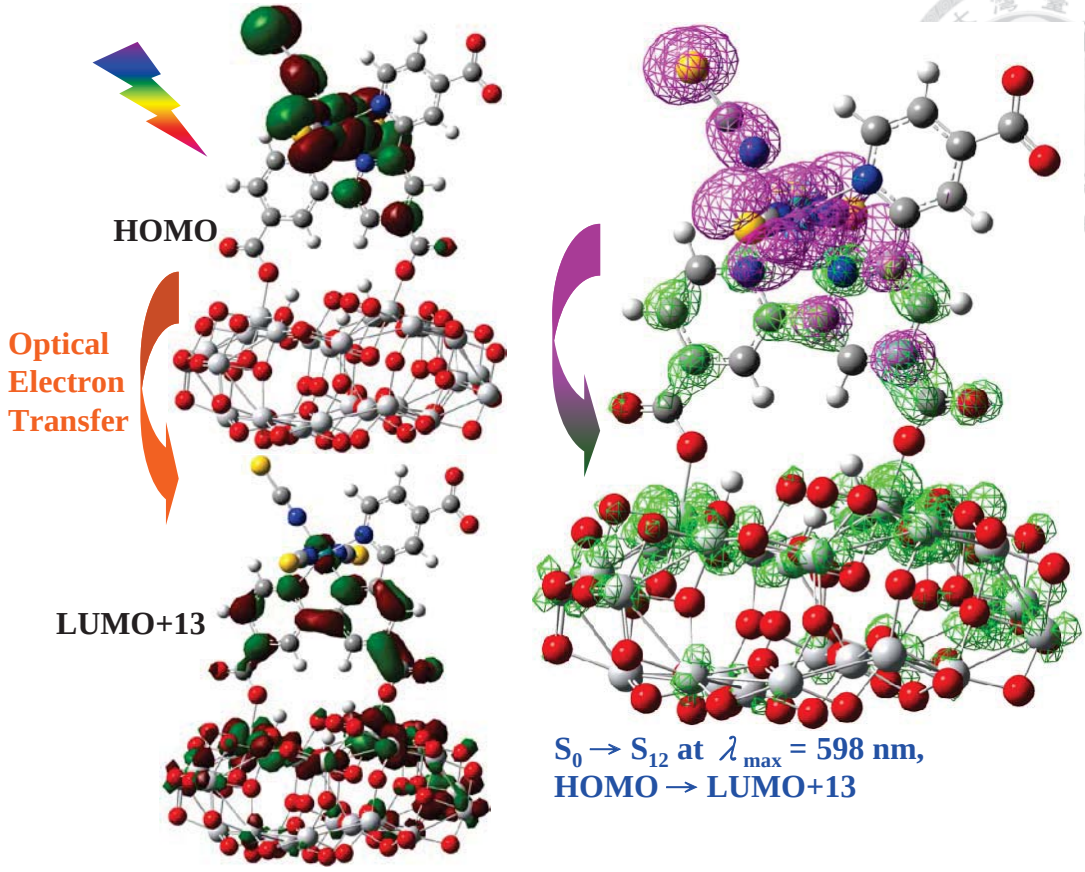


**Figure 1.19** Left**:** Frontier molecular orbitals of HOMO and LUMO+13 in N749-3H-DP/$(TiO_2)_{28}$ during optical absorption photoexcitation. LUMO+13 is picked due to its largest delocalization of electron density in both N749-3H-DP and $(TiO_2)_{28}$. Right: Charge density difference between the ground state $S_0$ and the excited state $S_{12}$. Pink mesh indicates decrease of charge density, while green mesh indicates the increase of charge density upon photoexcitation. The isovalue for the contours is 0.02.

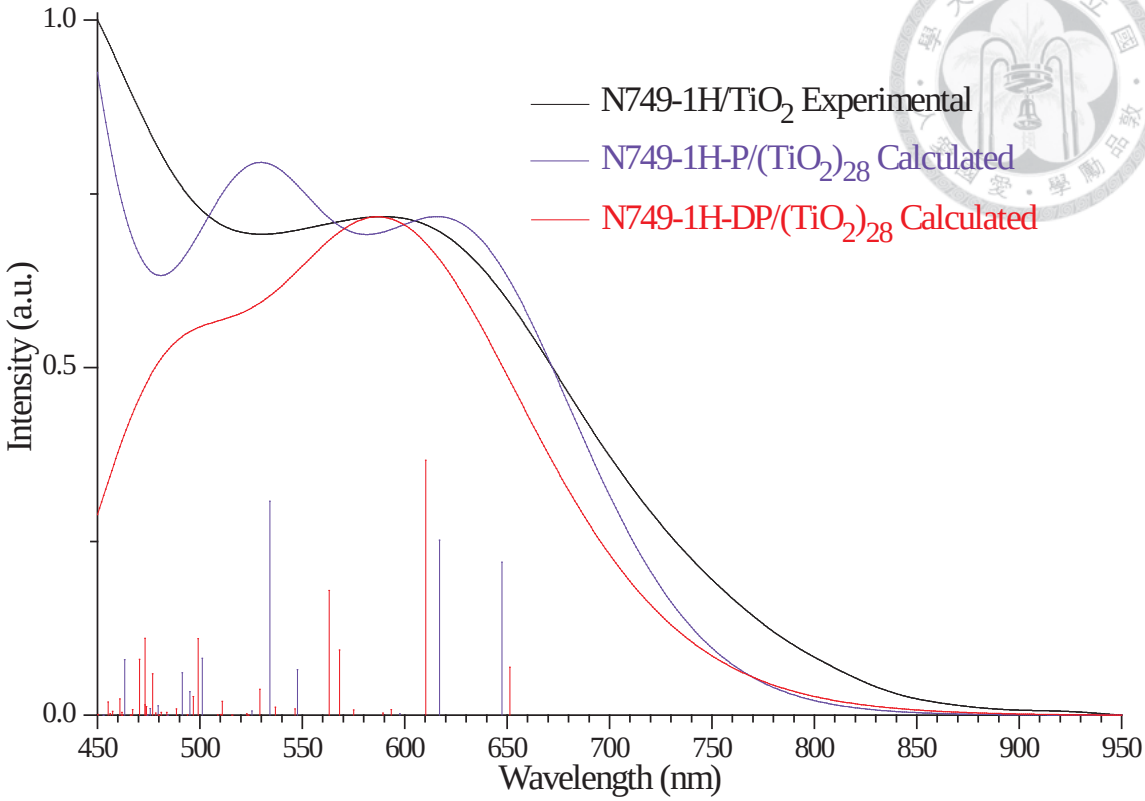


**Figure 1.20** The experimental N749-1H/$TiO_2$ and calculated absorption spectra of N749-1H-P/$(TiO_2)_{28}$ and N749-1H-DP/$(TiO_2)_{28}$ surface models in acetonitrile. The calculated spectra are obtained by a Gaussian convolution with $\sigma$ = 0.19 eV. Their intensities have been rescaled to match their absorption maxima over 560 nm. The violet and red vertical lines at the bottom of the graph represent the relative oscillator strengths.

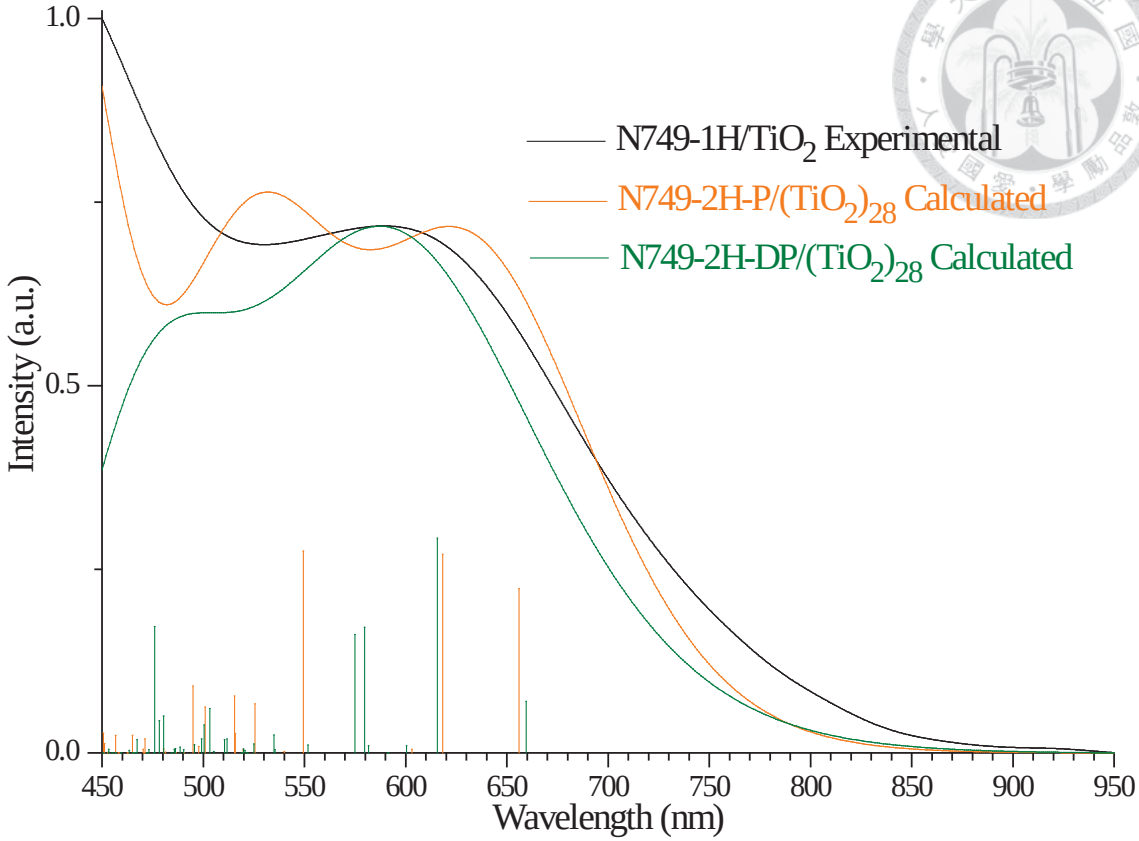


**Figure 1.21** The experimental N749-1H/$TiO_2$ and calculated absorption spectra of N749-2H-P/$(TiO_2)_{28}$ and N749-2H-DP/$(TiO_2)_{28}$ surface models in acetonitrile. The calculated spectra are obtained by a Gaussian convolution with $\sigma$ = 0.19 eV. Their intensities have been rescaled to match their absorption maxima over 560 nm. The orange and green vertical lines at the bottom of the graph represent the relative oscillator strengths.

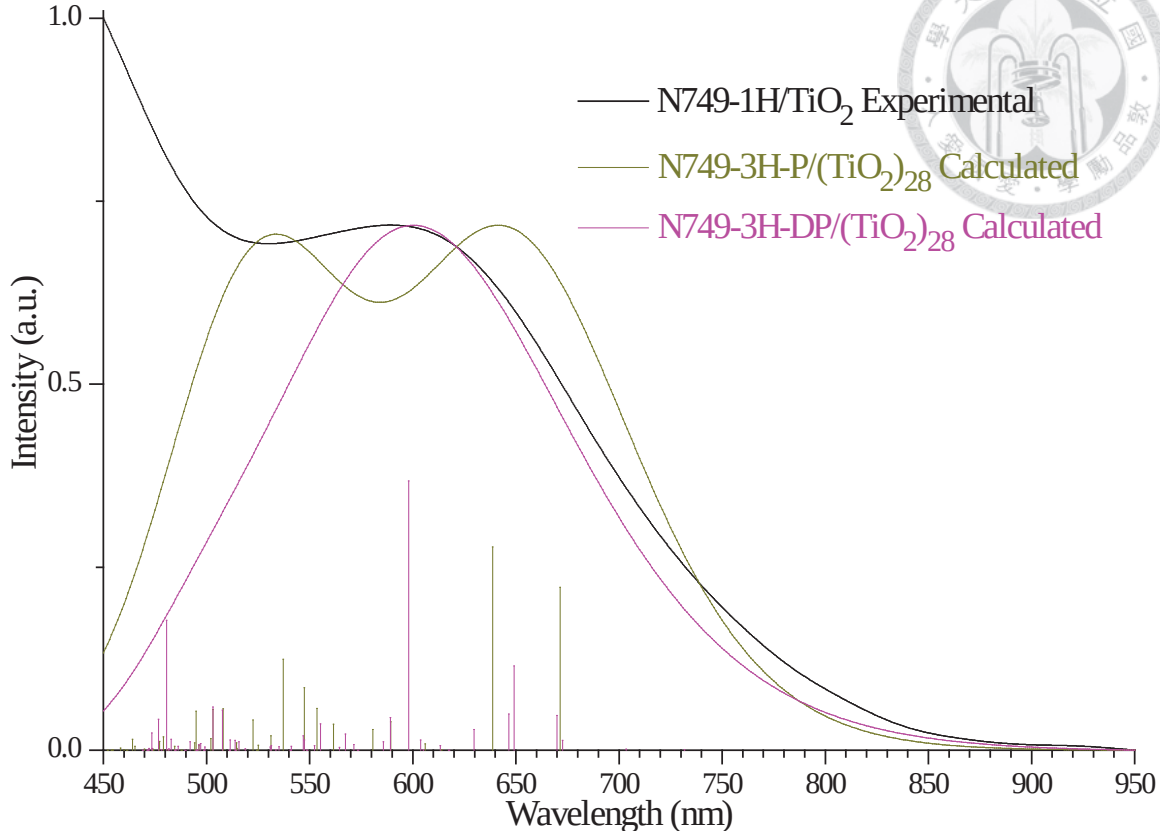


**Figure 1.22** The experimental N749-1H/$TiO_2$ and calculated absorption spectra of N749-3H-P/$(TiO_2)_{28}$ and N749-3H-DP/$(TiO_2)_{28}$ surface models in acetonitrile. The calculated spectra are obtained by a Gaussian convolution with $\sigma$ = 0.19 eV. Their intensities have been rescaled to match their absorption maxima over 560 nm. The dark yellow and pink vertical lines at the bottom of the graph represent the relative oscillator strengths.

## 1.6 References


1. O'Regan, B.; Grätzel, M. *Nature* **1991**, *353*, 737–740.

2. Grätzel, M. *Nature* **2001**, *414*, 338–344.

3. Hagfeldt, A.; Boschloo, G.; L, Sun.; Kloo, L.; Pettersson, H. *Chem. Rev*. **2010**, *110*, 6595–6663.

4. Boschloo, G.; Hagfeldt, A. *Acc. Chem. Res*. **2009**, *42*, 1819–1826.

5. Fantacci, S.; De Angelis, F. *Coord. Chem. Rev*. **2011**, *255*, 2704–2726.

6. Martsinovich, N.; Troisi, A. *Energy Environ. Sci*. **2011**, *4*, 4473–4495.

7. Labat, F. ; Bahers, T. L. ; Ciofini, I. ; Adamo, C. *Acc. Chem. Res*. **2012**, *45*, 1268–1277.

8. Yum, J. H.; Baranoff, E.; Wenger, S.; Nazeeruddin, M. K.; Grätzel, M. *Energy Environ. Sci*. **2011**, *4*, 842–857.

9. Persson, P; Lundqvist, M. J. *J. Phys. Chem. B* **2005**, *109*, 11918–11924.

10. Labat, F.; Ciofini, I.; Hratchian, H. P.; Frisch, M. J.; Raghavachari, K.; Adamo, C. *J. Phys. Chem. C* **2011**, *115*, 4297–4306.

11. De Angelis, F.; Tilocca, A.; Selloni, A. *J. Am. Chem. Soc*. **2004**, *126*, 15024–15025.

12. De Angelis, F.; Fantacci, S.; Selloni, A.; Nazeeruddin, M. K.; Grätzel, M. *J. Am. Chem. Soc*. **2007**, *129*, 14156–14157.

13. De Angelis, F.; Fantacci, S.; Selloni, A.; Nazeeruddin, M. K.; Grätzel, M. *J. Phys.*

*Chem. C* **2010**, *114*, 6054–6061.

14. De Angelis, F.; Fantacci, S.; Mosconi, E.; Nazeeruddin, M. K.; Grätzel, M. *J. Phys. Chem. C* **2011**, *115*, 8825–8831.

15. Sodeyama, K.; Sumita, M.; O'Rourke, C.; Terranova, U.; Islam, A.; Han, L.; Bowler, D. R.; Tateyama, Y. *J. Phys. Chem. Lett.* **2012**, *3*, 472–477.

16. Nazeeruddin, M. K.; Péchy, P.; Grätzel, M. *Chem. Commun*. **1997**, 1705–1706.

17. Nazeeruddin, M. K.; Péchy, P.; Renouard, T.; Zakeeruddin, S. M.; Humphry-Baker, R.; Comte, P.; Liska, P.; Cevey, L.; Costa, E.; Shklover, V.; Spiccia, L.; Deacon, G. B.; Bignozzi, C. A.; Grätzel, M. *J. Am. Chem. Soc*. **2001**, *123*, 1613–1624.

18. Chiba, Y.; Islam, A.; Watanabe, Y.; Komiya, R.; Koide, N.; Han, L. *Jpn. J. Appl. Phys.* **2006**, *45*, L638.

19. Zubavichus, Y. V.; Slovokhotov, Y. L.; Nazeeruddin, M. K.; Zakeeruddin, S. M.; Grätzel, M.; Shklover, V. *Chem. Mater*. **2002**, *14*, 3556–3563.

20. Bauer, C.; Boschloo, G.; Mukhtar, E.; Hagfeldt, A. *J. Phys. Chem. B* **2002**, *106*, 12693–12704.

21. Li, M.-X.; Zhou, X.; Xia, B.-H.; Zhang, H.-X.; Pan, Q.-J.; Liu, T.; Fu, H.-G.; Sun, C.-C. *Inorg. Chem*. **2008**, *47*, 2312–2324.

22. Nazeeruddin, M. K.; Humphry-Baker, R.; Liska, P.; Grätzel, M. *J. Phys. Chem. B* **2003**, *107*, 8981–8987.

23. Yang, S. H.; Wu, K. L.; Chi, Y.; Cheng, Y. M.; Chou, P. T. *Angew*. *Chem*., *Int*. *Ed*. **2011**, *50*, 8270–8274.

24. Persson, P.; Bergström, R.; Ojamäe, L.; Lunell, S. *Adv*. *Quantum Chem*. **2002**, *41*, 203–263.

25. Hirva, P.; Haukka, M. *Langmuir* **2010**, *26*, 17075–17081.

26. Robson, K. C. D.; Sporinova, B.; Koivisto, B. D.; Baumgartner, T.; Yella, A.; Nazeeruddin, K. M.; Grätzel, M.; Berlinguette, C. P. *Inorg*. *Chem*. **2011**, *50*, 5494–5508.

27. Vougioukalakis, G. C.; Stergiopoulos, T.; Kantonis, G.; Kontos, A. G.; Papadopoulos, K.; Stublla, A.; Potvin, P. G.; Falaras, P. *J*. *Photochem*. *Photobiol*. *A*: *Chem*. **2010**, *214*, 22–32.

28. Chen, B. S.; Chen, K.; Hong, Y. H.; Liu, W. H.; Li, T. H.; Lai, C. H.; Chou, P. T.; Chi, Y.; Lee, G. H. *Chem*. *Commun*., **2009**, 5844–5846.

29. Chen, K.; Hong, Y. H.; Chi, Y.; Liu, W. H.; Chen, B. S., Chou, P. T. *J*. *Mater*. *Chem*. **2009**, *19*, 5329–5335.

30. Chou, C. C.; Wu, K. L; Chi, Y.; Hu, W. P.; Yu, S. J.; Lee, G.. H.; Lin, C. L.; Chou, P. T. *Angew*. *Chem*., *Int*. *Ed*. **2011**, *50*, 2054–2058.

31. Wu, K. L.; Li, C. H.; Chi, Y.; Clifford, J. N.; Cabau, L.; Palomares, E.; Cheng, Y. M.; Pan, H. A.; Chou, P. T. *J*. *Am*. *Chem*. *Soc*. **2012**, *134*, 7488–7496.

32. Wu, K. L.; Ho, S. T.; Chou, C. C.; Chang, Y. C.; Pan, H, A.; Chi, Y.; Chou, P. T; *Angew*. *Chem*., *Int*. *Ed*. **2012**, *51*, 5642–5646.

33. Persson, P.; Gebhardt, J. C. M.; Lunell, S.; *J*. *Phys*. *Chem*. *B* **2003**, *107*, 3336–3339.

34. Lundqvist, M. J.; Nilsing, M.; Persson, P.; Lunell, S. *Int*. *J*. *Quantum Chem*. **2006**, *106*, 3214–3234.

35. Frisch, M. J.; Trucks, G. W.; Schlegel, H. B.; Scuseria, G. E.; Robb, M. A.; Cheeseman, J. R.; Scalmani, G.; Barone, V.; Mennucci, B.; Petersson, G. A.; Nakatsuji, H.; Caricato, M.; Li, X.; Hratchian, H. P.; Izmaylov, A. F.; Bloino, J.; Zheng, G.; Sonnenberg, J. L.; Hada, M.; Ehara, M.; Toyota, K.; Fukuda, R.; Hasegawa, J.; Ishida, M.; Nakajima, T.; Honda, Y.; Kitao, O.; Nakai, H.; Vreven, T.; Montgomery, J. A., Jr.; Peralta, J. E.; Ogliaro, F.; Bearpark, M.; Heyd, J. J.; Brothers, E.; Kudin, K. N.; Staroverov, V. N.; Kobayashi, R.; Normand, J.; Raghavachari, K.; Rendell, A.; Burant, J. C.; Iyengar, S. S.; Tomasi, J.; Cossi, M.; Rega, N.; Millam, N. J.; Klene, M.; Knox, J. E.; Cross, J. B.; Bakken, V.; Adamo, C.; Jaramillo, J.; Gomperts, R.; Stratmann, R. E.; Yazyev, O.; Austin, A. J.; Cammi, R.; Pomelli, C.; Ochterski, J. W.; Martin, R. L.; Morokuma, K.; Zakrzewski, V. G.; Voth, G. A.; Salvador, P.; Dannenberg, J. J.; Dapprich, S.; Daniels, A. D.; Farkas, ö.; Foresman, J. B.; Ortiz, J. V.; Cioslowski, J.; Fox, D. J. *Gaussian 09*, Revision A.02; Gaussian, Inc.: Wallingford, CT, 2009.

36. Perdew, J. P.; Burke, K.; Ernzerhof, M. *Phys*. *Re*v. *Lett*. **1996**, *77*, 3865–3868.

37. Vlček Jr., A.; Záliš, S. *Coord*. *Chem*. *Rev*. **2007**, *251*, 258–287.

38. Kalyanasundaram, K.; Grätzel, M. *Coord*. *Chem*. *Rev*. **1998**, *177*, 347–414.

39. Koops, S. E.; O'Regan, B. C.; Barnes, P. R. F.; Durrant, J. R. *J*. *Am*. *Chem*. *Soc*. **2009**, *131*, 4808–4818.

## Chapter II: Tridentate Terpyridine Os(II)– and Ru(II)–Based Dyes Anchoring on the $(TiO_2)_{38}$ Surface in DSCs – A Theoretical Study

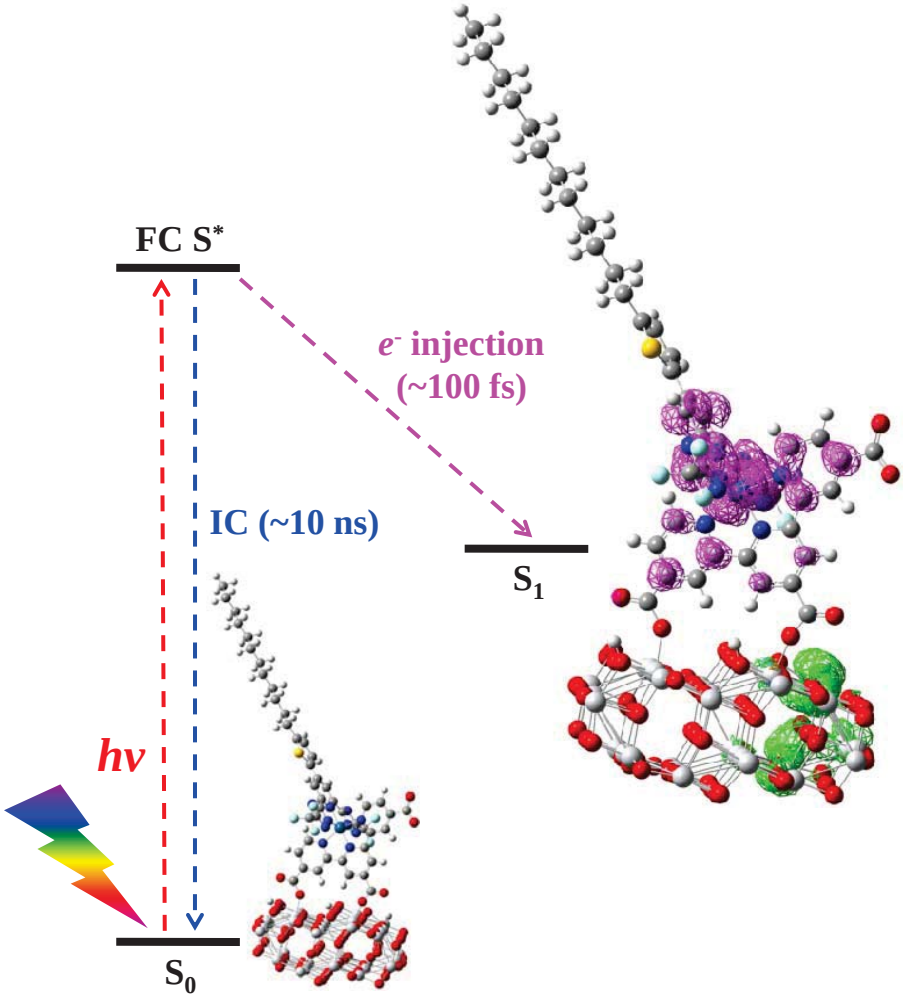


In the panchromatic Os(II)–based TF-52-Os/$(TiO_2)_{38}$ surface in DSCs with the isovalue equal 0.002, the electron density distribution of HOMO is mainly localized at TF-52-Os and a little at the $(TiO_2)_{38}$ surface. At the same time, the electron density distribution of LUMO is mainly delocalized at the $(TiO_2)_{38}$ surface and few at TF-52-Os. Therefore, the lowest singlet optical transition ($S_0 \rightarrow S_1$) process from HOMO→ LUMO in an adiabatic electron transfer with high electronic coupling.

## 2.1 Abstract

In the past decade, Os(II)–based panchromatic dye sensitized solar cells (DSCs) were an alternatively accessible choice to replacing the traditional heavy metal Ru(II)–based dyes. In 2012, we reported two synthesized Os(II)–based dyes with photo-current conversion efficiency reaching 8.85% in our experimental research. In this theoretical study, we performed the simulation regarding two Os(II)– (TF-51-Os and TF-52-Os) and two Ru(II)–based (TF-51-Ru and TF-52-Ru) dyes anchoring onto the anatase (101) $(TiO_2)_{38}$ surface. In total, we simulated four dye/$(TiO_2)_{38}$ surface models. Based on the same structures (TF-51-Os *vs*. TF-51-Ru and TF-52-Os *vs*. TF-52-Ru), we could make a comparative study relating the Os(II)– and Ru(II)–based dyes in DSCs. By the way, we also quantitatively estimated the electronic coupling between the dye and $(TiO_2)_{38}$ interfacial interaction using the Generalized Mulliken–Hush (GMH) theory with configuration–interaction singles (CIS) method. This article is the first report theoretically studying about the Os(II)–based dye in DSCs, and we believe that it could open a new doorway in the heavy metal based dye/$TiO_2$ research field.

## 2.2 Introduction

Dye-sensitized solar cells (DSCs) have been considered as a practical and accessible alternative to the conventional amorphous silicon solar cells due to their cost-effectiveness and highly efficient conversion of photovoltaic energy.[1–4] In 2011, Grätzel and his coworkers operated the DSCs using zinc porphyrin dye (YD2-o-C8) reaching 12.3%.[5] The DSCs devices are composed of a nanocrystalline $TiO_2$ anatase (101) film adsorbed by organic or inorganic dyes as the sensitizer, the latter of which are mainly based on a heavy metal Ru(II)–based transition metal complexes. When the dye molecule is excited by the absorption of sunlight, an excited electron of the dye is then injected into the conduction band of $TiO_2$. The electron is then transported to the external circuit and the dye molecule is regenerated by redox reaction coupled to e.g. the $I^-/I_3^-$ ion pair in electrolyte. The mechanism of the electron injection into $TiO_2$ from the dye incorporates an ultrafast interfacial electron transfer process (~100 fs) and is a key procedure in DSCs[3]. The presence of an ultrafast electron injection suggests that the energy of LUMO of the dye should lie well above the conduction band edge of $TiO_2$ (–4.00 eV *vs.* vacuum).[2] Additionally, the HOMO energy level of the dye should be lower than the redox potential of $I^-/I_3^-$ (–4.90 eV *vs.* vacuum),[4] leading to a fast dye regeneration and avoiding the recombination of the ejected electrons back into the oxidized dye molecules. From the theoretical view point, the dye/$TiO_2$/electrolyte

interaction is still a complicated system in practice. Interested readers can refer eight recent review articles regarding theoretical approaches in dye/$TiO_2$ surface system.[6–13]

The traditional heavy metal Ru(II)–based coordination complexes are effective sensitizers for DSCs due to their lower metal-to-ligand charge transfer (MLCT) energy gap. Some DSCs incorporating Ru(II)–based sensitizers have shown incident photon-to-current conversion efficiency (IPCE) under the red and near-infrared region of the solar spectrum.[3] The Ru(II)–based dyes in DSCs are panchromatic. During the past decade, three prototypical Ru(II) dyes, N3, N719, and N749 (black dye) have been the core of Ru(II)–based dyes developed in DSCs.[3] Simulations on N3/$TiO_2$[14–17], N719/$TiO_2$[18–22], and N749/$TiO_2$[23–27] models have been studied by several groups, including our previous study concerning N749/$(TiO_2)_{28}$ with different protonation forms.[25] There were other theoretical study relating the Ru(II)–based dye anchoring onto the $TiO_2$ surface, such as $Ru^{II}(tpy)_2$[28], N1044[29], C101[30], C106[31], and Z907[10].

In the past several years, the Os(II)–based dyes applying in the DSCs were an alternative choice replacing the traditional Ru(II)–based dyes.[32–39] In order to harvest lower energy photons, Os(II)–based dyes seem to be an excellent option for expanding the spectral response well in the near infrared (NIR) region. Os(II)–based polypyridine complexes show lower energy metal-to-ligand charge-transfer (MLCT) transition, as a consequence of the lower oxidation potential and higher $\pi$ orbital energy compared to

their Ru(II)–based counterparts.[40–43] In addition, larger spin-orbital coupling for the heavier Os(II) cation, in theory, induces nontrivial absorption of the $^3$MLCT states extended to even lower energy. Thus, appropriately designed Os(II) sensitizers should display a much broader absorption profile and faster electron injection from both nonthermalized $^1$MLCT and thermalized $^3$MLCT excited states.[40–43] Interested readers can refer our four review articles regarding the heavy metal based polypyridine complexes (including Os(II) and Ru(II) complexes).[40–43] The Os(II)–based dyes in DSCs are also panchromatic as well as the Ru(II)–based dyes. In 2012, we reported two synthesized Os(II)–based dyes (TF-51 and TF-52) in DSCs with the photo-current conversion efficiency reaching 8.85%.[37] There was also another Ru(II)–based dye named TF-5 in our previous experimental research.[36] TF-51 and TF-5 have the same structure just with the different central heavy metal. In this theoretical study, we simulate TF-51, TF-52, and TF-5 anchoring onto the $TiO_2$ surface. Due to a better comparative distinguishing between the Os(II)– (TF-51 and TF-52) and Ru(II)–based (TF-5) dyes, we rename TF-51, TF-52, and TF-5 replacing a new name TF-51-Os, TF-52-Os, and TF-51-Ru, respectively. For a comprehensive comparison, we also perform an imaginary Ru(II)–based dye named TF-52-Ru. TF-52-Os and TF-52-Ru have the same framework just with the different central heavy metal. The name of TF-51-Os, TF-51-Ru, TF-52-Os, and TF-52-Ru is Os(tcetpy)(pybtz), Ru(tcetpy)(pybtz),

Os(tcetpy)(thpybtz), and Ru(tcetpy)(thpybtz), respectively. The tcetpy is 4,4',4''-tricarboxy-2,2':6,2''-terpyridine; pybtz is 2,6-bis(3-trifluoromethyl-1H-1,2,4-triazol-5-yl)pyridine; thpybtz is 4-(5-dodecylthiophen-2-yl)-2,6-bis(3-(trifluoromethyl)-1H-1,2,4-triazol-5-yl)pyridine. In a word, we simulate four dye/$TiO_2$ surface models in this study. To our best knowledge, the theoretical simulation in the Os(II)–based dye anchoring onto the $TiO_2$ surface is not yet reported. It is the first time to perform the Os(II)–based dye on the $TiO_2$ surface in this study.

TF-51-Os, TF-51-Ru, TF-52-Os, and TF-52-Ru all have the tridentate terpyridine carboxylic group. From chemistry point of view, these terpyridine anchoring dyes latently possess superior stability suited for practical application. Despite three carboxylic groups being capable of anchoring on the $TiO_2$ surface, these four dyes are keen on adsorbing on the $TiO_2$ surface by a bidentate and bridging coordination mode according to the experimental[44–45] and theoretical[25–27] results, where two O atoms, each from a different carboxylate groups, attaching monodentately to the Ti atoms on the $TiO_2$ surface. In other words, two carboxylate groups are enough to create a stable adsorption site on the $TiO_2$ surface, and the third carboxylic group is dangling above the $TiO_2$ surface. The form of "bidentate carboxylate anchoring on the Ti atoms of $TiO_2$ surface" has been examined theoretically using the terpyridine Ru(II)–based dye such as

N749 in attempts to understand both the improved conversion efficiency and stability.[25–27]

The unit cell of $TiO_2$ anatase (101) is $(TiO_2)_4$ and its space group is no. 141 [I 41/a m d :2]. In the $TiO_2$ anatase (101) surface nanocluster, each O atom is nearly binding with two Ti atoms physically. The smallest possible reasonable $TiO_2$ anatase (101) nanocluster is $(TiO_2)_{16}$.[46] The next larger reasonable ones are $(TiO_2)_{28}$, $(TiO_2)_{38}$, or $(TiO_2)_{46}$.[47] In Chapter I, we used the $(TiO_2)_{28}$ surface as our simulation model. In this chapter (Chapter II), we make a further progress using the $(TiO_2)_{38}$ surface as our simulation model. The surface area of the $(TiO_2)_{38}$ is suitable for the bidentate carboxylate groups of the four dyes to anchor onto.

By the way, we try to estimate the electronic coupling in the dye/$(TiO_2)_{38}$ models quantitatively. We use the generalized Mulliken–Hush (GMH) theory[48–52] developed by Cave and Newton[48] in the electronic coupling calculation with configuration–interaction singles (CIS)[53] method. The details of results and discussion are elaborated in the following sections.

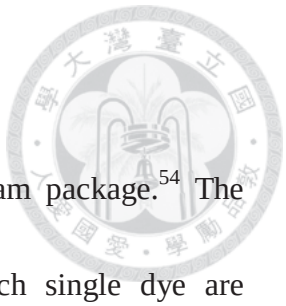

## 2.3 Models and Computational Methods

All the calculations are performed with the Gaussian 09 program package.[54] The ground state geometry of pure $(TiO_2)_{38}$ surface cluster and each single dye are optimized first, and then each ground state geometry of dye/$(TiO_2)_{38}$ composite is fully optimized. The geometry optimizations of the ground states are all performed with density functional theory (DFT) at B3LYP/LANL2DZ (Os, Ru, Ti) and B3LYP/6-31G* (H, C, N, O, F, S) level. By the way, the optimized lowest singlet ($S_1$) structures of the dye/$(TiO_2)_{38}$ model are simulated at CIS/LANL2DZ (Os, Ru, Ti) and CIS/6-31G* (H, C, N, O, F, S) level. The optimized structures of dye/$(TiO_2)_{38}$ models are then used to calculate the 50 lowest singlet electronic transitions using time dependent density functional theory (TD-DFT) method. The lowest triplet excited state energy of each model is also calculated. We use n,n-Dimethylformamide (DMF) as the solvent, which is used as well as in our previous experimental research. The solvation effect is based on the conductor-like polarizable continuum model (C-PCM), which is implemented in the Gaussian 09 program.

In this study, we take four dyes including two Os(II)– (TF-51-Os and TF-52-Os) and two Ru(II)– (TF-51-Ru and TF-52-Ru) dyes (see Figure 2.1 for their structures). We perform four tridentate terpyridine carboxylic dyes anchoring onto the $(TiO_2)_{38}$ surface including TF-51-Os/$(TiO_2)_{38}$, TF-51-Ru/$(TiO_2)_{38}$, TF-52-Os/$(TiO_2)_{38}$, and

TF-52-Ru/$(TiO_2)_{38}$. We take the deprotonated form in the dye/$(TiO_2)_{38}$ models (which means all the three carboxylic protons transferred onto the $(TiO_2)_{38}$ surface), because the deprotonated form is more thermodynamically stable than the protonated form (which means two of the carboxylic protons transferred onto the $(TiO_2)_{38}$ surface and the third carboxylic proton stay in the dangling carboxylic group) according to the theoretical literatures.[20–22,25–27]

## 2.4 Results and Discussion

### 2.4.1 $(TiO_2)_{38}$ Surface and Associated Behaviors of the four dye/$(TiO_2)_{38}$ Models

We adopt the $(TiO_2)_{38}$ surface cluster as our simulation model, for which the full geometry optimized structure is depicted in Figure 2.2. The $(TiO_2)_{38}$ cluster possesses a nearly planar structure and its surface area is suitable for the four dyes with the bidentate bicarboxylate (of the tridentate tricarboxylate) to anchor onto. The estimation of LUMO in this study is originated from "HOMO add the lowest singlet $S_0 \rightarrow S_1$ excitation energy" and this procedure is experimentally nature. The HOMO and LUMO energy levels of the $(TiO_2)_{38}$ surface in DMF are calculated to be –7.21 and –3.98 eV, respectively. The $S_0 \rightarrow S_1$ optical gap is calculated to be 3.23 eV, which is only slightly larger than the experimental band gap of ~3.20 eV for the nano-sized $TiO_2$,[2] supporting the validity of current theoretical approach based on the $(TiO_2)_{38}$ surface cluster. We then focus on the thermodynamics and the adsorption energies for the four dyes onto $(TiO_2)_{38}$. The optimized geometries, calculated adsorption energies, and O–Ti (between carboxylate O atom and Ti atom) distances of these four dye/$(TiO_2)_{38}$ models are shown in Figure 2.2. The adsorption energy, $E_{ads}$, is defined as $E_{ads} = E_{dye/(TiO2)38} - [E_{dye} + E_{(TiO2)38}]$ where $E_{dye/(TiO2)38,}$ $E_{dye}$ and $E_{(TiO2)38}$ denote the optimized energy of the dye/$(TiO_2)_{38}$ assembly, isolated dye, and $(TiO_2)_{38}$, respectively. The adsorption is expected to be exothermic, which is a prerequisite for the formation of dye/$(TiO_2)_{38}$ due

to the negative entropic change of the adsorption process. Evidently, as shown in Figure 2.2, the calculated adsorption energies of all the four dye/$(TiO_2)_{38}$ surface models are negative (~ –80kcal/mol); thus each dye/$(TiO_2)_{38}$ assembly is thermodynamically stable. In addition, the O–Ti distances between the carboxylate O atoms and Ti atoms of these four dye/$(TiO_2)_{28}$ cluster models are calculated to be within 1.94 to 1.97 Å (see Figure 2.2), which are in good agreement with the reported experimental value of N749/$TiO_2$ ranging from 1.92 to 1.97 Å.[44] However, although we do not measure the actual O–Ti distances of the four dye/$TiO_2$ experimentally, we believe that the O–Ti distances should close to the N749/$TiO_2$. We then illustrate the electronic properties for each dye/$(TiO_2)_{38}$ model elaborated as follows.

### 2.4.2 Frontier Molecular Orbitals and Absorption Spectra

The electron density distributions in HOMOs and LUMOs of these four dye/$(TiO_2)_{38}$ models show no obvious differences. The HOMOs are only located at the Os(II)– or Ru(II)–based dyes, while the LUMOs are localized at the $(TiO_2)_{38}$ surface or delocalized at the dye/$(TiO_2)_{38}$ interfaces, and the LUMOs form a nearly continuous state (with an isovalue = 0.02, default value in GaussView 5.0) (see Figure 2.3, 2.4, 2.5, 2.6, 2.7 and 2.8). Furthermore, the electron distributions in HOMO, HOMO-1, and HOMO-2 are all localized at the section between Os(II) or Ru(II) center and their terpyridine ligands. The LUMO of each dye/$(TiO_2)_{38}$ is gained from “HOMO plus the

lowest $S_0 \rightarrow S_1$ excitation energy". The calculated HOMO of TF51-Os/$(TiO_2)_{38}$, TF51-Ru/$(TiO_2)_{38}$, TF52-Os/$(TiO_2)_{38}$, and TF52-Ru/$(TiO_2)_{38}$ is –5.31, –5.36, –5.29, and –5.38 eV, respectively, and the LUMO is –3.91, –3.73, –3.89, and –3.74 eV, respectively (see Figure 3). The calculated lowest singlet excitation energy ($S_0 \rightarrow S_1$) of each dye/$(TiO_2)_{38}$ is assigned HOMO → LUMO (see Table 2.1, 2.2, 2.3, and 2.4). The calculated lowest singlet optical excitation energy ($S_0 \rightarrow S_1$) of TF51-Os/$(TiO_2)_{38}$, TF51-Ru/$(TiO_2)_{38}$, TF52-Os/$(TiO_2)_{38}$, and TF52-Ru/$(TiO_2)_{38}$ is 1.40, 1.63, 1.40, and 1.64 eV, respectively. The calculated lowest triplet excitation wavelength ($S_0 \rightarrow T_1$) of TF51-Os/$(TiO_2)_{38}$, TF51-Ru/$(TiO_2)_{38}$, TF52-Os/$(TiO_2)_{38}$, and TF52-Ru/$(TiO_2)_{38}$ is 887.4, 760.2, 885.5, and 756.1 nm, respectively, which is located in the near infrared (NIR) region (see Table 2.1, 2.2, 2.3, and 2.4). All LUMOs are higher than the experimental energy level of the $TiO_2$ conduction band (–4.0eV), and all HOMOs are lower than the experimental redox potential of $I^-/I_3^-$ (–4.9 eV). Accordingly, these four dye/$(TiO_2)_{38}$ models are predicted to operate well in the DSCs. In addition, the HOMO and $S_0 \rightarrow S_1$ excitation energy of Os(II) dye/$(TiO_2)_{38}$ are lower and than the corresponding Ru(II)–dye/$(TiO_2)_{38}$ model, such as TF51-Os/$(TiO_2)_{38}$ *vs.* TF51-Ru/$(TiO_2)_{38}$ and TF52-Os/$(TiO_2)_{38}$ *vs.* TF52-Ru/$(TiO_2)_{38}$. This result indicates that Os(II)–dye/$(TiO_2)_{38}$ can harvest lower energy photon (red shift) than Ru(II)–dye/$(TiO_2)_{38}$, which is in good agreement according to our four review

articles.[40–43] The optical transitions of these four dye/$(TiO_2)_{38}$ models are mainly transferring from HOMO, HOMO-1 or HOMO-2 to LUMOs, and are ascribed as an interfacial charge transfer process (see Tables 2.1, 2.2, 2.3, and 2.4). The distribution of the calculated oscillator strengths of TF51-Os/$(TiO_2)_{38}$, TF51-Ru/$(TiO_2)_{38}$, and TF52-Os/$(TiO_2)_{38}$ are in good trend in comparison with their corresponding experimental spectrum (see Figure 2.9 (a), (b), and (c)). Because TF-52-Ru is not synthesized yet, we do not have the experimental spectrum of TF52-Ru/$(TiO_2)_{38}$. We only depict the calculated oscillator strengths distribution (see Figure 2.9 (d)). Because the experimental and calculated spectral of TF51-Os/$TiO_2$ and TF52-Os/$(TiO_2)_{38}$ are similar, we could conclude that the experimental and calculated spectral of TF51-Ru/$TiO_2$ and TF52-Ru/$(TiO_2)_{38}$ are similar.

Based on the illustration in Figure 3 (isovalue = 0.02, default value in GaussView 5.0), the electron density distribution of HOMO and LUMO in each dye/$(TiO_2)_{38}$ model is at the dye and the $(TiO_2)_{38}$ surface, respectively. In a result, the electron density distribution of HOMO and LUMO in the default isovalue scale of GaussView are not overlap. Therefore, the calculated lowest singlet optical transition ($S_0 \rightarrow S_1$) is seemed to ascribed as a “photo-induced electron transfer process”. However, in the actually experimental DSCs, the electron injection process from the excited state of the dye into the $TiO_2$ surface is within the ultrafast timescale (~100 fs),[3,27] and it should be supposed

a small adiabatic electronic coupling process in the dye/$TiO_2$ interaction and ascribed an "slightly optical electron transfer process". But in many theoretical researches relating about the Ru(II)–dye/$TiO_2$ models[20,21,25,27] including our previous study regarding N749/$(TiO_2)_{28}$,[25] we do not see the comparison between "the photo-induced electron transfer process" and "the slightly optical electron transfer process" in the $S_0 \rightarrow S_1$ (HOMO → LUMO) transition. If we set the isovalue = 0.002 for the contours (which is equivalent to amplify the electron density distribution vision scale) of HOMO and LUMO in each dye/$(TiO_2)_{38}$ model (see Figure 2.10), we then discovery that the electron density distribution of HOMO of each dye/$(TiO_2)_{38}$ model has little delocalization in $(TiO_2)_{38}$ and the LUMO has few electron density in the carboxylic groups of each dye. This LUMO delocalization in the carboxylic groups in a smaller isovalue (which is equivalent to enlarge the electron density vision scale) is in good agreement with the $N_3$/$TiO_2$ report.[15,16] We then combine the electron density distribution of HOMO and LUMO of each dye/$(TiO_2)_{38}$ model together in the isovalue scale = 0.002 (see Figure 2.11), and we observe that the HOMO and LUMO are overlap resulting a moderate electronic coupling at the dye/$(TiO_2)_{38}$ interfacial region. Furthermore, we list the electron contribution of every molecular fragment and molecular orbital in each dye/$(TiO_2)_{38}$ model (see Table 2.5, 2.6, 2.7, 2.8 and 2.9), We see that the heavy metal Os(II) or Ru(II), terpyridine, and the two anchored carboxylic

groups have little delocalization in LUMO and the $(TiO_2)_{38}$ has few distribution in HOMO in each dye/$(TiO_2)_{38}$ model. The six F atoms have zero distribution in all LUMOs in each dye/$(TiO_2)_{38}$ model. The three anchored carboxylic protons in each dye/$(TiO_2)_{38}$ only are localized at the $(TiO_2)_{38}$ surface and have no more than 0.37% contrition. By the way, TF-52-Os/$(TiO_2)_{38}$ and TF-52-Ru/$(TiO_2)_{38}$ both have the long alkyl chain $–C_{12}H_{25}$, and the moiety $–C_{12}H_{25}$ has no electron density disbribution in all molecular orbital exception of HOMO-1 (1.06% and 0.24%, respectively) (see Table 2.8, 2.9, Figure 2.12, and 2.13). In Figure 2.12 and 2.13, we see that the butyl part of $–C_{12}H_{25}$ nearly conneting the thiophene moiety has little electron density distribution in HOMO-1 of TF-52-Os/$(TiO_2)_{38}$ (1.06%) and TF-52-Ru/$(TiO_2)_{38}$ (0.24%). Therefore, in the dye/$TiO_2$ simulation with carrying long alkyl chain, it is not a good idea to reduce the long alkyl chain to the methyl group. In the following section, we will use a theoretical method to quantitatively estimate the electronic coupling value in the dye/$(TiO_2)_{38}$ interface.

### 2.4.3 Electronic Coupling Estimation

The experimental time scale in the electron injection process of dye/$TiO_2$ is within ~100 fs,[3,27] and this ultrafast electron transfer process is supposed a slightly adiabatic donor(D)/acceptor(A) coupling process and assumed a moderate D/A interaction. In the experimental ultrafast electron injection process, the lowest singlet optical transition ($S_0$

→ $S_1$) is believed as the slowest transition among the process from ground to highly excited states. Therefore, we only consider the $S_0 \rightarrow S_1$ excitation process to estimate the electronic coupling. According to the time-dependent perturbation theory in quantum mechanism, the full Hamiltonian in a system is $\hat{\hat{H}} = H_0 + V(t)$, where $\hat{V}(t) = \hat{\mu} \cdot E_0 \cos(\omega t)$ . $\hat{V}(t)$ is the time-dependent perturbation, $\hat{\mu}$ is the dipole moment operator, and $E_0 \cos(\omega t)$ is the external electrical field varying with the time. Dirac and Fermi have developed the famous Fermi's golden rule to describe the electron transfer rate constant as $k_{ET} = \frac{2\pi}{\hbar} |H_{ab}|^2 \delta(E_a - E_b - \hbar\omega)$ , where $|H_{ab}|$ is the electronic coupling matrix element between state *a* and *b* and $\delta(E_a - E_b - \hbar\omega)$ is the density of state (DOS) between state *a* and *b*, respectively.[55] In the traditional D/A electron transfer, Marcus theory is used to describe the nonadiabatically electronic coupling process.[56] Because the electron injection process in the dye/$TiO_2$ interface is an adiabatic coupling process experimentally, thus, Marcus theory is not suitable for applying here. We have to search for other theoretical methods to estimate the adiabatic electronic coupling in the dye/$TiO_2$ interface. Unforturally, there is not an effectively universal formula determining the electronic coupling yet.[50] From the physical and chemical view point, the most convenient way is taking the two-level system concept. Because the time-dependent perturbation in the system Hamiltonian is composed by the dipole moment operator, we would like to adopt the generalized Mulliken–Hush (GMH)

theory[48–52] developed by Cave and Newton[48] as our theoretical foundation. The GMH theory is formulated as

$$H_{ab} = \frac{m_{ab}\Delta E_{ab}}{\sqrt{(\Delta\mu_{ab})^2 + 4(m_{ab})^2}} \quad (1)$$

where $m_{ab}$ is the transition electronic dipole moment connecting the two diabatic states *a* and *b*, $\Delta E_{ab}$ is the difference in energy between the two diabatic states *a* and *b*, and $\Delta\mu_{ab}$ is the difference in dipole moment between the two diabatic states *a* and *b*. This GMH formula is established the dipole moment operator which is according to the chemical intuition.[48–52] Interested readers can refer the derivation of the GMH formula in reference 50 and 51. Recently, both the GMH formula and Marcus theory were used in a theoretical analysis estimating the electronic coupling in the catechol and the sandwich single-walled $TiO_2$ nanotube (STNT) heterogeneous interface.[57] We need two diabatic states to represent the initial and final states of the adiabatic electron transfer process in the dye/$TiO_2$ interface. However, the exactly diabatic states do not usually exist.[50,58] We can get information about the diabatic states in reference 49–52, "the diabatic states are the linear combination of the adiabatic states that maximize the dipole moment difference between the pair of states" which is equivalent to "the diabatic states are the linear combination of the adiabatic states have the greatest charge separation between the initial and final states".[49–51] "Crudely, we are taking combinations of the

adiabatic states to get the two most localized (diabatic) states".[49–52] But, the critical key point is "how to accurately find two diabatic states in the adiabatic coupling process of the dye/$TiO_2$ interface?" It is not a easy task to select the two diabatic states in the adiabatic coupling process of the dye/$TiO_2$ interface. We use the CIS method to determine the two diabatic states.[53] According to the display in Figure 2.10, 2.11 and Table 2.1, the electron density distribution in HOMO and LUMO is few delocalized in $(TiO_2)_{38}$ and dye, respectively, indicating the HOMO and LUMO overlap indeedly during the $S_0 \rightarrow S_1$ transition. Therefore, the $S_0 \rightarrow S_1$ transition should have a moderate electron coupling. In this study, we only pay attention to the singlet–singlet transition, and the singlet–triplet intersystem crossing (ISC) is not considered here. Therefore, the electron injection process in the dye/$TiO_2$ only competes with the internal conversion (IC) process. However, the time scale in the electron injection process (~100 fs) is much faster than the IC process (~10 ns).[3] Based on our experimentally and theoretically chemical intuition, we approximately adopt the Frank-Condon excited S* and the excited geometry optimized medium state $S_1$ as the initial (donated *a*) and final (donated *b*) diabatic states, respectively (see Figure 2.14). The electronic coupling of TF-51-Ru/$(TiO_2)_{38}$ and TF-52-Ru/$(TiO_2)_{38}$ is 2004.15 and 2540.48 $cm^{-1}$, respectively, (>> 200 $cm^{-1}$ at room temperature *k*T), just roughly in the electron transfer time scale < 100 fs (see Table 2.10, 2.11, and 2.12). Therefore, the $S_0$

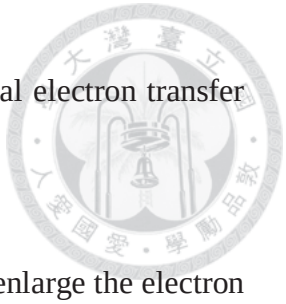

→ $S_1$ transition (HOMO → LUMO) is theoretically a slightly optical electron transfer process indeed.

In a word, we can set the isovalue = 0.002 (which is equivalent to enlarge the electron density distribution vision scale ) in HOMO and LUMO graphically and use the GMH formula to understand the $S_0$ → $S_1$ transition (HOMO → LUMO) quantitatively being an optical electron transfer process in the dye/$TiO_2$ interface.

## 2.5 Conclusion

In summary, we provide a compact model incorporating $(TiO_2)_{38}$ assembly for accessing the adsorption of the Os(II)– and Ru(II)–based dyes with tridentate terpyridine anchoring group. Four distinctive dye/$(TiO_2)_{38}$ surface models are investigated with the Gaussian 09 software package. Various properties such as optimized structures, O–Ti distances, adsorption energies, frontier molecular orbitals, and TD-DFT UV-VIS excitation spectra have been calculated and a fair comparison with the experimental results have been made. The lowest singlet optical transition ($S_0 \rightarrow S_1$) of the two Os(II) dye/$(TiO_2)_{38}$ (TF-51-Os/$(TiO_2)_{38}$ and TF-52-Os/$(TiO_2)_{38}$) models are more red shift than the corresponding two Ru(II) dye/$(TiO_2)_{38}$ (TF-51-Ru/$(TiO_2)_{38}$ and TF-52-Ru/$(TiO_2)_{38}$) models. We also set the isovalue = 0.002 (which is equivalent to enlarge the electron density distribution vision scale) in HOMO and LUMO and use the GMH formula to estimate the electron transfer electron coupling in the $S_0 \rightarrow S_1$ optical transition (HOMO → LUMO) theoretically, and it is an optical electron transfer process in the dye/$TiO_2$ interface which is according to the experimental spectroscopic study. Accordingly, we have demonstrated that the suitable $(TiO_2)_{38}$ assembly can be used to simulate real-life experimental data with good

reliability. Due to the readily accessible in computation capability for most of laboratories, new and more efficient Os(II) sensitizers may be strategically designed via simulation prior to the execution of synthetic work, saving the redundant synthetic efforts and suited for the demand of vast evaluation of the DSCs sensitizers.

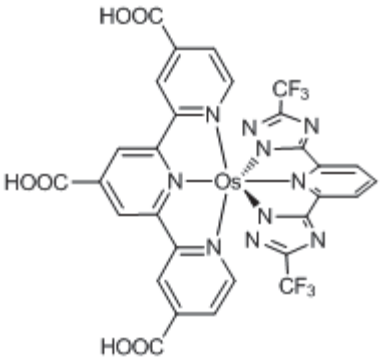


(a) TF-51-Os

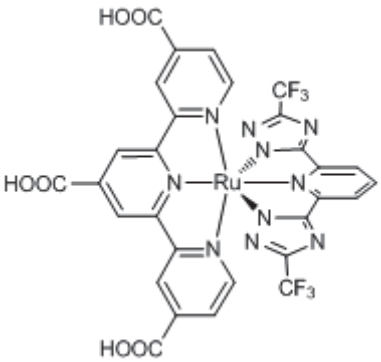


(b) TF-51-Ru

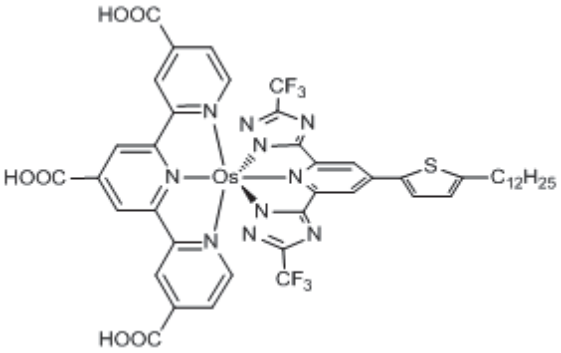


(c) TF-52-Os

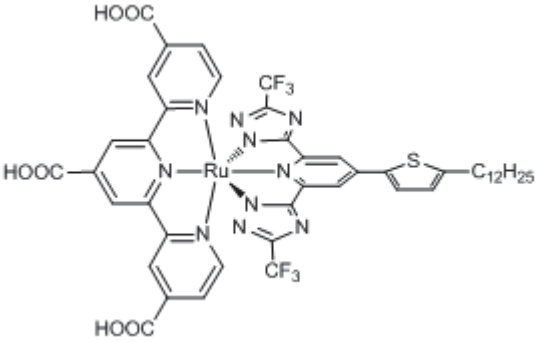


(d) TF-52-Ru

**Figure 2.1** Molecular structures of compound (a) TF51-Os, (b) TF51-Ru, (c) TF52-Os, and (d) TF52-Ru.

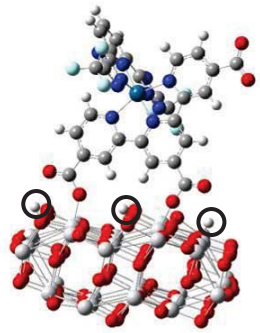

(a) TF51-Os/$(TiO_2)_{38}$
O–Ti = 1.96 and 1.94 Å
$E_{ads}$ = –82.09 kcal/mol

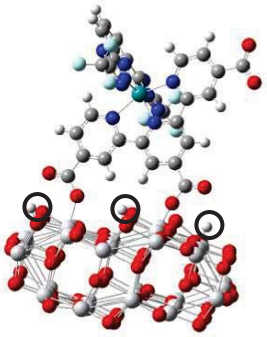

(b) TF51-Ru/$(TiO_2)_{38}$
O–Ti = 1.95 and 1.94 Å
$E_{ads}$ = –83.94 kcal/mol

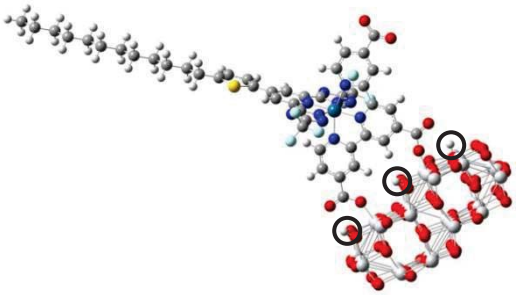

(c) TF52-Os/$(TiO_2)_{38}$
O–Ti = 1.97 and 1.94 Å
$E_{ads}$ = –82.79 kcal/mol

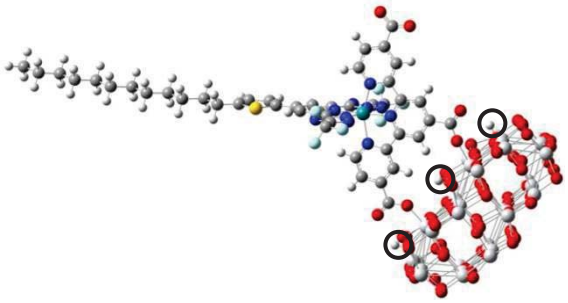

(d) TF52-Ru/$(TiO_2)_{38}$
O–Ti = 1.94 and 1.94 Å
$E_{ads}$ = –80.25 kcal/mol

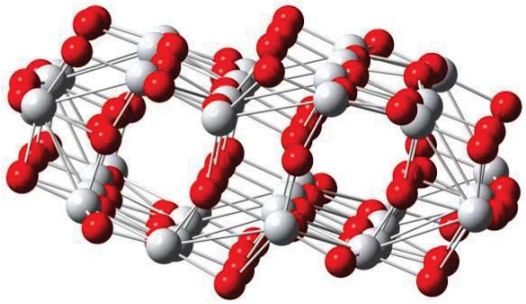

(e) $(TiO_2)_{38}$

**Figure 2.2** Optimized geometries, O–Ti distances (left and right side), and adsorption energies of (a) TF51-Os/$(TiO_2)_{38}$, (b) TF51-Ru/$(TiO_2)_{38}$, (c) TF52-Os/$(TiO_2)_{38}$, (d) TF52-Ru/$(TiO_2)_{38}$, and (e) $(TiO_2)_{38}$ models. The carboxylic protons on the $(TiO_2)_{38}$ surface are indicated by a circle symbol.

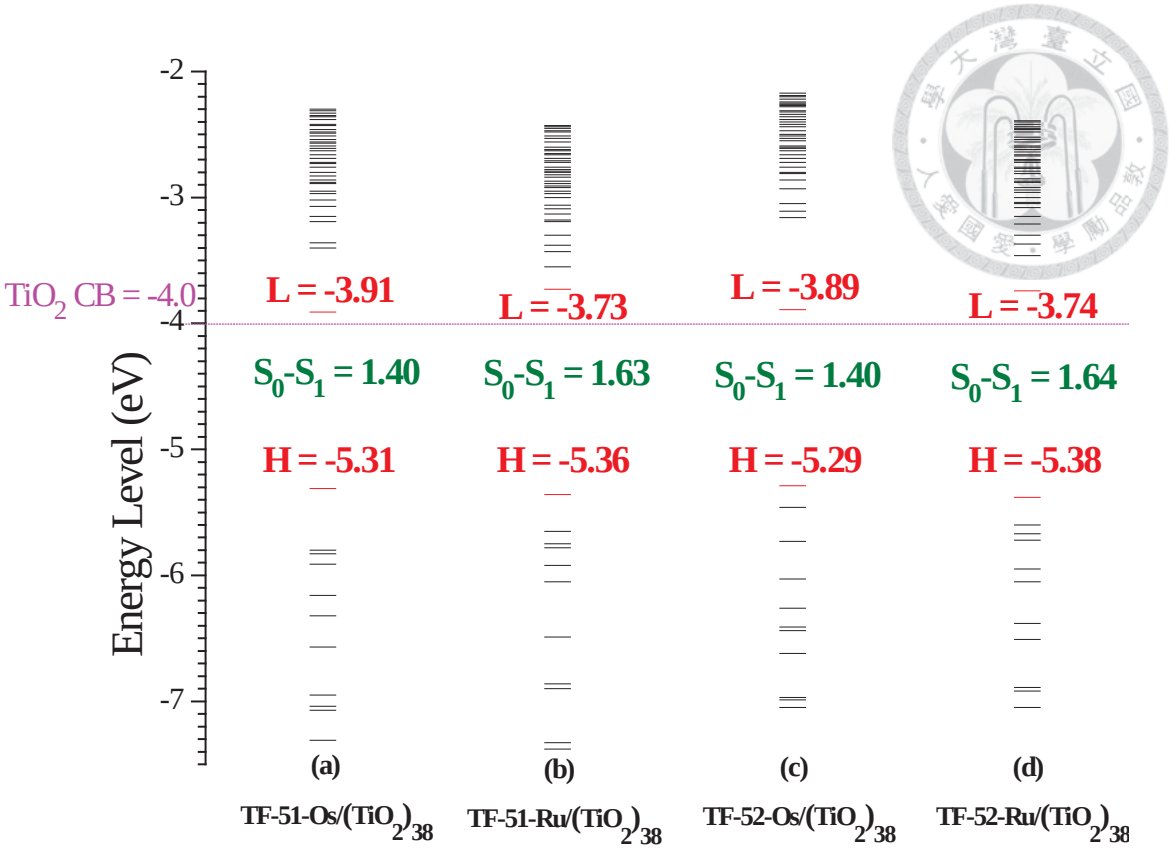


**Figure 2.3** Molecular orbital energy level (eV) diagram from HOMO-10 to LUMO+40 of (a) TF-51-Os/$(TiO_2)_{38}$, (b) TF-51-Ru/$(TiO_2)_{38}$, (c) TF-52-Os/$(TiO_2)_{38}$, and (d) TF-52-Ru/$(TiO_2)_{38}$. CB = conduction band, H = HOMO, L = LUMO, $S_0$–$S_1$ stands for the calculated first singlet excited state energy.

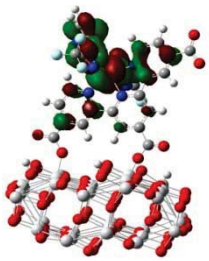

(a-1) HOMO of TF-51-Os/$(TiO_2)_{38}$

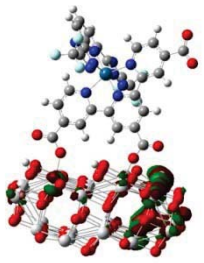

(a-2) LUMO of TF-51-Os/$(TiO_2)_{38}$

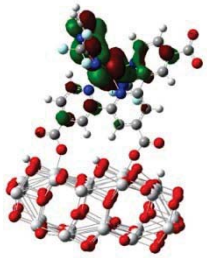

(b-1) HOMO of TF-51-Ru/$(TiO_2)_{38}$

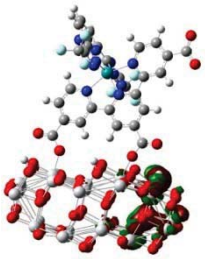

(b-2) LUMO of TF-51-Ru/$(TiO_2)_{38}$

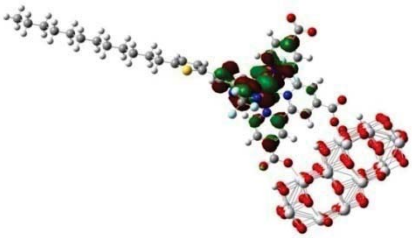

(c-1) HOMO of TF-52-Os/$(TiO_2)_{38}$

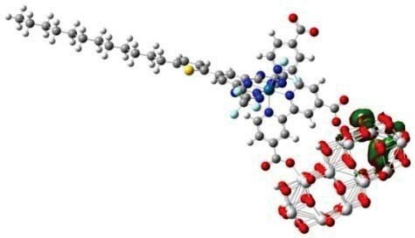

(c-2) LUMO of TF-52-Os/$(TiO_2)_{38}$

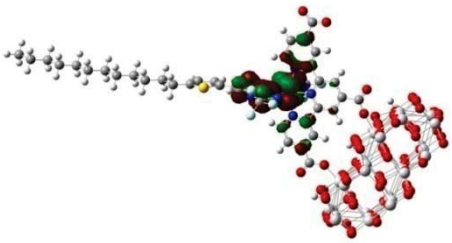

(d-1) HOMO of TF-52-Ru/$(TiO_2)_{38}$

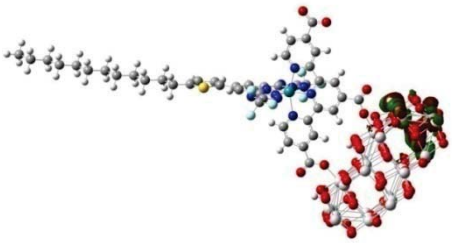

(d-2) LUMO of TF-52-Ru/$(TiO_2)_{38}$

**Figure 2.4** HOMO and LUMO of (a) TF-51-Os/$(TiO_2)_{38}$, (b) TF-51-Ru/$(TiO_2)_{38}$, (c) TF-52-Os/$(TiO_2)_{38}$, and (d) TF-52-Ru/$(TiO_2)_{38}$ models. The isovalue for the contours is 0.02 (default value in Gaussview 5.0).

**Table 2.1** The wavelengths, transition probabilities and charge transfer characters of the singlet optical transitions in selected states with oscillator strength > 0.0004 for TF-51-Os/$(TiO_2)_{38}$. The lowest triplet transition ($S_0 \rightarrow T_1$) is also listed.

| State | $\lambda_{cal}$ (nm) | $f$ | Assignments |
|---|---|---|---|
| $T_1$ | 887.4 | 0 | HOMO→LUMO(100%) |
| $S_1$ | 887 | 0.0003 | HOMO→LUMO(100%) |
| $S_2$ | 769.4 | 0.0102 | HOMO→LUMO+1(90%) |
| $S_3$ | 727.8 | 0.0035 | HOMO→LUMO+2(72%) HOMO→LUMO+3(6%) |
| $S_4$ | 711 | 0.0025 | HOMO→LUMO+3(61%) HOMO→LUMO+2(26%) |
| $S_7$ | 661.6 | 0.0026 | HOMO→LUMO+3(86%) |
| $S_9$ | 624.4 | 0.0015 | HOMO→LUMO+5(94%) |
| $S_{11}$ | 611.1 | 0.0017 | HOMO→LUMO+6(94%) |
| $S_{14}$ | 584.7 | 0.0043 | HOMO-2→LUMO+1(73%) HOMO→LUMO+8(21%) |
| $S_{15}$ | 583.8 | 0.0021 | HOMO→LUMO+8(65%) HOMO-2→LUMO+1(23%) |
| $S_{20}$ | 560.4 | 0.0024 | HOMO-2→LUMO+2(44%) HOMO-1→LUMO+2(44%) |
| $S_{21}$ | 559.3 | 0.0019 | HOMO-1→LUMO+2(44%) HOMO-2→LUMO+2(44%) |
| $S_{26}$ | 543.6 | 0.0016 | HOMO→LUMO+15(26%) HOMO→LUMO+40(12%) HOMO→LUMO+14(12%) HOMO→LUMO+16(9%) HOMO→LUMO+12(7%) |
| $S_{28}$ | 536.4 | 0.01 | HOMO→LUMO+15(59%) HOMO→LUMO+40(14%) |
| $S_{30}$ | 527.6 | 0.0013 | HOMO→LUMO+19(31%) HOMO→LUMO+17(26%) HOMO→LUMO+15(20%) HOMO→LUMO+20(6%) |
| $S_{32}$ | 524.9 | 0.0038 | HOMO-2→LUMO+3(44%) HOMO-1→LUMO+3(42%) |
| $S_{33}$ | 523.9 | 0.003 | HOMO-1→LUMO+3(49%) HOMO-2→LUMO+3(39%) |
| $S_{34}$ | 519.7 | 0.0006 | HOMO→LUMO+18(82%) HOMO→LUMO+20(8%) |
| $S_{35}$ | 515.4 | 0.0022 | HOMO-1→LUMO+4(50%) HOMO-2→LUMO+4(36%) |
| $S_{36}$ | 514.6 | 0.0038 | HOMO-1→LUMO+4(32%) HOMO→LUMO+19(19%) HOMO→LUMO+20(14%) HOMO→LUMO+21(11%) HOMO→LUMO+18(8%) HOMO-2→LUMO+4(7%) |
| $S_{37}$ | 514.1 | 0.0004 | HOMO-2→LUMO+4(53%) HOMO-1→LUMO+4(15%) HOMO→LUMO+19(8%) HOMO→LUMO+20(8%) HOMO→LUMO+21(5%) |
| $S_{46}$ | 470.6 | 0.0113 | HOMO→LUMO+40(65%) HOMO→LUMO+15(32%) |

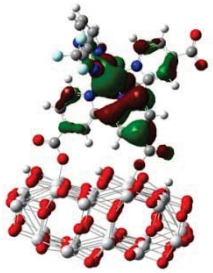

HOMO-2 (–5.83 eV)

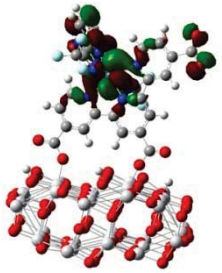

HOMO-1 (–5.80 eV)

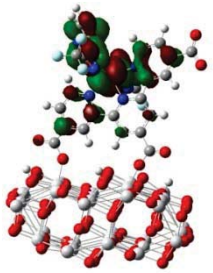

HOMO (–5.31 eV)

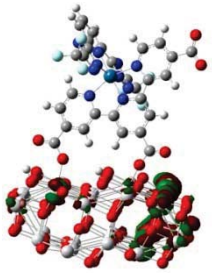

LUMO (–3.91 eV)

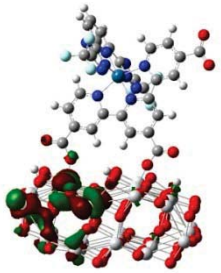

LUMO+1 (–3.40 eV)

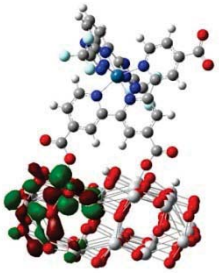

LUMO+2 (–3.36 eV)

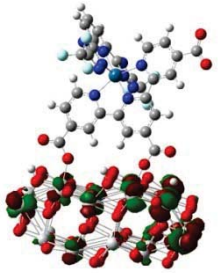

LUMO+3 (–3.19 eV)

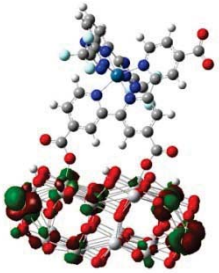

LUMO+4 (–3.15 eV)

**Figure 2.5.1** Frontier molecular orbitals pertinent to the singlet optical transitions in selected states for TF-51-Os/$(TiO_2)_{38}$. The isovalue for the contours is 0.02 (default value in GaussView 5.0).

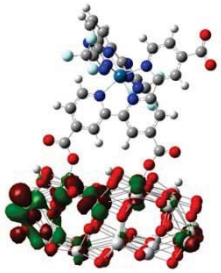

LUMO+5 (–3.07 eV)

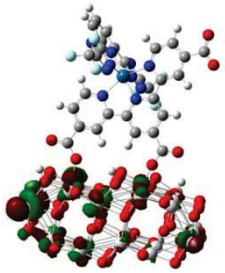

LUMO+6 (–3.02 eV)

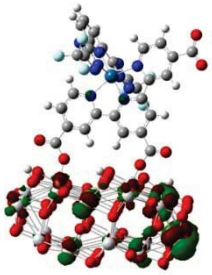

LUMO+8 (–2.95 eV)

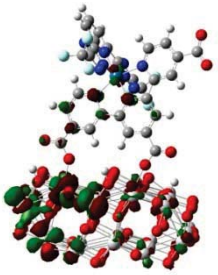

LUMO+12 (–2.83 eV)

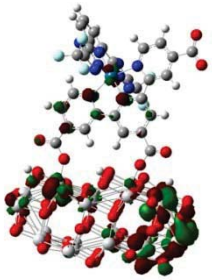

LUMO+14 (–2.80 eV)

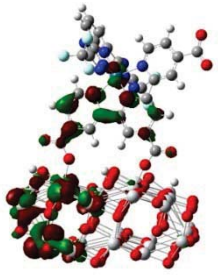

LUMO+15 (–2.76 eV)

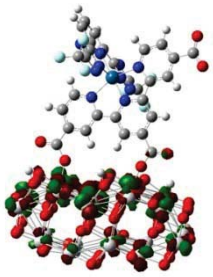

LUMO+16 (–2.73 eV)

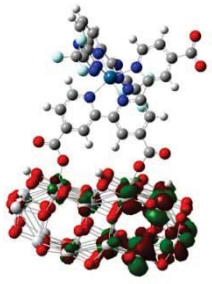

LUMO+17 (–2.72 eV)

**Figure 2.5.2** Frontier molecular orbitals pertinent to the singlet optical transitions in selected states for TF-51-Os/$(TiO_2)_{38}$. The isovalue for the contours is 0.02 (default value in GaussView 5.0).

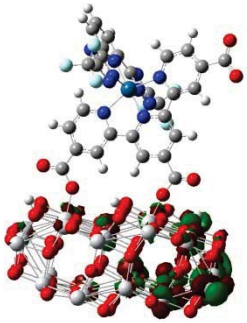

LUMO+18 (–2.69 eV)

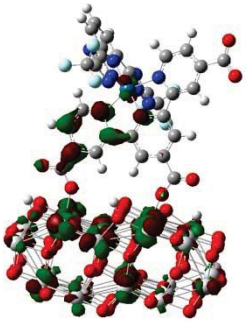

LUMO+19 (–2.66 eV)

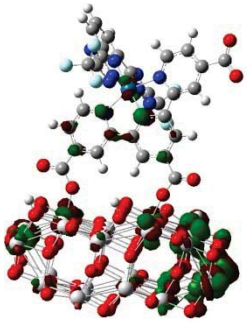

LUMO+20 (–2.63 eV)

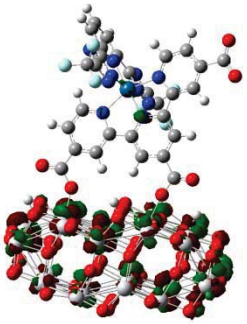

LUMO+21 (–2.61 eV)

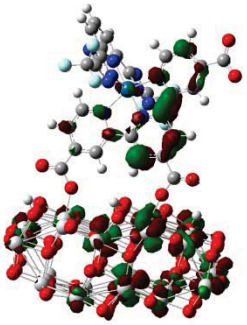

LUMO+40 (–2.30 eV)

**Figure. 2.5.3** Frontier molecular orbitals pertinent to the singlet optical transitions in selected states for TF-51-Os/$(TiO_2)_{38}$. The isovalue for the contours is 0.02 (default value in GaussView 5.0).

**Table 2.2** The wavelengths, transition probabilities and charge transfer characters of the singlet optical transitions in selected states with oscillator strength > 0.0008 for TF-51-Ru/$(TiO_2)_{38}$. The lowest triplet transition ($S_0 \rightarrow T_1$) is also listed.

| State | $\lambda_{cal}$ (nm) | *f* | Assignments |
|---|---|---|---|
| $T_1$ | 760.2 | 0 | HOMO→LUMO(100%) |
| $S_1$ | 760 | 0.0003 | HOMO→LUMO(100%) |
| $S_2$ | 751.2 | 0.0001 | HOMO→LUMO+1(52%) HOMO→LUMO(46%) |
| $S_3$ | 714.8 | 0.0016 | HOMO→LUMO+2(51%) HOMO→LUMO+3(40%) |
| $S_4$ | 660.5 | 0.0102 | HOMO→LUMO+2(96%) |
| $S_5$ | 647.7 | 0.0009 | HOMO→LUMO+4(92%) |
| $S_7$ | 621.4 | 0.003 | HOMO-1→LUMO+1(90%) |
| $S_8$ | 619.9 | 0.0083 | HOMO→LUMO+22(27%) HOMO-2→LUMO(14%) HOMO-2→LUMO+1(8%) HOMO→LUMO+28(5%) HOMO→LUMO+29(5%) |
| $S_9$ | 618.6 | 0.0041 | HOMO-2→LUMO+18(40%) HOMO-2→LUMO+2(34%) HOMO-2→LUMO(10%) |
| $S_{10}$ | 612.7 | 0.0019 | HOMO-2→LUMO+1(48%) HOMO-2→LUMO(48%) |
| $S_{11}$ | 603.6 | 0.0094 | HOMO→LUMO+22(38%) HOMO→LUMO+30(32%) |
| $S_{16}$ | 588 | 0.0024 | HOMO-1→LUMO+2(96%) |
| $S_{21}$ | 566.2 | 0.0031 | HOMO-2→LUMO+2(97%) |
| $S_{25}$ | 550.2 | 0.0009 | HOMO→LUMO+12(86%) HOMO→LUMO+11(6%) |
| $S_{29}$ | 541.9 | 0.0107 | HOMO-2→LUMO+22(97%) |
| $S_{31}$ | 537.5 | 0.001 | HOMO→LUMO+18(50%) HOMO→LUMO+13(30%) HOMO→LUMO+15(10%) |
| $S_{35}$ | 528.5 | 0.0008 | HOMO→LUMO+16(53%) HOMO→LUMO+22(19%) HOMO→LUMO+14(10%) HOMO→LUMO+18(9%) |
| $S_{37}$ | 523.5 | 0.0021 | HOMO→LUMO+18(55%) HOMO→LUMO+22(31%) HOMO→LUMO+17(5%) |
| $S_{40}$ | 519.6 | 0.0035 | HOMO→LUMO+28(73%) HOMO→LUMO+29(13%) HOMO→LUMO+18(6%) |
| $S_{42}$ | 496.6 | 0.0043 | HOMO→LUMO+30(55%) HOMO-2→LUMO+28(35%) |
| $S_{43}$ | 485.8 | 0.013 | HOMO→LUMO+35(80%) HOMO→LUMO+39(16%) |
| $S_{44}$ | 482.3 | 0.0013 | HOMO→LUMO+37(60%) HOMO→LUMO+38(31%) |
| $S_{45}$ | 480.3 | 0.0143 | HOMO→LUMO+39(75%) HOMO→LUMO+38(18%) |

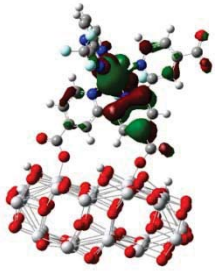

HOMO-2 (–5.75 eV)

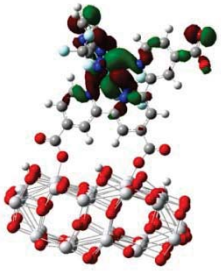

HOMO-1 (–5.65 eV)

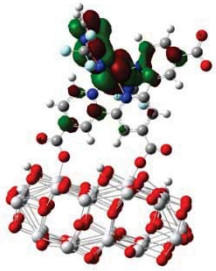

HOMO (–5.36 eV)

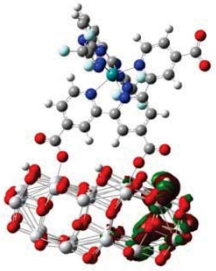

LUMO (–3.73 eV)

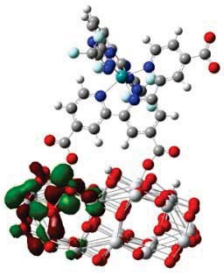

LUMO+1 (–3.55 eV)

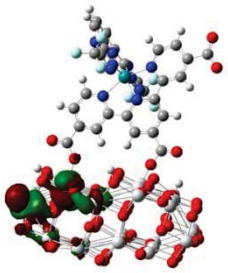

LUMO+2 (–3.43 eV)

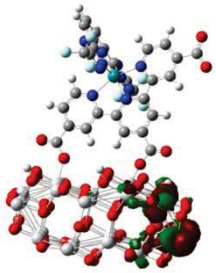

LUMO+3 (–3.38 eV)

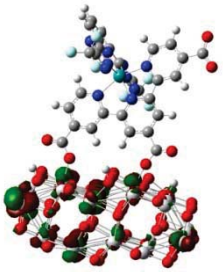

LUMO+4 (–3.30 eV)

**Figure 2.6.1** Frontier molecular orbitals pertinent to the singlet optical transitions in selected states for TF-51-Ru/$(TiO_2)_{38}$. The isovalue for the contours is 0.02 (default value in GaussView 5.0).

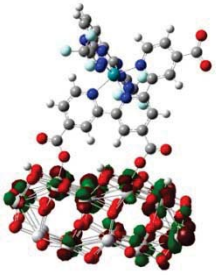

LUMO+11 (–2.97 eV)

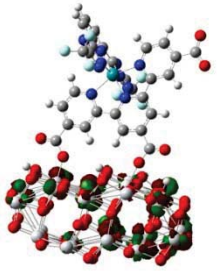

LUMO+12 (–2.95 eV)

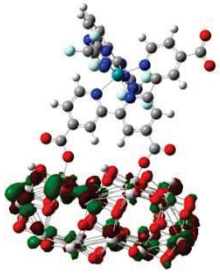

LUMO+13 (–2.92 eV)

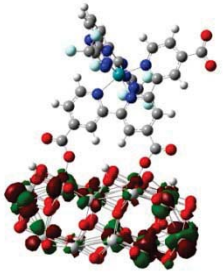

LUMO+14 (–2.91 eV)

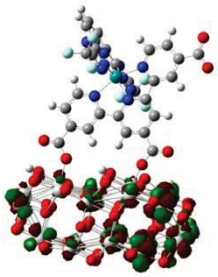

LUMO+15 (–2.89 eV)

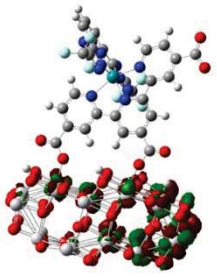

LUMO+16 (–2.87 eV)

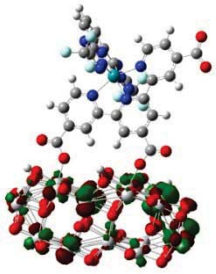

LUMO+17 (–2.84 eV)

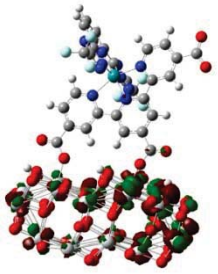

LUMO+18 (–2.82 eV)

**Figure 2.6.2** Frontier molecular orbitals pertinent to the singlet optical transitions in selected states for TF-51-Ru/$(TiO_2)_{38}$. The isovalue for the contours is 0.02 (default value in GaussView 5.0).

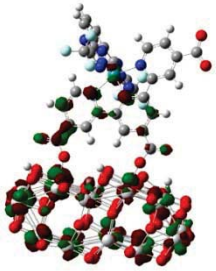

LUMO+22 (–2.76 eV)

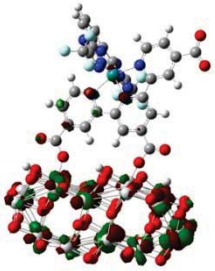

LUMO+28 (–2.63 eV)

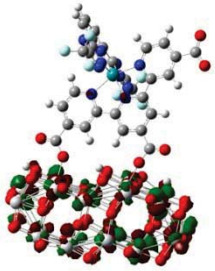

LUMO+29 (–2.62 eV)

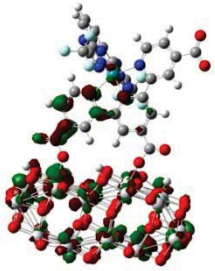

LUMO+30 (–2.60 eV)

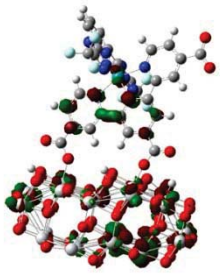

LUMO+35 (–2.48 eV)

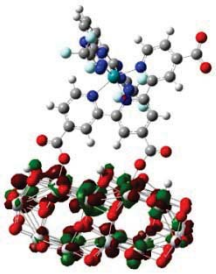

LUMO+37 (–2.47 eV)

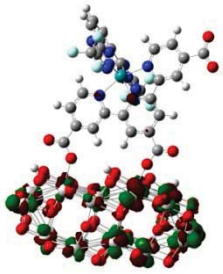

LUMO+38 (–2.45 eV)

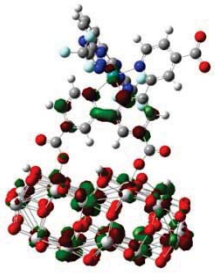

LUMO+39 (–2.44 eV)

**Figure 2.6.3** Frontier molecular orbitals pertinent to the singlet optical transitions in selected states for TF-51-Ru/$(TiO_2)_{38}$. The isovalue for the contours is 0.02 (default value in GaussView 5.0).

**Table 2.3** The wavelengths, transition probabilities and charge transfer characters of the singlet optical transitions in selected states with oscillator strength > 0.0005 for TF-52-Os/$(TiO_2)_{38}$. The lowest triplet transition ($S_0 \rightarrow T_1$) is also listed.

| State | $\lambda_{cal}$ (nm) | *f* | Assignments |
|---|---|---|---|
| $T_1$ | 885.5 | 0 | HOMO→LUMO(100%) |
| $S_1$ | 885.3 | 0.0003 | HOMO→LUMO(100%) |
| $S_2$ | 850.1 | 0.0006 | HOMO→LUMO+1(95%) |
| $S_3$ | 803.2 | 0.0094 | HOMO-2→LUMO+4(80%) HOMO-2→LUMO+2(7%) HOMO→LUMO+2(6%) |
| $S_4$ | 763.9 | 0.0005 | HOMO→LUMO+2(60%) HOMO→LUMO+3(36%) |
| $S_5$ | 750.1 | 0.0034 | HOMO-1→LUMO+4(77%) HOMO-2→LUMO(20%) |
| $S_7$ | 700.9 | 0.0006 | HOMO→LUMO+7(83%) HOMO-2→LUMO+7(8%) |
| $S_8$ | 678.4 | 0.0022 | HOMO→LUMO+8(40%) HOMO→LUMO+12(30%) HOMO→LUMO+16(12%) |
| $S_9$ | 663.1 | 0.0041 | HOMO→LUMO+9(62%) HOMO→LUMO+20(30%) HOMO→LUMO+21(6%) |
| $S_{11}$ | 644.2 | 0.0067 | HOMO→LUMO+12(64%) HOMO→LUMO+22(25%) |
| $S_{13}$ | 613.1 | 0.0082 | HOMO→LUMO+15(70%) HOMO→LUMO+9(18%) HOMO→LUMO+8(9%) |
| $S_{14}$ | 599 | 0.0043 | HOMO-2→LUMO+9(68%) HOMO→LUMO+8(14%) |
| $S_{15}$ | 580.1 | 0.0094 | HOMO→LUMO+15(84%) HOMO-2→LUMO+8(10%) |
| $S_{20}$ | 552.1 | 0.0044 | HOMO→LUMO+15(63%) HOMO→LUMO+26(21%) |
| $S_{23}$ | 536.9 | 0.0109 | HOMO→LUMO+34(67%) HOMO→LUMO+37(6%) HOMO→LUMO+36(5%) HOMO→LUMO+17(5%) |
| $S_{26}$ | 525.9 | 0.0016 | HOMO→LUMO+32(44%) HOMO→LUMO+35(39%) |
| $S_{28}$ | 519.4 | 0.0009 | HOMO→LUMO+17(59%) HOMO→LUMO+16(26%) |
| $S_{29}$ | 516.1 | 0.0036 | HOMO→LUMO+36(42%) HOMO→LUMO+35(20%) HOMO→LUMO+37(18%) HOMO→LUMO+20(15%) |
| $S_{30}$ | 514.8 | 0.0008 | HOMO→LUMO+26(78%) HOMO→LUMO+21(6%) HOMO→LUMO+12(6%) HOMO→LUMO+17(5%) |
| $S_{36}$ | 499.1 | 0.0051 | HOMO-1→LUMO+36(75%) HOMO→LUMO+34(20%) |
| $S_{39}$ | 472.4 | 0.0133 | HOMO→LUMO+37(82%) HOMO→LUMO+36(15%) |
| $S_{40}$ | 468.9 | 0.0009 | HOMO→LUMO+21(54%) HOMO→LUMO+20(39%) |
| $S_{46}$ | 443.6 | 0.0033 | HOMO→LUMO+37(44%) HOMO→LUMO+35(28%) |

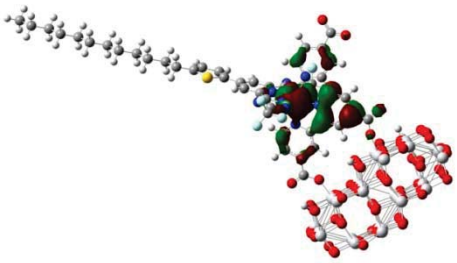

HOMO-2 (–5.73 eV)

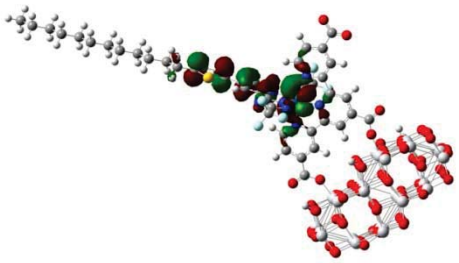

HOMO-1 (–5.46 eV)

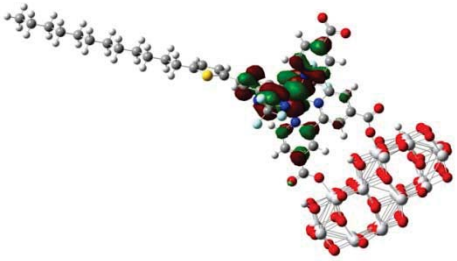

HOMO (–5.29 eV)

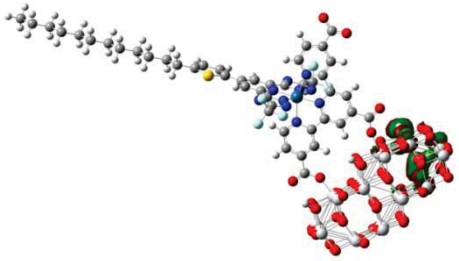

LUMO (–3.89 eV)

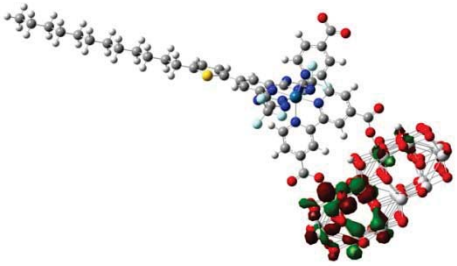

LUMO+1 (–3.16 eV)

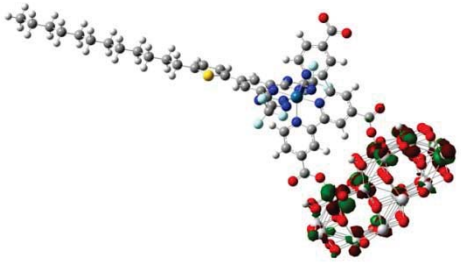

LUMO+2 (–3.11 eV)

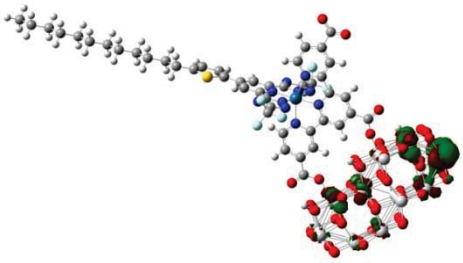

LUMO+3 (–3.05 eV)

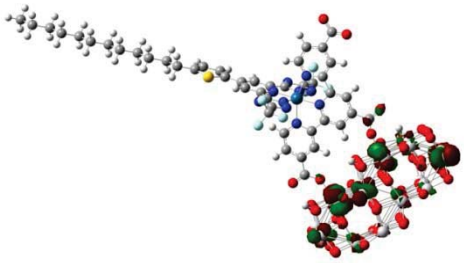

LUMO+4 (–2.93 eV)

**Figure 2.7.1** Frontier molecular orbitals pertinent to the singlet optical transitions in selected states for TF-52-Os/$(TiO_2)_{38}$. The isovalue for the contours is 0.02 (default value in GaussView 5.0).

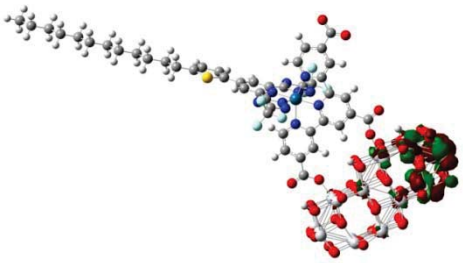

LUMO+7 (–2.80 eV)

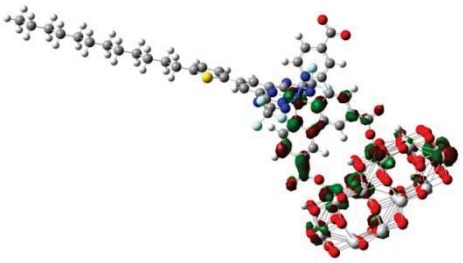

LUMO+8 (–2.76 eV)

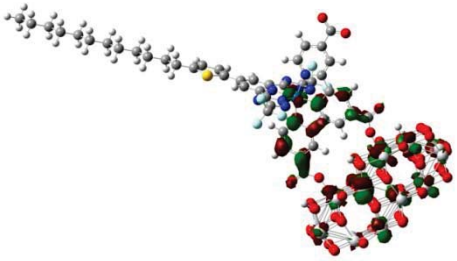

LUMO+9 (–2.72 eV)

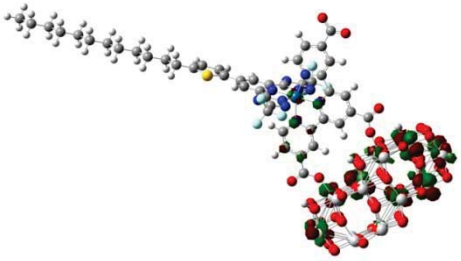

LUMO+12 (–2.63 eV)

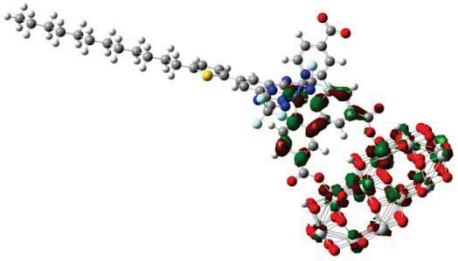

LUMO+15 (–2.59 eV)

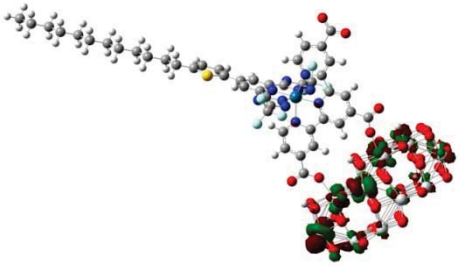

LUMO+16 (–2.55 eV)

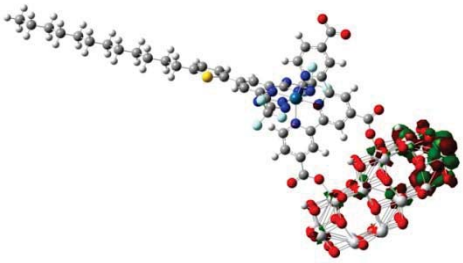

LUMO+17 (–2.53 eV)

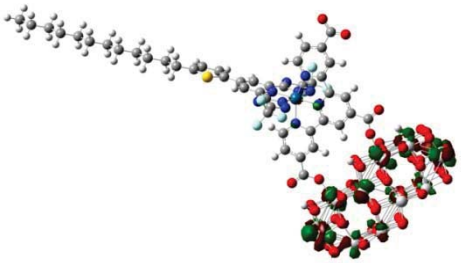

LUMO+20 (–2.47 eV)

**Figure 2.7.2** Frontier molecular orbitals pertinent to the singlet optical transitions in selected states for TF-52-Os/$(TiO_2)_{38}$. The isovalue for the contours is 0.02 (default value in GaussView 5.0).

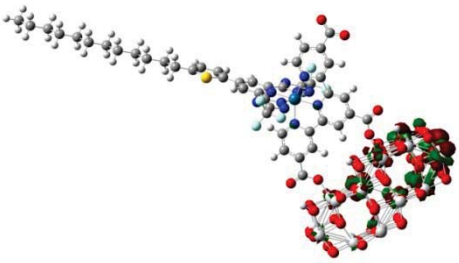

LUMO+21 (–2.44 eV)

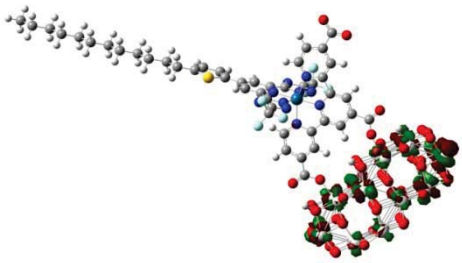

LUMO+26 (–2.38 eV)

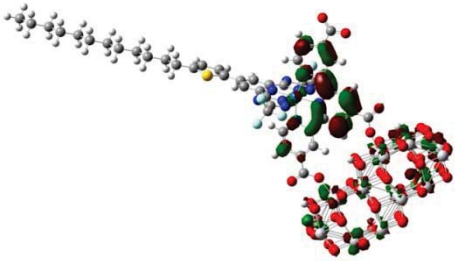

LUMO+34 (–2.25 eV)

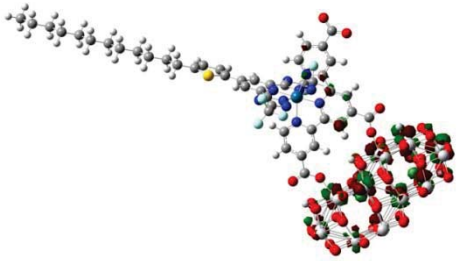

LUMO+35 (–2.24 eV)

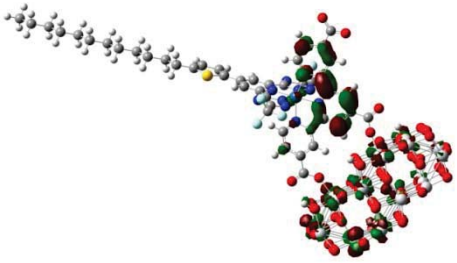

LUMO+36 (–2.24 eV)

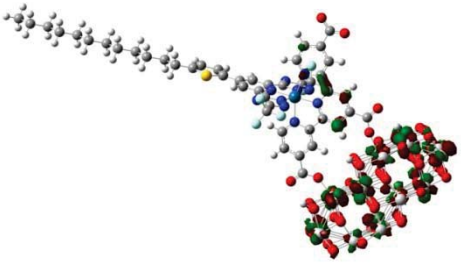

LUMO+37 (–2.22 eV)

**Figure 2.7.3** Frontier molecular orbitals pertinent to the singlet optical transitions in selected states for TF-52-Os/$(TiO_2)_{38}$. The isovalue for the contours is 0.02 (default value in GaussView 5.0).

**Table 2.4** The wavelengths, transition probabilities and charge transfer characters of the singlet optical transitions in selected states with oscillator strength > 0.0004 for TF-52-Ru/$(TiO_2)_{38}$. The lowest triplet transition ($S_0 \rightarrow T_1$) is also listed.

| State | $\lambda_{cal}$ (nm) | *f* | Assignments |
|---|---|---|---|
| $T_1$ | 756.1 | 0 | HOMO→LUMO(100%) |
| $S_1$ | 755.9 | 0.0003 | HOMO→LUMO (100%) |
| $S_2$ | 722.9 | 0.0011 | HOMO→LUMO+3(65%) HOMO→LUMO+1 (30%) |
| $S_3$ | 669.9 | 0.0094 | HOMO→LUMO+3(99%) |
| $S_7$ | 625 | 0.0013 | HOMO→LUMO+4(84%) |
| $S_{10}$ | 608.2 | 0.0067 | HOMO-1→LUMO+3(66%) HOMO→LUMO+7(31%) |
| $S_{11}$ | 606 | 0.0029 | HOMO-2→LUMO+3(74%) HOMO→LUMO+8(20%) |
| $S_{13}$ | 595.8 | 0.0018 | HOMO-2→LUMO(98%) |
| $S_{14}$ | 588.2 | 0.0049 | HOMO→LUMO+15(73%) HOMO→LUMO+16(13%) |
| $S_{21}$ | 558 | 0.0025 | HOMO→LUMO+20 (62%) HOMO→LUMO+22(13%)<br>HOMO→LUMO+25(11%) HOMO→LUMO+26(6%) |
| $S_{22}$ | 551.6 | 0.0105 | HOMO→LUMO+29(38%) HOMO→LUMO+28(36%) |
| $S_{23}$ | 550.8 | 0.0007 | HOMO→LUMO+3(51%) HOMO→LUMO+2(46%) |
| $S_{29}$ | 540 | 0.0032 | HOMO→LUMO+11(66%) HOMO→LUMO+10(28%) |
| $S_{31}$ | 532 | 0.0008 | HOMO→LUMO+22 (55%) HOMO→LUMO+16(43%) |
| $S_{32}$ | 530.9 | 0.0004 | HOMO→LUMO+17 (46%) HOMO→LUMO+18(25%) |
| $S_{34}$ | 527.4 | 0.0034 | HOMO→LUMO+29 (64%) HOMO→LUMO+35(15%)<br>HOMO→LUMO+36 (6%) HOMO→LUMO+39(5%) |
| $S_{35}$ | 525.8 | 0.0007 | HOMO→LUMO+21 (68%) HOMO→LUMO+23(31%) |
| $S_{37}$ | 520.4 | 0.0014 | HOMO-2→LUMO+29 (61%) HOMO→LUMO+28(31%) |
| $S_{39}$ | 510.3 | 0.0004 | HOMO→LUMO+30 (46%) HOMO→LUMO+31(25%) |
| $S_{40}$ | 505.1 | 0.0045 | HOMO→LUMO+33 (59%) HOMO→LUMO+39(38%) |
| $S_{42}$ | 500 | 0.0005 | HOMO→LUMO+30 (59%) HOMO→LUMO+37(25%) |
| $S_{43}$ | 497.2 | 0.0087 | HOMO-2→LUMO+33 (77%) HOMO→LUMO+29(6%)<br>HOMO-1→LUMO+28 (6%) HOMO→LUMO+22(5%) |
| $S_{44}$ | 488.8 | 0.0025 | HOMO→LUMO+29 (69%) HOMO→LUMO+36(18%) |
| $S_{45}$ | 484.1 | 0.0125 | HOMO→LUMO+33 (74%) HOMO→LUMO+29(10%)<br>HOMO→LUMO+15 (6%) HOMO→LUMO+25(5%) |
| $S_{46}$ | 479.3 | 0.0005 | HOMO→LUMO+31 (93%) HOMO→LUMO+24(5%) |
| $S_{47}$ | 468.2 | 0.0007 | HOMO→LUMO+32 (80%) HOMO→LUMO+28(17%) |

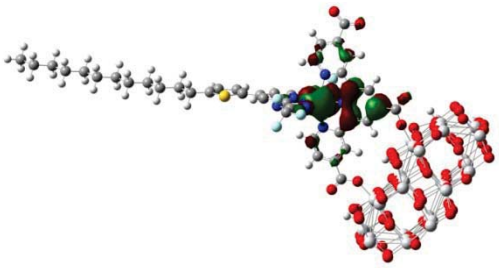

HOMO-2 (–5.67 eV)

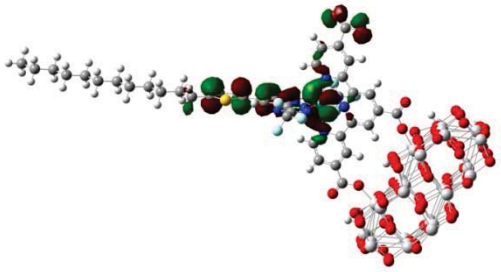

HOMO-1 (–5.60 eV)

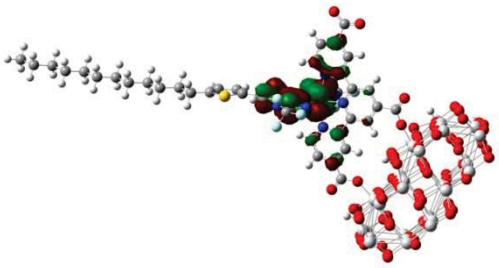

HOMO (–5.38 eV)

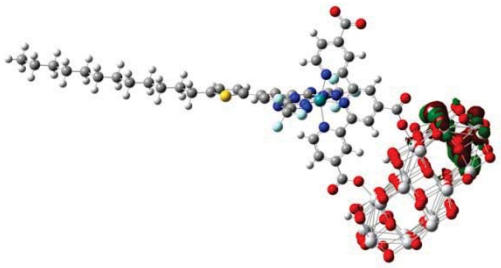

LUMO (–3.74 eV)

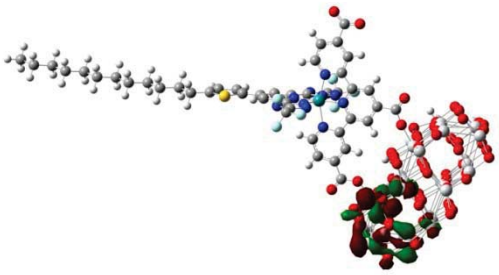

LUMO+1 (–3.46 eV)

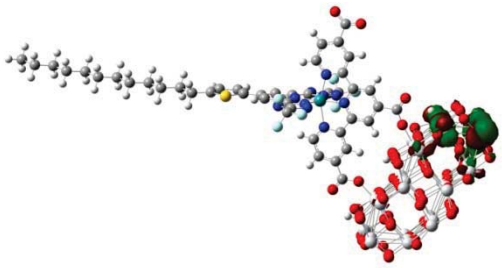

LUMO+2 (–3.37 eV)

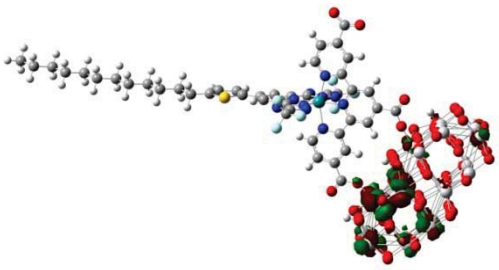

LUMO+3 (–3.30 eV)

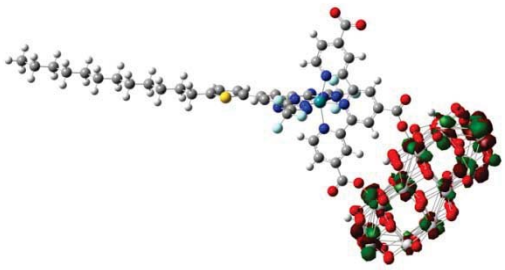

LUMO+7 (–3.05 eV)

**Figure 2.8.1** Frontier molecular orbitals pertinent to the singlet optical transitions in selected states for TF-52-Ru/$(TiO_2)_{38}$. The isovalue for the contours is 0.02 (default value in GaussView 5.0).

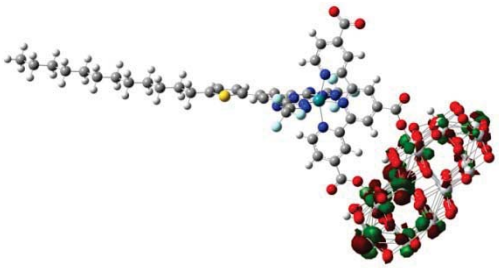

LUMO+8 (–3.04 eV)

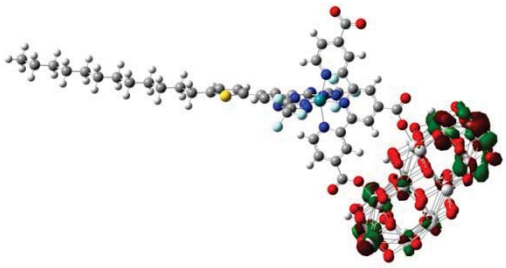

LUMO+10 (–2.96 eV)

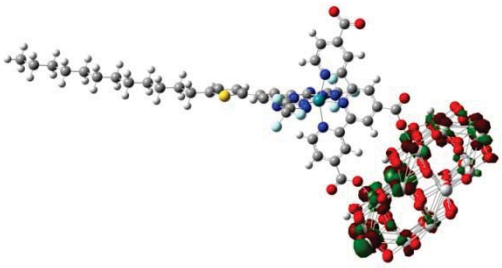

LUMO+11 (–2.94 eV)

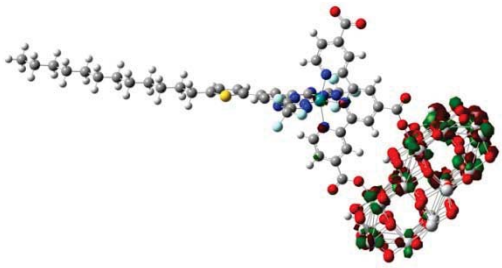

LUMO+15 (–2.85 eV)

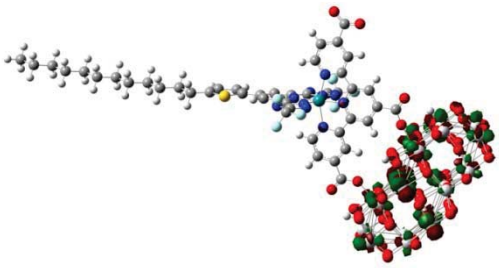

LUMO+16 (–2.81 eV)

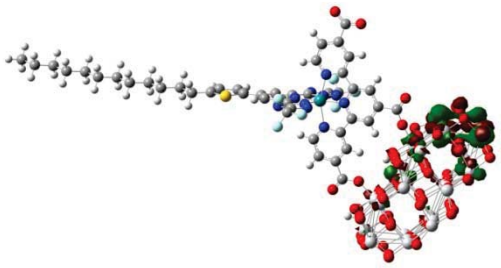

LUMO+17 (–2.81 eV)

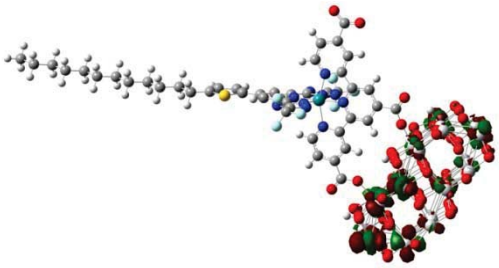

LUMO+18 (–2.79 eV)

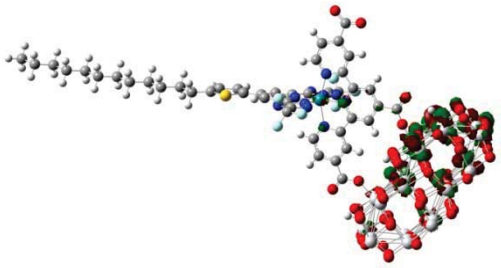

LUMO+20 (–2.76 eV)

**Figure 2.8.2** Frontier molecular orbitals pertinent to the singlet optical transitions in selected states for TF-52-Ru/$(TiO_2)_{38}$. The isovalue for the contours is 0.02 (default value in GaussView 5.0).

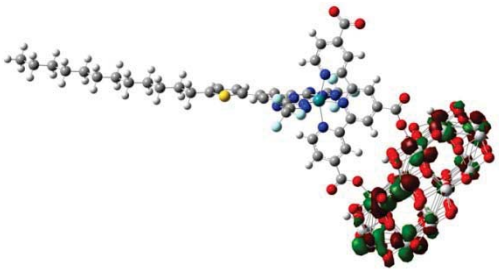

LUMO+21 (–2.72 eV)

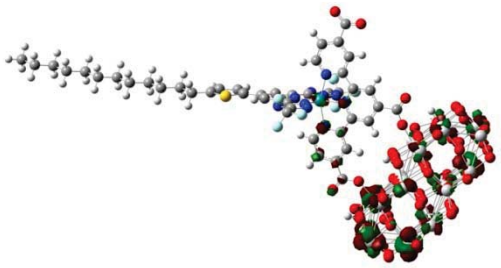

LUMO+22 (–2.71 eV)

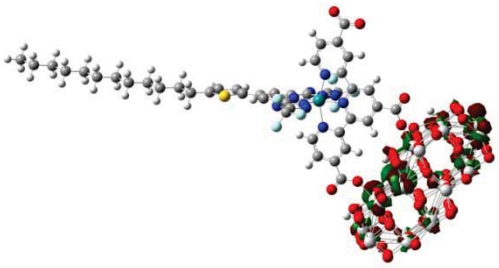

LUMO+23 (–2.70 eV)

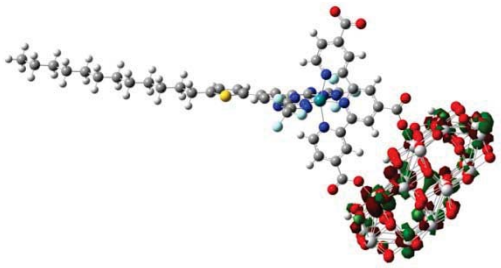

LUMO+24 (–2.67 eV)

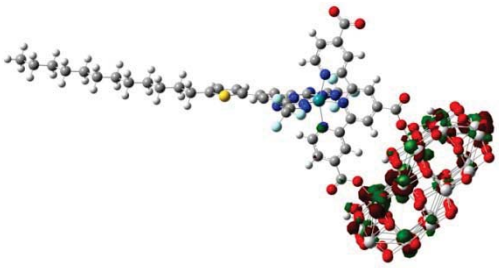

LUMO+25 (–2.66 eV)

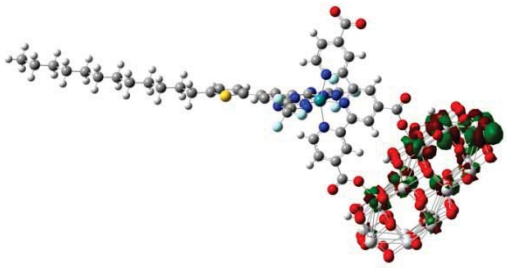

LUMO+26 (–2.64 eV)

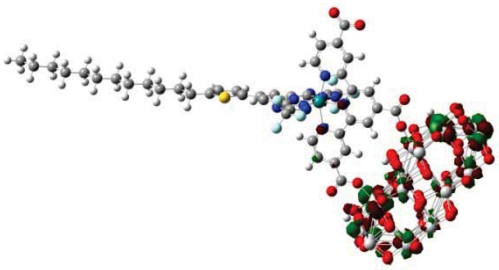

LUMO+28 (–2.60 eV)

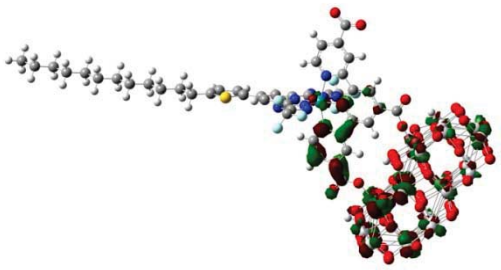

LUMO+29 (–2.59 eV)

**Figure 2.8.3** Frontier molecular orbitals pertinent to the singlet optical transitions in selected states for TF-52-Ru/$(TiO_2)_{38}$. The isovalue for the contours is 0.02 (default value in GaussView 5.0).

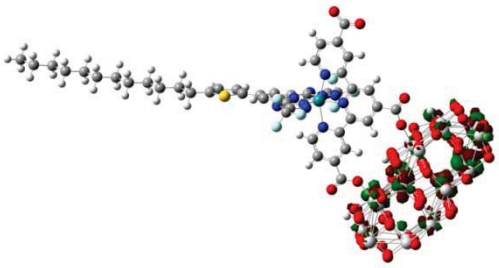

LUMO+30 (–2.56 eV)

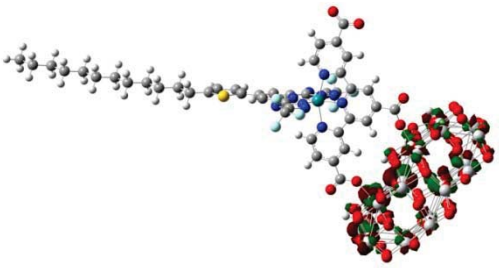

LUMO+31 (–2.54 eV)

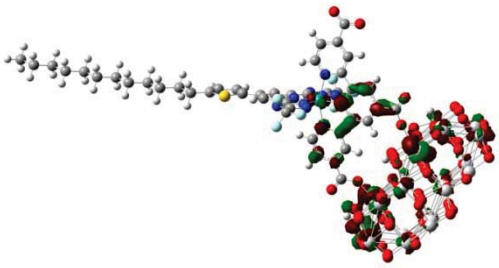

LUMO+33 (–2.52 eV)

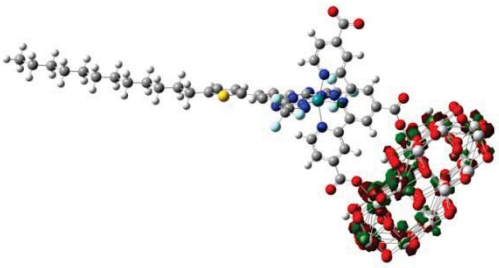

LUMO+35 (–2.46 eV)

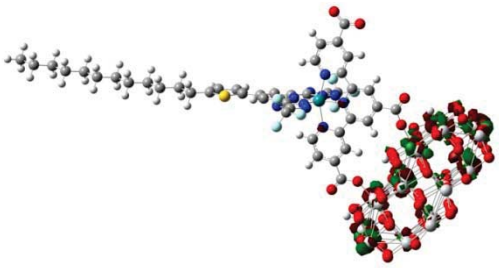

LUMO+36 (–2.45 eV)

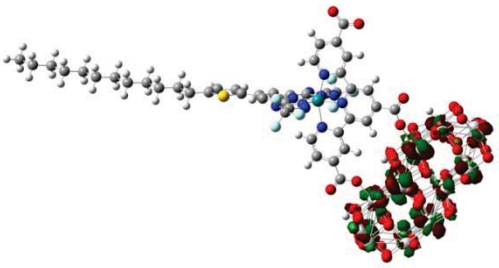

LUMO+37 (–2.44 eV)

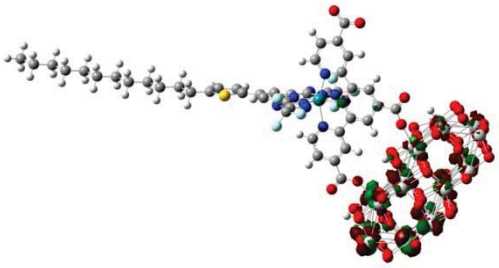

LUMO+39 (–2.40 eV)

**Figure 2.8.4** Frontier molecular orbitals pertinent to the singlet optical transitions in selected states for TF-52-Ru/$(TiO_2)_{38}$. The isovalue for the contours is 0.02 (default value in GaussView 5.0).

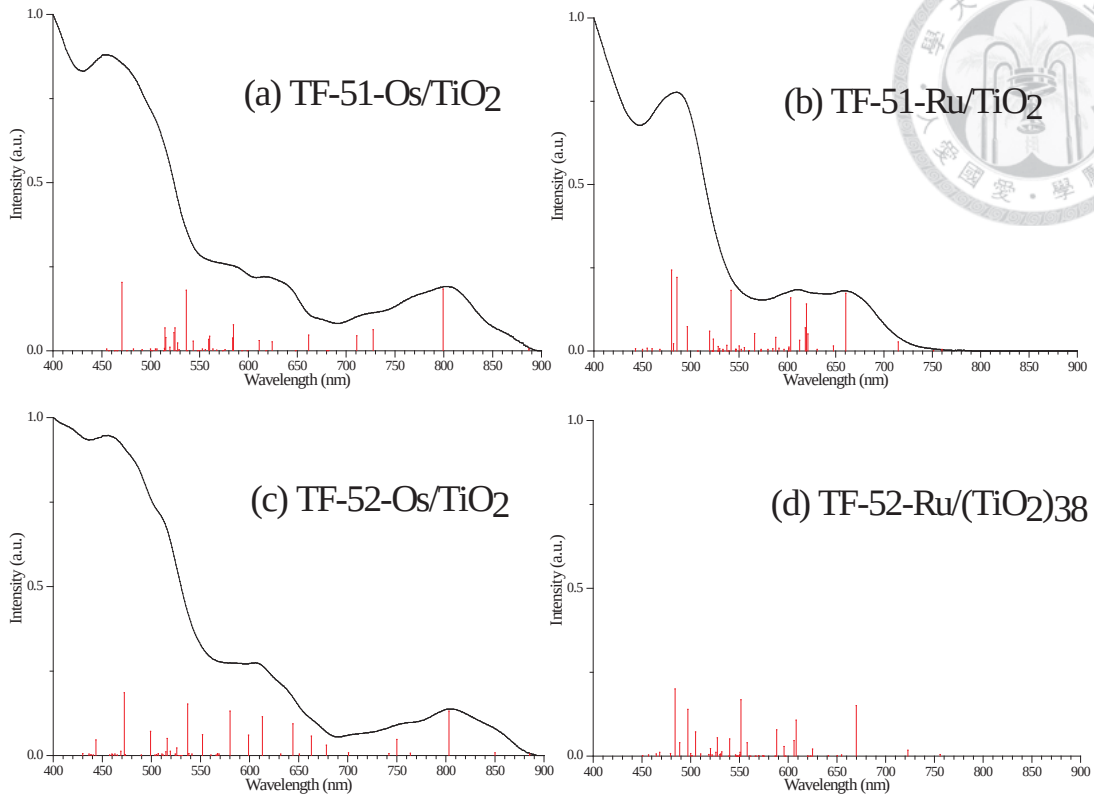


**Figure 2.9** The experimental spectra and calculated oscillator strengths of (a) TF-51-Os/$(TiO_2)_{38}$, (b) TF-51-Ru/$(TiO_2)_{38}$, (c) TF-52-Os/$(TiO_2)_{38}$, and (d) TF-52-Ru/$(TiO_2)_{38}$ in DMF. The red vertical lines at the bottom of the graphs represent the relative oscillator strengths.

(a-1) HOMO of TF-51-Os/$(TiO_2)_{38}$

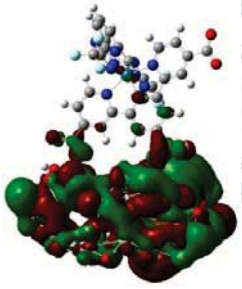

(a-2) LUMO of TF-51-Os/$(TiO_2)_{38}$

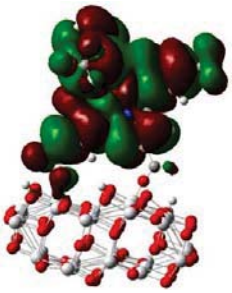

(b-1) HOMO of TF-51-Ru/$(TiO_2)_{38}$

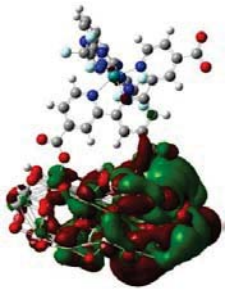

(b-2) LUMO of TF-51-Ru/$(TiO_2)_{38}$

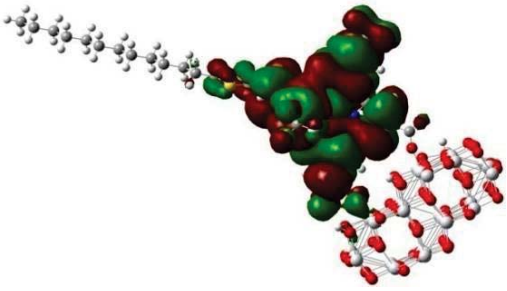

(c-1) HOMO of TF-52-Os/$(TiO_2)_{38}$

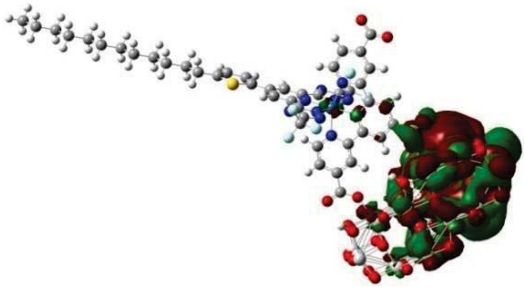

(c-2) LUMO of TF-52-Os/$(TiO_2)_{38}$

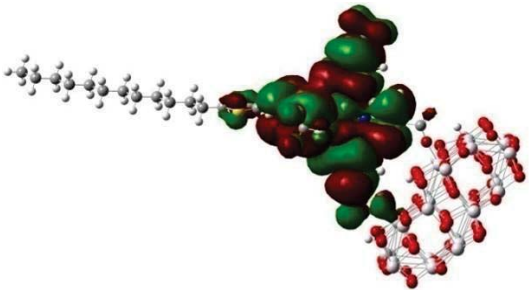

(d-1) HOMO of TF-52-Ru/$(TiO_2)_{38}$

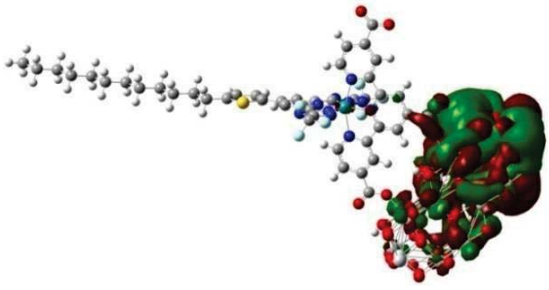

(d-2) LUMO of TF-52-Ru/$(TiO_2)_{38}$

**Figure 2.10** HOMO and LUMO of (a) TF-51-Os/$(TiO_2)_{38}$, (b) TF-51-Ru/$(TiO_2)_{38}$, (c) TF-52-Os/$(TiO_2)_{38}$, and (d) TF-52-Ru/$(TiO_2)_{38}$ models. The isovalue for the contours is 0.002.

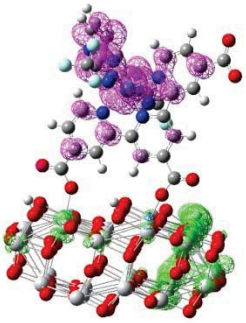

(a-1) HOMO → LUMO ($S_0 \rightarrow S_1$) (isovalue = 0.02) of TF-51-Os/$(TiO_2)_{38}$

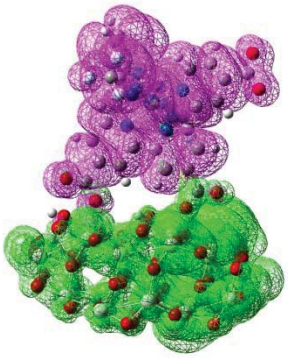

(a-2) HOMO → LUMO ($S_0 \rightarrow S_1$) (isovalue = 0.002) of TF-51-Os/$(TiO_2)_{38}$

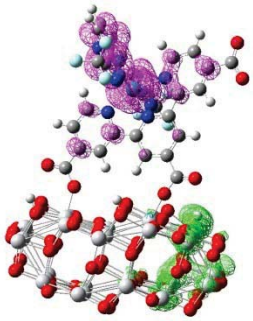

(b-1) HOMO → LUMO ($S_0 \rightarrow S_1$) (isovalue = 0.02) of TF-51-Ru/$(TiO_2)_{38}$

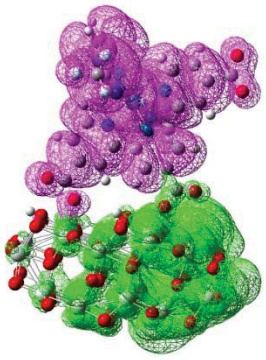

(b-2) HOMO → LUMO ($S_0 \rightarrow S_1$) (isovalue = 0.002) of TF-51-Ru/$(TiO_2)_{38}$

**Figure 2.11.1** The lowest singlet optical transition of (a) TF-51-Os/$(TiO_2)_{38}$ and (b) TF-51-Ru/$(TiO_2)_{38}$ models. Pink mesh indicates the decrease of charge density, while green mesh indicates the increase of charge density upon photoexcitation. The isovalue for the contours is 0.02 (left column) and 0.002 (right column), respectively.

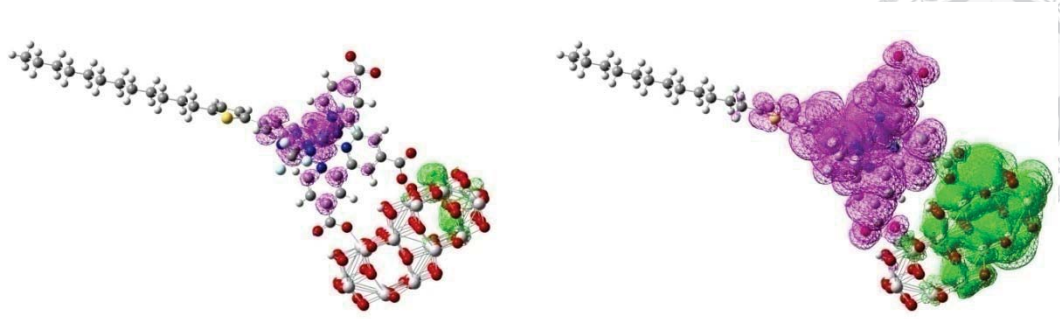

(c-1) HOMO → LUMO ($S_0 \rightarrow S_1$) (isovalue = 0.02) of TF-52-Os/$(TiO_2)_{38}$

(c-2) HOMO → LUMO ($S_0 \rightarrow S_1$) (isovalue = 0.002) of TF-52-Os/$(TiO_2)_{38}$

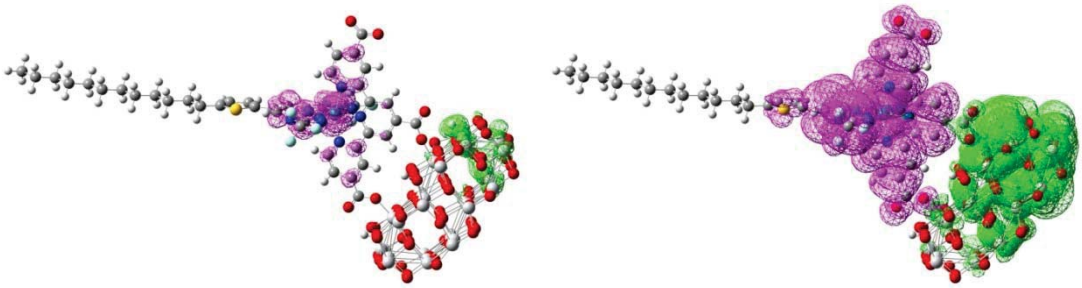

(d-1) HOMO → LUMO ($S_0 \rightarrow S_1$) (isovalue = 0.02) of TF-52-Ru/$(TiO_2)_{38}$

(d-2) HOMO → LUMO ($S_0 \rightarrow S_1$) (isovalue = 0.002) of TF-52-Ru/$(TiO_2)_{38}$

**Figure 2.11.2** The lowest singlet optical transition of (c) TF-52-Os/$(TiO_2)_{38}$ and (d) TF-52-Ru/$(TiO_2)_{38}$ models. Pink mesh indicates the decrease of charge density, while green mesh indicates the increase of charge density upon photoexcitation. The isovalue for the contours is 0.02 (left column) and 0.002 (right column), respectively.

**Table 2.5** Electron contributions (%) in molecular fragments and molecular orbitals of the four dye/$(TiO_2)_{38}$ models.

| TF-51-Os /$(TiO_2)_{38}$ | Os | terpyridine | 2 anchored $COO^-$ | 6 F | thiophene | $(TiO_2)_{38}$ | 3 anchored $H^+$ |
|---|---|---|---|---|---|---|---|
| HOMO | 52.86 | 13.42 | 0.58 | 0.64 | – | 0.25 | 0 |
| LUMO | 0.01 | 0.04 | 0.19 | 0 | – | 99.67 | 0.05 |
| TF-51-Ru /$(TiO_2)_{38}$ | Ru | terpyridine | 2 anchored $COO^-$ | 6 F | thiophene | $(TiO_2)_{38}$ | 3 anchored $H^+$ |
| HOMO | 58.76 | 10.19 | 0.39 | 0.61 | – | 0.03 | 0 |
| LUMO | 0.01 | 0.02 | 0.06 | 0 | – | 99.83 | 0.05 |
| TF-52-Os /$(TiO_2)_{38}$ | Os | terpyridine | 2 anchored $COO^-$ | 6 F | thiophene | $(TiO_2)_{38}$ | 3 anchored $H^+$ |
| HOMO | 54.32 | 14.73 | 0.59 | 0.59 | 0.17 | 0.04 | 0 |
| LUMO | 0.02 | 0.02 | 0.1 | 0 | 0 | 99.57 | 0.06 |
| TF-52-Ru /$(TiO_2)_{38}$ | Ru | terpyridine | 2 anchored $COO^-$ | 6 F | thiophene | $(TiO_2)_{38}$ | 3 anchored $H^+$ |
| HOMO | 59.41 | 10.63 | 0.43 | 0.59 | 0.08 | 0.05 | 0 |
| LUMO | 0.01 | 0.02 | 0.07 | 0 | 0 | 99.81 | 0.05 |

**Table 2.6** Electron contributions (%) in molecular fragments and molecular orbitals relavent to the singlet optical transitions in Table 2.1 for TF-51-Os/$(TiO_2)_{38}$.

| Molecular Orbital | Os | terpyridine | 2 anchored $COO^-$ | 6 F | $(TiO_2)_{38}$ | 3 anchored $H^+$ |
|---|---|---|---|---|---|---|
| HOMO-2 | 62.99 | 26.62 | 1.99 | 0.1 | 0.23 | 0 |
| HOMO-1 | 65.93 | 8.33 | 0.04 | 0.02 | 0.02 | 0 |
| HOMO | 52.86 | 13.42 | 0.58 | 0.64 | 0.25 | 0 |
| LUMO | 0.01 | 0.04 | 0.19 | 0 | 99.67 | 0.05 |
| LUMO+1 | 0.09 | 0.41 | 1.18 | 0 | 98.24 | 0.03 |
| LUMO+2 | 0 | 0 | 0 | 0 | 99.51 | 0.37 |
| LUMO+3 | 0.11 | 0.39 | 0.5 | 0 | 98.95 | 0.01 |
| LUMO+4 | 0.04 | 0.15 | 0.16 | 0 | 99.62 | 0.02 |
| LUMO+5 | 0.06 | 0.27 | 0.48 | 0 | 99.1 | 0.08 |
| LUMO+6 | 0.03 | 0.43 | 1.07 | 0 | 98.45 | 0.02 |
| LUMO+8 | 0.43 | 2.23 | 0.9 | 0 | 96.37 | 0.01 |
| LUMO+12 | 1.05 | 6.11 | 1.27 | 0 | 91.36 | 0 |
| LUMO+14 | 1.09 | 6.47 | 1.2 | 0 | 91 | 0.02 |
| LUMO+15 | 2.19 | 13.49 | 2.15 | 0 | 81.68 | 0.07 |
| LUMO+16 | 0.13 | 0.89 | 1.18 | 0 | 97.78 | 0 |
| LUMO+17 | 0.01 | 0.23 | 0.34 | 0 | 99.37 | 0 |
| LUMO+18 | 0 | 0 | 0 | 0 | 99.98 | 0.02 |
| LUMO+19 | 1.25 | 9.91 | 1.59 | 0 | 87 | 0.03 |
| LUMO+20 | 1.13 | 7.2 | 0.68 | 0 | 90.83 | 0.02 |
| LUMO+21 | 0.54 | 3.29 | 0.48 | 0 | 95.6 | 0.02 |
| LUMO+40 | 0.72 | 16.07 | 0.93 | 0 | 81.9 | 0.04 |

**Table 2.7** Electron contributions (%) of molecular fragments and molecular orbitals relavent to the singlet optical transitions in Table 2.2 for TF-51-Ru/$(TiO_2)_{38}$.

| Molecular Orbital | Ru | terpyridine | 2 anchored $COO^-$ | 6 F | $(TiO_2)_{38}$ | 3 anchored $H^+$ |
|---|---|---|---|---|---|---|
| HOMO-2 | 70.11 | 19.66 | 1.37 | 0.08 | 0.14 | 0 |
| HOMO-1 | 70.63 | 9.75 | 0.11 | 0.02 | 0.02 | 0 |
| HOMO | 58.76 | 10.19 | 0.39 | 0.61 | 0.03 | 0 |
| LUMO | 0.01 | 0.02 | 0.06 | 0 | 99.83 | 0.05 |
| LUMO+1 | 0 | 0 | 0 | 0 | 99.6 | 0.34 |
| LUMO+2 | 0.03 | 0.16 | 0.65 | 0 | 99.1 | 0.04 |
| LUMO+3 | 0.01 | 0.03 | 0.09 | 0 | 99.78 | 0.01 |
| LUMO+4 | 0.06 | 0.24 | 0.5 | 0 | 99.13 | 0.01 |
| LUMO+11 | 0.02 | 0.12 | 0.17 | 0 | 99.67 | 0.02 |
| LUMO+12 | 0 | 0 | 0.02 | 0 | 99.96 | 0.01 |
| LUMO+13 | 0 | 0 | 0.04 | 0 | 99.91 | 0.05 |
| LUMO+14 | 0.14 | 0.9 | 0.55 | 0 | 98.35 | 0.01 |
| LUMO+15 | 0.05 | 0.33 | 0.17 | 0 | 99.41 | 0.02 |
| LUMO+16 | 0.14 | 0.93 | 0.41 | 0 | 98.46 | 0.01 |
| LUMO+17 | 0.02 | 0.15 | 0.17 | 0 | 99.65 | 0 |
| LUMO+18 | 0.16 | 1.01 | 0.77 | 0 | 98.05 | 0.01 |
| LUMO+22 | 1.01 | 7.71 | 2.5 | 0 | 88.53 | 0.07 |
| LUMO+28 | 0.56 | 4.81 | 1.03 | 0 | 93.42 | 0.03 |
| LUMO+29 | 0.28 | 2.32 | 0.43 | 0 | 96.99 | 0.01 |
| LUMO+30 | 0.92 | 9.01 | 1.93 | 0 | 87.93 | 0.02 |
| LUMO+35 | 1.06 | 9.89 | 1.02 | 0 | 87.82 | 0 |
| LUMO+37 | 0.22 | 1.96 | 0.3 | 0 | 97.42 | 0.06 |
| LUMO+38 | 0.35 | 3.15 | 0.4 | 0 | 96.05 | 0 |
| LUMO+39 | 1.1 | 10.32 | 1.13 | 0 | 87.18 | 0.03 |

**Table 2.8** Electron contribution (%) of molecular fragments and molecular orbitals relavent to the singlet optical transitions in Table 2.3 for TF-52-Os/$(TiO_2)_{38}$.

| Molecular Orbital | Os | terpyridine | 2 anchored $COO^-$ | 6 F | thiophene | $-C_{12}H_{25}$ | $(TiO_2)_{38}$ | 3 anchored $H^+$ |
|---|---|---|---|---|---|---|---|---|
| HOMO-2 | 61.6 | 28.06 | 2.09 | 0.1 | 0 | 0 | 0.17 | 0 |
| HOMO-1 | 53.96 | 6.76 | 0.02 | 0.02 | 19.31 | 1.06 | 0.08 | 0 |
| HOMO | 54.32 | 14.73 | 0.59 | 0.59 | 0.17 | 0 | 0.04 | 0 |
| LUMO | 0.02 | 0.02 | 0.1 | 0 | 0 | 0 | 99.57 | 0.06 |
| LUMO+1 | 0.09 | 0.28 | 0.36 | 0 | 0 | 0 | 93.2 | 0.31 |
| LUMO+2 | 0.26 | 0.84 | 0.95 | 0 | 0 | 0 | 97.78 | 0.11 |
| LUMO+3 | 0.07 | 0.32 | 0.45 | 0 | 0 | 0 | 99.15 | 0.01 |
| LUMO+4 | 0.19 | 1.05 | 2.22 | 0 | 0 | 0 | 96.16 | 0.01 |
| LUMO+7 | 0.03 | 0.11 | 0.18 | 0 | 0 | 0 | 97.5 | 0 |
| LUMO+8 | 2.34 | 11.87 | 2.98 | 0 | 0 | 0 | 82.34 | 0 |
| LUMO+9 | 2.89 | 15.17 | 3.08 | 0 | 0 | 0 | 78.45 | 0.01 |
| LUMO+12 | 0.89 | 5.47 | 0.84 | 0 | 0 | 0 | 92.8 | 0 |
| LUMO+15 | 2.97 | 16.92 | 2.16 | 0 | 0 | 0 | 76.99 | 0.02 |
| LUMO+16 | 0.37 | 2.38 | 0.44 | 0 | 0 | 0 | 94.72 | 0.04 |
| LUMO+17 | 0.48 | 2.87 | 0.28 | 0 | 0 | 0 | 93.54 | 0.01 |
| LUMO+20 | 0.55 | 3.42 | 0.38 | 0 | 0 | 0 | 95.45 | 0.03 |
| LUMO+21 | 0.33 | 2.49 | 0.23 | 0 | 0 | 0 | 86.45 | 0.01 |
| LUMO+26 | 0.16 | 1.8 | 0.58 | 0 | 0 | 0 | 97.41 | 0.05 |
| LUMO+34 | 1.51 | 32.17 | 1.62 | 0 | 0.02 | 0 | 64.28 | 0.03 |
| LUMO+35 | 0.28 | 5.81 | 0.3 | 0 | 0 | 0 | 89.18 | 0.04 |
| LUMO+36 | 1.14 | 24.82 | 0.5 | 0 | 0.02 | 0 | 72.64 | 0 |
| LUMO+37 | 0.27 | 7.8 | 0.25 | 0 | 0.02 | 0 | 88.39 | 0.1 |

**Table 2.9** Electron contribution (%) of molecular fragments and molecular orbitals relavent to the singlet optical transitions in Table 2.4 for TF-52-Ru/$(TiO_2)_{38}$.

| Molecular Orbital | Ru | terpyridine | 2 anchored $COO^-$ | 6 F | thiophene | $-C_{12}H_{25}$ | $(TiO_2)_{38}$ | 3 anchored $H^+$ |
|---|---|---|---|---|---|---|---|---|
| HOMO-2 | 69.26 | 20.75 | 1.48 | 0.09 | 0.14 | 0 | 0.16 | 0 |
| HOMO-1 | 50.71 | 5.9 | 0.02 | 0 | 18.43 | 0.24 | 0.01 | 0 |
| HOMO | 59.41 | 10.63 | 0.43 | 0.59 | 0.08 | 0 | 0.05 | 0 |
| LUMO | 0.01 | 0.02 | 0.07 | 0 | 0 | 0 | 99.81 | 0.05 |
| LUMO+1 | 0 | 0 | 0.01 | 0 | 0 | 0 | 99.56 | 0.35 |
| LUMO+2 | 0.01 | 0.03 | 0.07 | 0 | 0 | 0 | 99.83 | 0.01 |
| LUMO+3 | 0.11 | 0.5 | 1.02 | 0 | 0 | 0 | 98.29 | 0.01 |
| LUMO+7 | 0.02 | 0.22 | 0.7 | 0 | 0 | 0 | 99.05 | 0.01 |
| LUMO+8 | 0.06 | 0.39 | 0.33 | 0 | 0 | 0 | 99.22 | 0 |
| LUMO+10 | 0.01 | 0.04 | 0.07 | 0 | 0 | 0 | 99.86 | 0.01 |
| LUMO+15 | 0.55 | 3.6 | 1.36 | 0 | 0 | 0 | 94.42 | 0 |
| LUMO+16 | 0.37 | 2.49 | 0.88 | 0 | 0 | 0 | 96.1 | 0.03 |
| LUMO+17 | 0.17 | 1.02 | 0.49 | 0 | 0 | 0 | 98.3 | 0.02 |
| LUMO+18 | 0.02 | 0.29 | 0.39 | 0 | 0 | 0 | 99.22 | 0.04 |
| LUMO+20 | 0.64 | 4.18 | 1.25 | 0 | 0 | 0 | 93.76 | 0.02 |
| LUMO+21 | 0.13 | 1.04 | 0.3 | 0 | 0 | 0 | 98.52 | 0.01 |
| LUMO+22 | 0.7 | 5.54 | 1.3 | 0 | 0 | 0 | 92.28 | 0.06 |
| LUMO+23 | 0.11 | 0.74 | 0.22 | 0 | 0 | 0 | 98.86 | 0.01 |
| LUMO+24 | 0.03 | 0.16 | 0.1 | 0 | 0 | 0 | 99.63 | 0.01 |
| LUMO+25 | 0.33 | 2.94 | 0.82 | 0 | 0 | 0 | 95.81 | 0.07 |
| LUMO+26 | 0.07 | 0.61 | 0.77 | 0 | 0 | 0 | 98.54 | 0.01 |
| LUMO+28 | 0.5 | 4.24 | 0.61 | 0 | 0 | 0 | 94.59 | 0.01 |
| LUMO+29 | 1.52 | 14.02 | 2.31 | 0 | 0 | 0 | 81.81 | 0.04 |
| LUMO+30 | 0.12 | 0.84 | 0.29 | 0 | 0 | 0 | 98.71 | 0.04 |
| LUMO+31 | 0 | 0.01 | 0.08 | 0 | 0 | 0 | 99.89 | 0.02 |
| LUMO+33 | 1.77 | 14.13 | 1.81 | 0 | 0 | 0 | 81.96 | 0 |
| LUMO+35 | 0.3 | 2.61 | 0.31 | 0 | 0 | 0 | 96.7 | 0.02 |
| LUMO+36 | 0.35 | 3.21 | 0.27 | 0 | 0 | 0 | 96.16 | 0 |
| LUMO+37 | 0.11 | 1.19 | 0.16 | 0 | 0 | 0 | 98.38 | 0.1 |
| LUMO+39 | 0.47 | 4.03 | 0.58 | 0 | 0 | 0 | 94.81 | 0 |

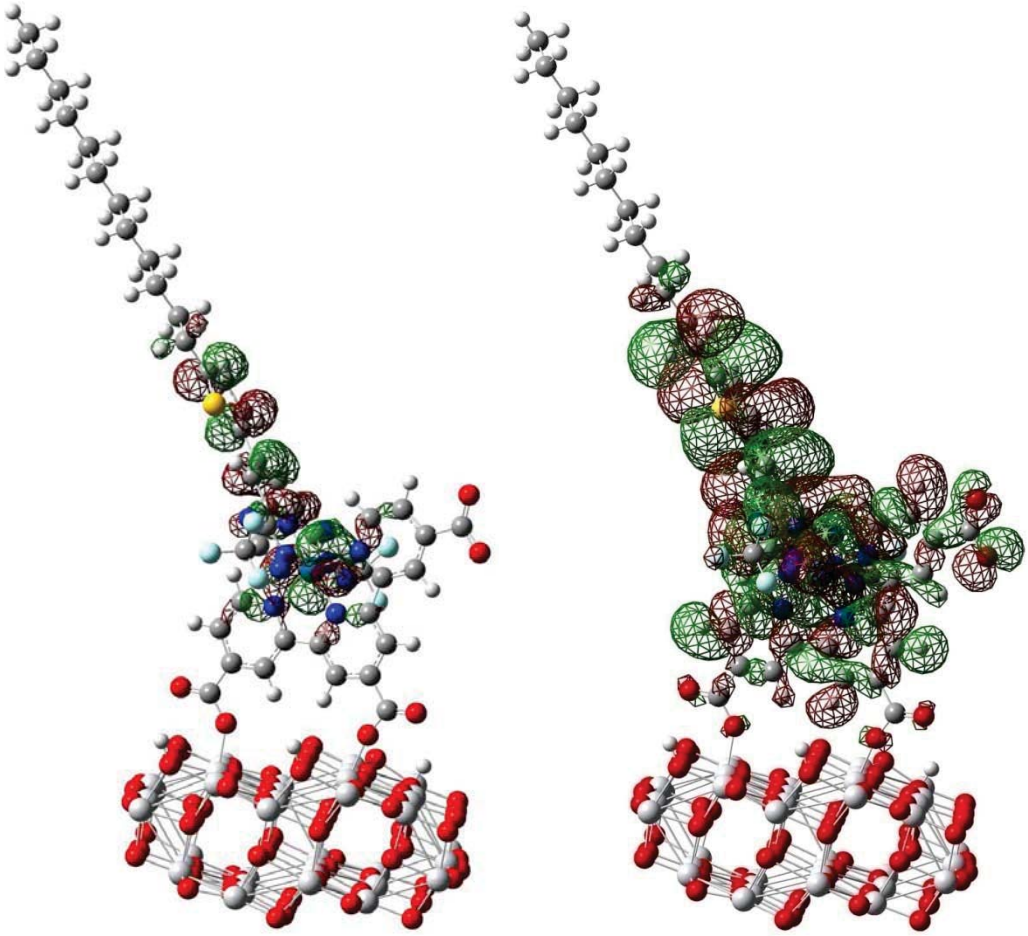

**Figure 2.12** The HOMO-1 of TF-52-Os/$(TiO_2)_{38}$. The isovalue for the contour is 0.02 (left) and 0.002 (right), respectively.

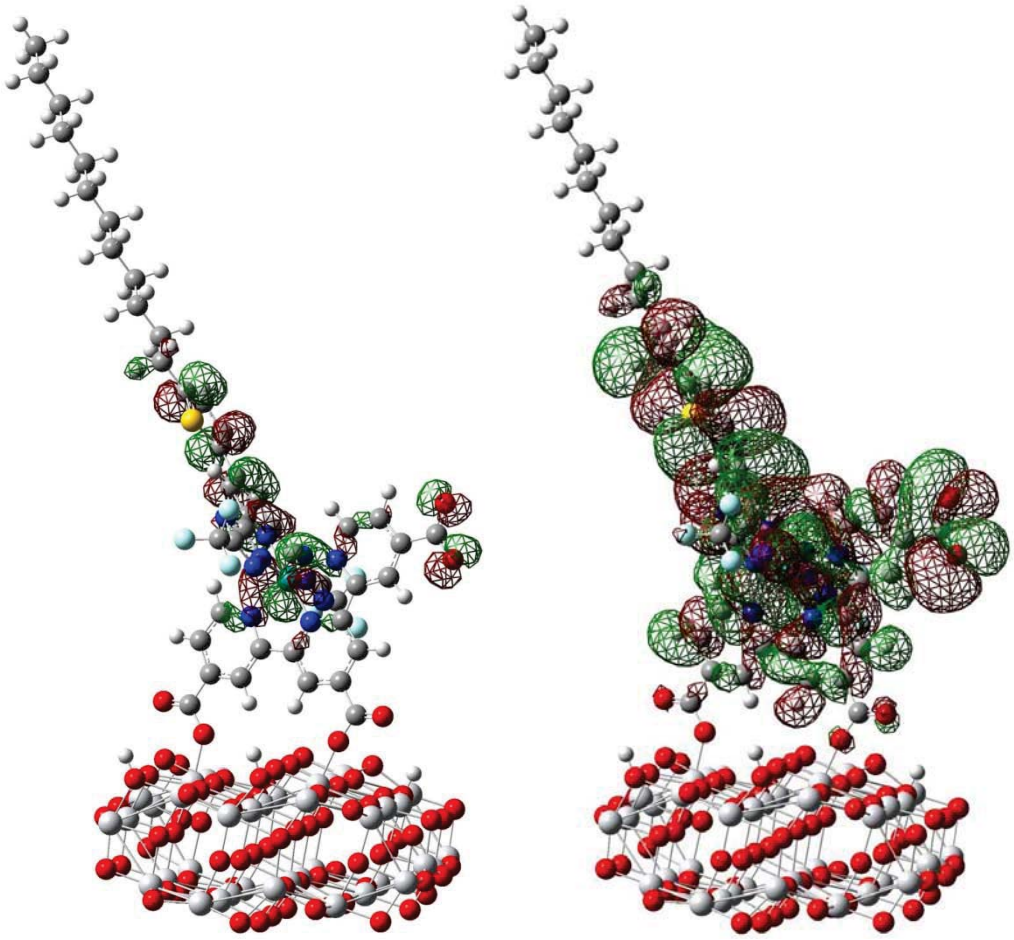

**Figure 2.13** The HOMO-1 of TF-52-Ru/$(TiO_2)_{38}$. The isovalue for the contour is 0.02 (left) and 0.002 (right), respectively.

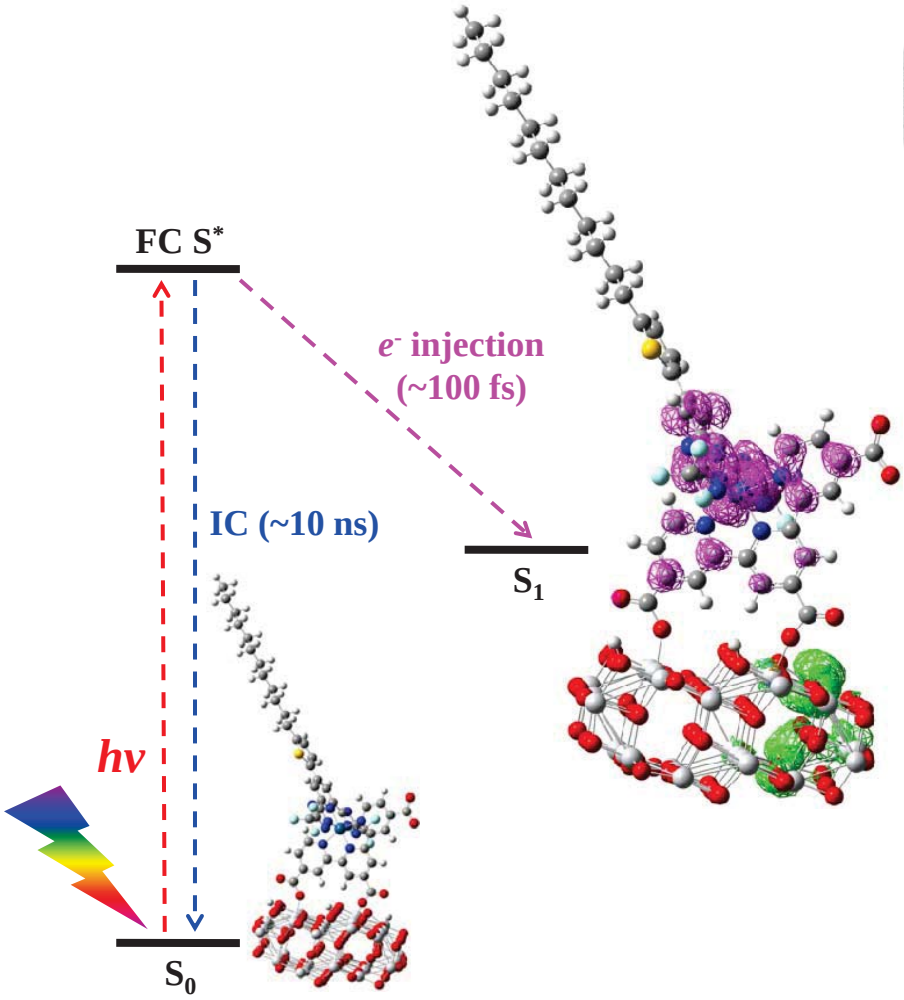


**Figure 2.14** Schematic illustration of the ground state $S_0$, Frank–Condon excited state S*, and the nuclear geometry optimized medium state $S_1$ during the photoexcitation in TF-52-Os/$(TiO_2)_{38}$. Pink mesh indicates the decrease of charge density, while green mesh indicates the increase of charge density unop photoexcitation. The isovalue for the contours is 0.02. FC and IC stands for Frank-Condon and internal conversion, respectively.

**Table 2.10** The electronic coupling ($H_{ab}$) in $cm^{-1}$ of (a) TF-51-Ru/$(TiO_2)_{38}$ and (b) TF-52-Ru/$(TiO_2)_{38}$.

| | $\mu_{ab}$ (Debye) | $m_{ab}$ (Debye) | $\Delta E_{ab}$ (eV) | $H_{ab}$ ($cm^{-1}$) |
|---|---|---|---|---|
| (a) TF-51-Ru/$(TiO_2)_{38}$ | 11.7340 | 0.0428 | 0.497 | 2004.15 |
| (b) TF-52-Ru/$(TiO_2)_{38}$ | 9.1702 | 0.1282 | 0.63 | 2540.48 |

**Table 2.11** The calculated dipole moment in S* and $S_1$ of (a) TF-51-Ru/$(TiO_2)_{38}$ and (b) TF-52-Ru/$(TiO_2)_{38}$.

| (a) TF-51-Ru/$(TiO_2)_{38}$ | $\mu_x$ (Debye) | $\mu_y$ (Debye) | $\mu_z$ (Debye) | $\|\mu\|$ (Debye) |
|---|---|---|---|---|
| S* | -55.5146 | 12.4775 | -13.4902 | 58.4769 |
| $S_1$ | -44.1734 | 9.6946 | -14.6384 | 47.5348 |
| (b) TF-52-Ru/$(TiO_2)_{38}$ | $\mu_x$ (Debye) | $\mu_y$ (Debye) | $\mu_z$ (Debye) | $\|\mu\|$ (Debye) |
| S* | 43.2549 | 26.4012 | -27.3323 | 57.5766 |
| $S_1$ | 36.3687 | 21.5909 | -23.7290 | 48.4965 |

**Table 2.12** The calculated transition dipole moment in S* and $S_1$ of (a) TF-51-Ru/$(TiO_2)_{38}$ and (b) TF-52-Ru/$(TiO_2)_{38}$.

| (a) TF-51-Ru/$(TiO_2)_{38}$ | $m_x$ (Debye) | $m_y$ (Debye) | $m_z$ (Debye) | $\|m\|$ (Debye) |
|---|---|---|---|---|
| S* | 0.0034 | -0.002 | 0.0017 | 0.0043 |
| $S_1$ | -0.0185 | 0.0323 | -0.0115 | 0.039 |
| (b) TF-52-Ru/$(TiO_2)_{38}$ | $m_x$ (Debye) | $m_y$ (Debye) | $m_z$ (Debye) | $\|m\|$ (Debye) |
| S* | -0.0459 | -0.0225 | 0.0417 | 0.0660 |
| $S_1$ | 0.0348 | -0.0262 | -0.0579 | 0.0725 |

## 2.6 References


1. O'Regan, B.; Grätzel, M. *Nature* **1991**, *353*, 737–740.
2. Grätzel, M. *Nature* **2001**, *414*, 338–344.
3. Hagfeldt, A.; Boschloo, G.; Sun, L.; Kloo, L.; Pettersson, H. *Chem. Rev.* **2010**, *110*, 6595–6663.
4. Boschloo, G.; Hagfeldt, A. *Acc. Chem. Res.* 2009, **41**, 1819–1826.
5. Yella, A.; Lee, H. W.; Tsao, H. N.; Yi, C.; Chandiran, A. K.; Nazeeruddin, M. K.; Diau, E. W. G. Yeh, C. Y.; Zakeeruddin, S. M.; Grätzel, M. *Science* **2011**, *334*, 629–634.
6. Fantacci, S.; De Angelis, F. *Coord. Chem. Rev.* **2011**, *255*, 2704–2726.
7. Martsinovich, N.; Troisi, A. *Energy Environ. Sci.* **2011**, *4*, 4473–4495.
8. Labat, F.; Bahers, T. L.; Ciofini, I.; Adamo, C. *Acc. Chem. Res.* **2012**, *45*, 1268–1277.
9. Anselmi, C.; Mosconi, E.; Pastore, M.; Ronca, E.; De Angelis, F. *Phys. Chem. Chem. Phys.* **2012**, *14*, 15963–15974.
10. Pastore, M.; De Angelis, F. *J. Phys. Chem. Lett.* **2013**, *4*, 956–941.
11. Pastore, M.; Mosconi, E.; Fantacci, S.; De Angelis, F. *Curr. Org. Synth.* **2012**, *9*, 215–232.
12. Pastore, M.; Fantacci, S.; De Angelis, F. *J. Phys. Chem. C* **2013**, *117*,

3685–3700.

13. Sousa, C.; Tosoni, S.; Illas, F. *Chem. Rev*. **2013**, *13*, 4456–4495.

14. Persson, P.; Lundqvist, M. J. *J. Phys. Chem. B* **2005**, *109*, 11918–11924.

15. Labat, F.; Ciofini, I.; Hratchian, H. P.; Frisch, M. J.; Raghavachari, K.; Adamo, C. *J. Phys. Chem. C* **2011**, *115*, 4297–4306.

16. Labat, F.; Ciofini, I.; Adamo, C. *J. Mater. Chem.* **2012**, *22*, 12205–12211.

17. Martsinovich, N.; Ambrosio, F.; Troisi, A. *Phys. Chem. Chem. Phys.* **2012**, *14*, 16668–16676.

18. De Angelis, F.; Fantacci, S.; Selloni, A.; Nazeeruddin, M. K.; Grätzel, M. *J. Am. Chem. Soc*. **2007**, *129*, 14156–14157.

19. De Angelis, F.; Fantacci, S.; Selloni, A. *Nanotechnology*, **2008**, *19*, 424002(7pp).

20. De Angelis, F.; Fantacci, S.; Selloni, A.; Nazeeruddin, M. K.; Grätzel, M. *J. Phys. Chem. C* **2010**, *114*, 6054–6061.

21. De Angelis, F.; Fantacci, S.; Mosconi, E.; Nazeeruddin, M. K.; Grätzel, M. *J. Phys. Chem. C* **2011**, *115*, 8825–8831.

22. Mosconi, E.; Yum, J. H.; Kessler, F.; Gómez García, C. J.; Zuccaccia, C.; Cinti, A.; Nazeeruddin, M. K.; Grätzel, M.; De Angelis, F. *J. Am. Chem. Soc*. **2012**, *134*, 19438–19453.

23. Sodeyama, K.; Sumita, M.; O'Rourke, C.; Terranova, U.; Islam, A.; Han, L.; Bowler, D. R.; Tateyama, Y. *J. Phys. Chem. Lett.* **2012**, *3*, 472–477.

24. Chen, J.; Bai, F. Q.; Wang, J.; Hao, L.; Xie, Z. F.; Pan, Q. J.; Zhang, H. X. *Dyes Pigm.* **2012**, *94*, 459–468.

25. Liu, S. H.; Fu, H.; Cheng, Y. M.; Wu, K. L.; Ho, S. T.; Chi, Y.; Chou, P. T. *J. Phys. Chem. C* **2012**, *116*, 16338–16345.

26. Fantacci, S.; Lobello, M. G.; De Angelis, F. *Chimia*, **2013**, *67*, 121–128.

27. Kandada, A. R. S.; Fantacci, S.; Guarnera, S.; Polli, D.; Lanzani, G.; De Angelis, F.; Petrozza, A. *ACS Appl. Mater. Interfaces* **2013**, *5*, 4334–4339.

28. Lundqvist, M. J.; Nilsing, M.; Lunell, S.; Åkermark, B.; Persson, P. *J. Phys. Chem. B* **2006**, *110*, 20513–20525.

29. Abbotto, A.; Sauvage, S.; Barolo, C.; De Angelis, F.; Fantacci, S.; Grätzel, M.; Manfredi, N.; Marinzi, C.; Nazeeruddin, M. K. *Dalton Trans.* **2011**, *40*, 234–242.

30. De Angelis, F.; Vitillaro, G.; Kavan, L.; Nazeeruddin, M. K.; Grätzel, M. *J. Phys. Chem. C* **2012**, *116*, 18124–18131.

31. Pastore, M.; De Angelis, F. *J. Phys. Chem. Lett.* **2012**, *3*, 2146–2153.

32. Sauvé, G.; Cass, M. E.; Coia, G.; Doig, S. J.; Lauermann, I.; Pomykal, K. E.; Lewis, N. S. *J. Phys. Chem. B* **2000**, *104*, 6821–6836.

33. Altobello, S.; Argazzi, R.; Caramori, S.; Contado, C.; Da Fré, S.; Rubino, P.; C.

Choné, Larramona, G.; Bignozzi, C. A. *J. Am. Chem. Soc.* **2005**, *127*, 15342–15343.

34. Onicha, A. C.; Castellano, F. N. *J. Phys. Chem. C* **2010**, *114*, 6831–6840.

35. Yamaguchi, T.; Miyabe, T.; Ono, T.; Arakawa, H. *Chem. Commun.* **2010**, *46*, 5802–5804.

36. Wu, K. L.; Ho, S. T.; Chou, C. C.; Chang, Y. C.; Pan, H. A.; Chi, Y.; Chou, P. T.; *Angew. Chem. Int. Ed.* **2012**, *51*, 5642–5646.

37. Kinoshita, T.; Fujisawa, J. i.; Nakazaki, J.; Uchida, S.; Kubo, T.; Segawa, H. *J. Phys. Chem. Lett.* **2012**, *3*, 394–398.

38. Verma, S.; Kar, P.; Banerjee, T.; Das, A.; Ghosh, H. N. *J. Phys. Chem. Lett.* **2012**, *3*, 1543–1548.

39. Banerjee, T.; Kaniyankandy, S.; Das, A.; Ghosh, H. N. *Inorg. Chem.* **2013**, *52*, 5366–5377.

40. Chou, P. T.; Chi, Y. *Chem. Eur. J.* **2007**, *13*, 380–395.

41. Chi, Y.; Chou, P. T. *Chem. Soc. Rev.* **2007**, *36*, 1421–1431.

42. Chi, Y.; Chou, P. T. *Chem. Soc. Rev.*, **2010**, *39*, 638–655.

43. Chou, P. T.; Chi, Y.; Chung, M. W.; Lin, C. C. *Coord. Chem. Rev.* **2011**, *255*, 2653–2665.

44. Zubavichus, Y. V.; Slovokhotov, Y. L.; Nazeeruddin, M. K.; Zakeeruddin, S. M.; Grätzel, M.; Shklover, V. *Chem. Mater.* **2002**, *14*, 3556–3563.

45. Bauer, C.; Boschloo, B.; Mukhtar, E.; Hagfeldt, A. *J. Phys. Chem. B* **2002**, *106*, 12693–12704.

46. Persson, P.; Gebhardt, J. C. M.; Lunell, S. *J. Phys. Chem. B* **2003**, *107*, 3336–3339.

47. Lundqvist, M. J.; Nilsing, M.; Persson, P.; Lunell, S. *Int. J. Quantum Chem.*, **2006**, *106*, 3214–3234.

48. Cave, R. J.; Newton, M. D. *Chem. Phys. Lett.* **1996**, *249*, 15–19.

49. Newton, M. D. *Coord. Chem. Rev.* **2003**, *238*, 167–185.

50. Subotnik, J. E.; Yeganeh, S.; Cave, R. J.; Ratner, M. A. *J. Chem. Phys.* **2008**, *129*, 244101(10pp).

51. Nitzan, A. *Chemical Dynamics in Condensed Phases Relaxation, Transfers, and Reactions in Condensed Molecular Systems*, (Oxford University Press, New York, **2006**), p. 588.

52. Hsu, C. P. *Acc. Chem. Res.* **2009**, *42*, 509–518.

53. Chen, H. C.; Hsu, C. P. *J. Phys. Chem. A* **2005**, *109*, 11989–11995.

54. Frisch, M. J.; Trucks, G. W.; Schlegel, H. B.; Scuseria, G. E.; Robb, M. A.; Cheeseman, J. R.; Scalmani, G.; Barone, V.; Mennucci, B.; Petersson, G. A.; et al. Gaussian *09*, revision A.02; Gaussian, Inc.: Wallingford, CT, 2009.

55. Dirac, P. A. M. *Proc. R. Soc. Lond. A* **1927**, *114*, 243–265.

56. Marcus, R. A. *J. Chem. Phys.* 1956, **24**, 966–978.

57. Dong, C. Li, X.; Zhao, W.; Jin, P.; Qi, J. *J. Phys. Chem. C* **2013**, *117*, 9092–9103.

58. Mead, C. A.; Truhlar, D. G. *J. Chem. Phys.* **1982**, *77*, 6090–6098.